HIGH TENOR NI-PGE SULFIDE MINERALIZATION OF THE SOUTH MANASAN ULTRAMAFIC INTRUSION, THOMPSON NICKEL BELT, MANITOBA

by
ANATOLIY FRANCHUK

A thesis submitted in partial fulfillment
of the requirement for the degree of
Master of Science (M.Sc.) in Geology

The School of Graduate Studies
Laurentian University
Sudbury, Ontario, Canada

THESIS DEFENCE COMMITTE/COMITÉ DE SOUTENANCE DE THÈSE

Laurentian Université/Université Laurentienne
School of Graduate Studies/École des études supérieures

Title of Thesis Titre de la thèse	HIGH TENOR NI-PGE SULFIDE MINERALIZATION OF THE SOUTH MANASAN ULTRAMAFIC INTRUSION, THOMPSON NICKEL BELT, MANITOBA
Name of Candidate Nom du candidat	Franchuk, Anatoliy
Degree Diplôme	Master of Science
Department/Program Département/Programme	Geology
Date of Defence Date de la soutenance	April 22, 2014

APPROVED/APPROUVÉ

Thesis Examiners/Examinateurs de thèse:

Dr. Peter C. Lightfoot
(Co-supervisor/Co-directeur de thèse)

Dr. Daniel Kontak
(Co-supervisor/Co-directeur de thèse)

Dr. C. Michael Lesher
(Committee member/Membre du comité)

Dr. David C. Peck
(External Examiner/Examinateur externe)

Approved for the School of Graduate Studies
Approuvé pour l'École des études supérieures
Dr. David Lesbarrères
M. David Lesbarrères
Director, School of Graduate Studies
Directeur, École des études supérieures

ACCESSIBILITY CLAUSE AND PERMISSION TO USE

Thesis abstract

The South Manasan ultramafic intrusion (ca. 1880 Ma) located in the Early Proterozoic Thompson Nickel Belt (TNB) contains Ni and platinum group element (PGE) mineralization hosted by disseminated sulfide. Whole-rock Ni values range from 0.3 to 1.7 wt. % and total precious metals (TPMs) range from 0 to 1.3 ppm Pt + Pd + Au and equate to tenor values (i.e., metal in 100% sulfide) of 11-39 wt. % Ni and 8-27 ppm TPMs. The South Manasan intrusion is a steeply dipping sill-like body with a boudinaged outline having a strike length of approximately 1200 m, average width of 125 m and a minimum depth extent of 1000 m. The intrusion is composed of approximately 25% fresh dunite, 50% serpentine altered dunite and 25% tectonized and carbonate altered dunite. The most intense alteration is found near the intrusion's margin where it is in contact with metasedimentary rocks of the Pipe Formation, part of the surrounding Ospwagan Group. In fresh dunite the sulfide assemblage characterized by an intercumulate texture is dominated by pentlandite with accessory pyrite; the latter having a symplectic-like texture. The pentlandite-pyrite assemblage in the serpentinized dunite, although still characterized overall by an intercumlate-texture, has well developed platy intergrowths with chlorite and serpentine. In the most intensely modified unit (the carbonate altered dunite) the sulfide assemblage consists primarily of pyrrhotite and pentlandite.

Whole-rock geochemical data (n=360), modal mineralogy and mineral chemistry obtained on representative drill core throughout the South Manasan intrusion have been used to establish a type section in order to evaluate the relative roles of primary magmatic versus secondary (i.e., serpentinization, carbonate alteration and deformation) processes. These data indicate that the primary silicate-sulfide assemblage was systematically modified during

serpentinization, carbonate alteration and deformation of the South Manasan intrusion such that a sequence of primary versus secondary events can be established. Intrusion of the original komatiitic magma and formation of the South Manasan intrusion took place at a shallow level into consolidated Ospwagan Group sediments with subsequent contamination of this melt with crustal S. This triggered sulfide saturation and generation of an immiscible sulfide melt. Calculated Ni and TPM tenor values constrain the R factor to between 500 and 2500. The early crystallization of olivine inhibited the sulfide melt from settling to the bottom of the magma column and as a consequence, the sulfides now have a primary interstitial magmatic texture. The current sulfide association dominated by pentlandite>>pyrite>chalcopyrite has a mineral paragenesis that is consistent with subsolidus re-equilibration of a primary pentlandite-pyrrhotite-chalcopyrite assemblage. The subsequent processes of serpentinization, deformation and carbonate alteration resulted in modifying the primary sulfide assemblages and their textures (i.e., to platy habits), but did not greatly alter the bulk composition, in particular metal contents, except for addition of volatiles (H_2O, CO_2).

It is concluded therefore that the enrichment of the sulfide assemblage at South Manasan in Ni and PGEs is a consequence of a primary magmatic process involving high R factor and that the effects of later overprinting processes (alteration, deformation) are not responsible for the presently observed high-tenor sulfide association.

Keywords: nickel, magmatic ore deposit, Thompson Nickel Belt, ultramafic rocks, disseminated sulfide, komatiite.

Statement of responsibilities

The candidate was supervised by Dr. Peter C. Lightfoot and Dr. Daniel Kontak. The thesis manuscript consists of three chapters with chapter 2 being presented as a journal paper with the candidate and thesis supervisors as co-authors. The candidate logged project diamond drill cores, prepared samples for whole-rock geochemical analysis and selected core chips for polished thin sections. Thin sections selected by the candidate were prepared at the Vancouver Petrographics Ltd. laboratory. The aspirant performed all of the microscope work and collected and processed all of the SEM-EDS analysis used in the study. In addition, mineral chemistry of the selected thin sections was acquired using the wavelength dispersive electron microprobe. The analysis was done by Dr. Chusi Li at the Indiana University. Several drafts were produced by the candidate and edited by thesis supervisors.

Acknowledgments

I would like to thank Dr. Peter Lightfoot for shaping the project, for his advice and patience through the research process; acknowledgments are extended to Dr. Daniel Kontak for guidance on the SEM-EDS and the ore microscope and for his enthusiasm for the project; both are thanked for putting that extra effort to overcome the bureaucratic obstacles in the way. Dr. Josef Macek is thanked for sharing his great knowledge of the Thompson Nickel Belt geology in the core shack and in the field. Rob Stewart, Manager Nickel Exploration (Thompson) is thanked for suggesting the South Manasan ultramafic body exploration target in 2008 and for accommodating the time and cash required to complete this study. This study would not be possible without the financial support and access to the data provided by Vale Base Metals and Scott Mooney, Manager of Brownfield Exploration (Canada). Acknowledgements go to my colleagues at the Vale Exploration office in Thompson, MB. A special thank you to my wife Lucine Franchuk for the great support and patience; many perfect fishing weekends and movie nights were sacrificed for this.

Table of Contents

List of Tables

List of Figures

List of Appendices

List of Data repositories

Data repository 1: Table of precision and analytical ranges for the lithogeochemical methods used to obtain data from the whole-rock samples of the South Manasan intrusion. Digital file in Excel 2010 format.

Data repository 2: Table of lithogeochemical results from the whole-rock analysis of the South Manasan intrusion. Digital file in Excel 2010 format.

Data repository 3: Table of mineral chemistry results from the SEM-EDS analysis of mineral grains in carbon-coated polished thin sections from the South Manasan intrusion. Digital file in Excel 2010 format.

Data repository 4: Table of mineral chemistry results from the Microprobe analysis of mineral grains in carbon-coated polished thin sections from the South Manasan intrusion. Digital file in Excel 2010 format.

CHAPTER 1: Introduction to Thesis

Introduction

The Thompson Nickel Belt (TNB) is a NNE-trending thrust and fold belt situated on the north-western margin of the Archaean Superior Province in northern Manitoba, Canada (Fig 1A). The TNB comprises reworked Ospwagan Group metasedimentary rocks, basement gneisses, mafic-ultramafic intrusive and volcanic rocks. The terrane is 400 km long and contains a number of Ni-Cu-PGE sulfide deposits (McRitchie, 1995; Lightfoot et al., 2012; Lightfoot et al., in prep) and is considered one of four principal Ni camps in Canada, the others being Sudbury, Ontario, Ragland, Quebec, and Voisey's Bay, Labrador. The part of the TNB that is not under Phanerozoic cover is between Moak and Manibridge (Fig. 1A); this section of the TNB is about 180 km long and 30 km wide and has been subjected to intensive exploration that led to the discovery of numerous Ni sulfide deposits, two of which are currently being mined, the Thompson and Birchtree deposits.

Exploration of the TNB using geophysical methods and diamond drilling began in 1946 (Zurbrigg, 1962). The result of these efforts was the discovery of the South Mystery (1949), Moak (1952), Soab (1953), North Mystery (1954), Thompson (1956) and Pipe (1957) deposits. The discovery of the large, massive Ni sulfide Thompson orebody in 1956 marked a turning point in the exploration history. The orebody was named after the head of Inco Exploration, Dr. John F. Thompson. Commercial production from the orebody started in 1961 with a newly constructed integrated mining, milling, smelting and refining complex.

Further exploration work in the belt produced the discovery of Birchtree (1962), South Manasan (1966), Ospwagan (1975), as well as a large number of significant Ni sulfide

occurrences. From the 1980's onwards the exploration activity has concentrated near the Birchtree and Thompson orebodies, which allowed for significant expansion of the deposits. Past production from Thompson Mine is 2500 kt Ni, which is double the historic resources from Kambalda (1200kt Ni; Hoatson et al., 2006; Mudd, 2010). Current National Instruments 43-101 compliant reserves for Thompson Mine are 27.54 Mt @ 1.75% Ni; there are also unreported resources and ongoing exploration successes by Vale (Lightfoot et al., 2012). Unmined resources and reserves and in 2012 are greater than those identified at the time of initial mine construction in 1959.

The magmatic Ni sulfide mineralization is believed to have formed as a result of sulfur saturation and precipitation of immiscible sulfide liquid from komatiitic magma (Lesher et al., 2001)). The timing of the sulfide mineralization is constrained to 1885 ± 49 Ma based on Re-Os determination from sulfide ore samples at Thompson Mine (Hulbert et al., 2005). The sulfide mineralization and host rocks have been subsequently heavily deformed and metamorphosed to upper amphibolite facies during the Trans-Hudson orogeny at 1.7 Ga. Thus, the primary linkage between ultramafic magmatism and the formation of magmatic sulfide ores is obscured by deformation and metasomatic alteration. As a result, TNB deposits range in mineralization style from relatively fresh interstitial sulfides through deformed ultramafic-associated mineralization to metasediment-hosted mineralization remobilized from the parent ultramafic rocks. The distribution of massive and semi-massive Ni-sulfide mineralization is heavily controlled by structural fabric. In the cases of the Thompson and Pipe deposits important ore bodies develop in dilation zones parallel to the fold axis (Gribbin et al., 2011).

Geology of the Thompson Nickel Belt

Stratigraphic Framework

The ultramafic rocks of the TNB and the associated Ni sulfide mineralization are hosted exclusively in the Ospwagan Group metasedimentary rocks. The current understanding of the Ospwagan Group stratigraphy came from many decades of careful work by exploration geologists and researchers who have broken out the stratigraphy of the Ospwagan Group host rocks (Bleeker, 1990), recognized the stratigraphic position of the economically mineralized ultramafic intrusive bodies (Bleeker, 1990; Layton-Matthews et al., 2010; Peredery et al., 1982; Zurbrigg, 1963), and begun to unpick the complex deformation and metamorphic history as they relate the geometry of the ore bodies (Bleeker, 1990; Layton-Matthews et al., 2011), and the significance to exploration (Lightfoot et al., 2012). These studies, in the context of belt-scale magnetic, electromagnetic, and audio-magnetotelluric surveys together with drilling have now established the deeper structure of the belt and provided the basis to extend stratigraphy to depth (Gribbin, 2011; McDowell et al., 2007).

The Ospwagan Group shows considerable lithological diversity from its stratigraphic base to the top, as illustrated in Figure 1B. Variation in the metamorphic grade from middle amphibolite grade to upper amphibolite provide for further diversity in appearance. For a complete description of the Ospwagan Group stratigraphy the reader is referred to (Bleeker, 1990; Macek et al., 2004, 2005; McGregor and Macek, 2003; Zwanzig et al., 2007). Below is a brief summary.

The Manasan Formation (M) unconformably overlies the Achaean basement gneiss and forms the lowermost unit of the Ospwagan Group. The Manasan Formation likely formed during

initial siliclastic sedimentation of the rift margin. It consists of two members: the lower M1 and upper M2. The M1 member is typically a light grey meta-sandstone with a high proportion of quartz. The M2 member occurs as muscovite-biotite-quartz-feldspar schist at middle-amphibolite grade and as sillimanite-biotite-quartz-feldspar gneiss at upper-amphibolite grade. A characteristic feature of the M2 member is the presence of quartzofeldspathic or pegmatitic segregations and veinlets (Bleeker, 1990; Couëslan et al., 2011; Zwanzig et al., 2007).

The Thompson Formation (T) is stratigraphically above the M2 and is likely a result of simultaneous siliclastic sedimentation and chemical precipitation of calcareous muds; three members are recognized. The lowermost T1 member is a medium to coarse grained, thinly layered schist of diverse composition and texture. Quartz, microcline, plagioclase and biotite are the principal minerals and are complemented by phlogopite, chlorite, calcite, dolomite, diopside, amphibole, epidote, hematite and sphene in various proportions. It is interpreted that the mineralogical and textural diversity is a result of metamorphic recrystallization of hybrid (siliciclastic and calcareous) mud into medium to coarse grained schist. The middle T2 member is a biotite-diopside-quartz-feldspar gneiss layer; it occurs only in the Thompson Mine and possibly represents local episodic influx of siliclastic material into the Thompson sequence. The upper T3 member is a dolomite marble with partly serpentinized olivine, phlogopite and coarse-grained diopside. The characteristic composition and texture make the Thompson Formation an excellent lithostratigraphic marker.

The Pipe Formation (P) overlies the T3 and is the stratigraphic host to most of the magmatic Ni-Cu sulfide deposits and the majority of ultramafic intrusive rocks. It comprises three members. The lowermost P1 member is composed of a thin band of sulfide facies and silicate facies iron formation. The sulfide facies iron formation comprises graphite- and

pyrrhotite-rich metapelitic schist and the silicate facies iron formation comprises grunerite, Ca-amphibole, magnetite, quartz, garnet, biotite, chlorite, pyrrhotite, and graphite in different proportions (Coueslan, et al., 2006).

The P2 occurs in two metamorphic varieties. The middle amphibolite grade variety is biotite-muscovite-quartz-feldspar schist with 1-5 cm thick segmented quartz-rich intercalations and rare 10-50 cm thick calc-silicate layers. The very top of the P2 schist hosts the upper sulfide facies iron formation several tens of centimeters thick, rich in graphite and pyrrhotite. This sulfide facies iron formation represents the lithostratigraphic level at which the ore of the Thompson mine is located (Fig. 1B). The upper amphibolite grade variety of the P2 is grey-brown, coarse grained, sillimanite-garnet-biotite-quartz-feldspar gneiss. Intercalations of thin quartz-rich layers and lenses are likely derived from episodic precipitation of chert.

The P3 member is lithologically very diverse. It is a varied succession of pyrrhotite-bearing, biotite-rich quartzofeldpatic metasedimentary rocks; silicate facies iron formations, ironstones, cherts, dolomite marble and calc-silicates. The silicate iron formation layers are composed of grunerite, hornblende, diopside, quartz, feldspars, magnetite, garnet, biotite, pyrrhotite, and carbonate in different combinations and proportions. Ironstone layers are rich in garnet, biotite, grunerite, and quartz. Beige subtly layered dolomite marble, as well as several layers of calc-silicate, are hosted by iron formations and serve as lithostratigraphic markers. Its precursor could be either siliciclastic sediment intermittently contaminated by calcareous precipitate, or alternatively, hybrid sediment generated by silica precipitation with simultaneous sedimentation of clastic pelite and complemented by an episodic deposition of calcareous precipitate.

The overlying Setting Formation (S) comprises a collection of various clastic metasedimentary rocks that occur stratigraphically above the last P3 iron formation, but below volcanogenic succession of the Bah Lake assemblage (B). It is subdivided into two members: the S1 comprising finer grain rocks and the S2 composed of more diverse, coarser rocks. The S1 is constituted of feldspathic metaquartzite rhythmically interlayered with sillimanite-biotite metapelite schist. This turbiditic sequence contains unique pinkish-brown concretions (3-15 cm thick, up to 3 m long layer segments) enriched in poikiloblastic garnet and carbonate. The S2 is exposed only in disconnected lithostratigraphic fragments, such as metagraywacke, quartz-rich feldspathic wacke grading into metapelite or oligomictic conglomerate. The lithostratigraphic relation between the S1 and S2 members is also uncertain due to the lack of exposure continuity and also because the S1-S2 and S2-B contacts are not exposed.

The Bah Lake assemblage forms the top of the Ospwagan Group. It comprises metamorphic equivalents of various mafic and ultramafic volcanogenic rocks. Pillowed and massive metabasalt flows dominate over intercalated tabular bodies of metapicrite (these are possibly flows or sills). The metabasalts have been transformed into plagioclase amphibolites, whereas metapicrite occurs as fine grained, tremolite-actinolite-chlorite-carbonate schist rich in dusty magnetite. Some metapicrite bodies contain forsterite porphyroblasts up to 20 mm in size. The contact between the Bah Lake assemblage and Setting Formation (S1 member) is exposed at only one locality and appears to be autochthonous. It is accompanied by rusty-weathering gossan.

The lithostratigraphic framework of the Ospwagan Group is critical to the understanding of the mineral potential of the contained ultramafic bodies. Although ultramafic bodies can be found at any stratigraphic level (Fig. 1B), the ultramafic bodies associated with Ni sulfide

mineralization are located in or near the Pipe Formation which is currently the most important for mineral exploration. To identify this horizon among many lithological units in the drill core is a crucial task in exploration that requires a detailed knowledge of each of the units of the Ospwagan Group. These units can vary in their appearance according to the metamorphic grade and they can also be modified in appearance by differing intensities of shearing and alteration. The detailed features are also important because they can aid in the recognition of the Burntwood River and Grass River groups that are economically unimportant, but are also encountered in drill core. A detailed knowledge of the Ospwagan Group lithology is an essential tool in areas covered by glacial overburden where geophysical anomalies followed by drilling constitute the primary method of exploration.

Structural history

The Hudsonian Orogeny (ca. 1.9 – 1.7 Ga) resulted from the collision of the Churchill and Superior provinces and subjected the Ospwagan Group together with the Archaean basement to polyphase deformation and amphibolite facies metamorphism (Bleeker, 1990). The ultramafic sills were deformed into boudins or cigar-shaped bodies, and the original contact relationships were destroyed. Maximum P-T conditions have been established as 5.5 kbar and 710 °C (Couëslan et al., 2011) and the age of re-crystallization constrained to 1780 Ma (Bleeker, 1990; Hamilton and Bleeker, 2002).

In this study Bleeker's (1990) interpretation of structural evolution is adopted where four main deformation events are recognized. D1 is interpreted to be a recumbent isoclinal folding event which produced nappe structures. During the post-D1 and pre-D2 interlude the 1883 ± 2 Ma Molson dyke swarm intruded the sedimentary sequence (Heaman et al., 1986). Molson dykes

are observed to cut ultramafic rocks at Pipe and South Manasan that appear to be folded by the D1 event at Pipe. The D2 event was responsible for F2 folding of F1 structures and development of a fabric under peak metamorphic conditions. D3 is interpreted to be a sinistral transpression event responsible for producing F3 folding resulting in dome and basin interference patterns; the type example is the Thompson Dome. The D3 deformational phase continued with formation of minor, open, subhorizontal F4 folds that developed on some steep F3 limbs. This may possibly reflect gravitational collapse of the high amplitude F3 folds (Bleeker, 1990c). Subvertical F5 folds were developed only locally and do not affect the regional F1-F2-F3 pattern. The D4 dextral transpression produced a terminal minor adjustment to the TNB F1-F2-F3 geological configuration as evidenced by kink folds along with dextral pseudotachylite generating brittle faults, conjugate brittle faults and joints.

Focus of the study

The global reserves and resources of high-grade Ni sulfide mineralization with >2 wt. % Ni has been growing at a rate significantly less than the rate of mining of high-grade deposits. In response to this exploration companies have undertaken a variety of strategies to offset the loss of ore. Some of these strategies include the development of Ni-Co laterite deposits with open cast mining methods and production from conventional furnace operations and innovation of new hydrometallurgical methods. Another group of companies have shifted the focus to the assessment of historic discoveries of low grade Ni sulfide mineralization (Mudd, 2010). The TNB contains a number of low grade Ni-Co deposits which have potential to become important new producers under the right economic circumstances.

Over 400 ultramafic rock bodies occur within the TNB (Macek et al., 2006) which range in size from a few meters to a kilometer in thickness and up to a few cubic kilometers in volume; they typically have a boudinaged outline. The ultramafic bodies are believed to be deformed fragments of sills or chonoliths, although the pre-deformation geometry cannot be reliably established. There is no clear relationship between the size of ultramafic body and sulfide mineralization. However, almost all of the ultramafic bodies of the TNB host some amount of disseminated Ni-sulfide mineralization. Some of these bodies are spatially associated with massive sulfide deposits, including past and current Ni-Co producers (e.g., Thompson, Birchtree, Pipe, Soab), but most are not. Some of the ultramafic bodies hosting disseminated sulfide mineralization are large enough to be of interest as a potential bulk-mining open-pit resource. Barnes and Lightfoot (2005) provide historic estimates of quantity of low grade Ni sulfide in the TNB.

The minimum total volume of the ultramafic rock bodies of the TNB can be estimated based on the surface expression and depth extent identified by diamond drilling. In the exposed portion of the TNB (approximately 120 km long) the 42 largest ultramafic bodies have a combined surface footprint of 20.5 km^2. Assuming an average depth extent of 1 km the total volume is approximately 20.5 km^3. In terms of volume and potential economic significance the ultramafic bodies of TNB can be compared to the komatiitic rock in the Yilgarn Craton, Australia. However, unlike the relatively well-understood Western Australian counterparts (Barnes, 2004; Barnes et al., 2011a), there are relatively few publications on the nature or composition of the ultramafic rock bodies of the TNB (Layton-Matthews, 2001; Paktung, 1984; Peredery, 1979) and none on the nature of the disseminated Ni sulfide mineralization hosted by them.

This work contributes to furthering our understanding of the nature of disseminated Ni sulfide mineralization in the TNB by documenting the South Manasan intrusion. The importance and uniqueness of this ultramafic rock body and the associated disseminated sulfide mineralization rests in both the extent of preservation of primary magmatic textures and in the unusual pentlandite- and PGE-rich nature of the sulfides. The detailed logging of new drilling of the South Manasan intrusion completed by Vale in 2009-2010 was followed by careful documentation of the mineralogical and chemical zonation of the intrusion along with examination and interpretation of the preserved textures. The extensive overprinting by amphibolite facies metamorphism, serpentinization and carbonate alteration added to the complexity of the study, which necessitated extensive integration of image analysis obtained through scanning electron microscopy with energy dispersive spectrometry (SEM-EDS) and transmitted reflected light petrography. The results of this study provide new information that supports an assessment of the relative roles of primary magmatic and secondary alteration processes to the current composition of sulfide mineralization.

Structure of Thesis

This thesis is presented in the form of a manuscript to be submitted for publication in a peer-reviewed, internationally circulated geoscience journal. Chapter 1 provides a brief introduction, an explanation of the structure of the thesis, a statement of responsibilities, and personal acknowledgements. Chapter 2 is the final draft of a manuscript formatted for submission to Economic Geology. Chapter 3 provides additional discussion that falls outside of the scope of the journal paper and includes suggestions for future research. Appendix A summarizes the quality control measures employed and provides an assessment of the reliability

of results. Digital data repositories contain method precision and ranges, complete set of whole-rock lithogeochemical results and mineral chemistry results by SEM-EDS and Microprobe.

CHAPTER 2: Journal Paper

High tenor Ni-PGE sulfide mineralization of the South Manasan ultramafic intrusion, Thompson Nickel Belt, Manitoba.

Anatoliy Franchuk[1], Peter C. Lightfoot[2] and Daniel. J. Kontak[3]

1. Vale Technology Development (Canada) Limited, Brownfield Exploration, Thompson, Manitoba, Canada, R8N 1S4;

2. Peter C. Lightfoot, Vale Technology Development (Canada) Limited, Brownfield Exploration, Copper Cliff, Ontario, Canada, P0M 1N0;

3. Daniel. J. Kontak, Department of Earth Sciences, Laurentian University, Sudbury, Ontario, P3E 2C6.

Abstract

The South Manasan ultramafic intrusion (ca. 1880 Ma) located in the Early Proterozoic Thompson Nickel Belt (TNB) contains Ni and platinum group element (PGE) mineralization hosted by disseminated sulfide. Whole-rock Ni values range from 0.3 to 1.7 wt. % and total precious metals (TPMs) range from 0 to 1.3 ppm Pt + Pd + Au and equate to tenor values (i.e., metal in 100% sulfide) of 11-39 wt. % Ni and 8-27 ppm TPMs. The South Manasan intrusion is a steeply dipping sill-like body with a boudinaged outline having a strike length of approximately 1200 m, average width of 125 m and a minimum depth extent of 1000 m. The intrusion is composed of approximately 25% fresh dunite, 50% serpentine altered dunite and 25% tectonized and carbonate altered dunite. The most intense alteration is found near the intrusion's margin where it is in contact with metasedimentary rocks of the Pipe Formation, part of the surrounding Ospwagan Group. In fresh dunite the sulfide assemblage characterized by an intercumulate texture is dominated by pentlandite with accessory pyrite; the latter having a symplectic-like texture. The pentlandite-pyrite assemblage in the serpentinized dunite, although still characterized overall by an intercumlate-texture, has well developed platy intergrowths with chlorite and serpentine. In the most intensely modified unit (the carbonate altered dunite) the sulfide assemblage is pyrrhotite and pentlandite dominant.

Whole-rock geochemical data (n=360), modal mineralogy and mineral chemistry obtained on representative drill core throughout the South Manasan intrusion have been used to establish a type section in order to evaluate the relative roles of primary magmatic versus secondary (i.e., serpentinization, carbonate alteration and deformation) processes. These data indicate that the primary silicate-sulfide assemblage was systematically modified during

serpentinization, carbonate alteration and deformation of the South Manasan intrusion such that a sequence of primary versus secondary events can be established. Intrusion of the original komatiitic magma and formation of the South Manasan intrusion took place at a shallow level into consolidated Ospwagan Group sediments with subsequent contamination of this melt with crustal S. This triggered sulfide saturation and generation of an immiscible sulfide melt. Calculated Ni and TPM tenor values constrain the R factor to between 500 and 2500. The early crystallization of olivine inhibited the sulfide melt from settling to the bottom of the magma column and as a consequence the sulfides now have a primary interstitial magmatic texture. The current sulfide association dominated by pentlandite>>pyrite>chalcopyrite has a mineral paragenesis that is consistent with subsolidus re-equilibration of a primary pentlandite-pyrrhotite-chalcopyrite assemblage. The subsequent processes of serpentinization, deformation and carbonatization resulted in modifying the primary sulfide assemblages and their textures (i.e., to platy habits), but did not greatly alter the bulk composition, in particular metal contents, except for addition of volatiles (H_2O, CO_2).

It is concluded therefore that the enrichment of the sulfide assemblage at South Manasan in Ni and PGEs is a consequence of a primary magmatic process involving high R factor and that the effects of later overprinting processes (alteration, deformation) are not responsible for the presently observed high-tenor sulfide association.

Introduction

The Thompson Nickel Belt (TNB), northern Manitoba, Canada is a world-class Ni-Cu-(PGE) sulfide camp. Thompson Ni-Cu-(PGE) orebody was discovered in 1956 by electro-magnetic geophysical methods and diamond drilling. Many other discoveries, including Birchtree and Pipe followed. The Ni-rich massive sulfide ores are principally associated with both ultramafic rock bodies, such as at the Moak, Soab and Pipe deposits, and sulfidic metasedimentary rocks at the currently producing Thompson and Birchtree mines. These ores are heavily influenced by post-magmatic processes (i.e., metamorphism, deformation) which make primary linkages between ultramafic magmatism and the formation of magmatic sulfide ores often difficult to unravel (Bleeker, 1990; Layton-Matthews et al., 2007; Peredery et al., 1982).

Within the TNB over 400 low-grade disseminated Ni-sulfide occurrences are known in ultramafic rock bodies (Macek et al., 2006). Some of these rock bodies are spatially associated with massive sulfide deposits that include past and current Ni-Co producers. These ultramafic rock bodies range in size from a few meters to a kilometer in thickness and up to a few cubic kilometers in volume with about 40 being large enough to be of potential economic interest. Barnes and Lightfoot (2005) provide a summary of the historic estimates of the quantity of low grade Ni-sulfide in the TNB.

The total volume of ultramafic rock within the TNB approaches that of the komatiitic rock in the Yilgarn Craton, Australia. Unlike the relatively well-understood Western Australian counterparts (Barnes, 2004; Barnes et al., 2011a) there are, however, relatively few publications on the nature or composition of the ultramafic rock bodies of the TNB (Layton-Matthews, 2001;

Paktung, 1984; Peredery, 1979) and none on the nature of the disseminated Ni-sulfide mineralization hosted by them.

This paper reports new data on one such occurrence of low-grade, disseminated sulfide mineralization – the South Manasan ultramafic rock body and its associated Ni-Co-platinum group element (PGE) mineralization. The importance and uniqueness of this ultramafic rock body and the associated disseminated sulfide mineralization rests in both the extent of preservation of primary magmatic textures and in the unusual pentlandite and PGE-rich nature of the sulfides.

Regional Geological Setting

The TNB is a 400 km long, NNE-trending, richly mineralized (i.e., Ni-Cu-PGE sulfide deposits) thrust and fold belt situated on the north-western margin of the Archaean Superior Province in northern Manitoba, Canada (Fig. 1A). The TNB comprises, from oldest to youngest, reworked basement gneisses, Ospwagan Group metasedimentary rocks, mafic-ultramafic intrusive and volcanic rocks. The basement gneisses are interpreted to be derived from the adjacent Pikwitonei Granulite Domain, which was subjected to amphibolite to granulite-facies conditions from ca. 2720 to 2640 Ma (Heaman et al., 2011).

The overlying Ospwagan Group metasedimentary rocks were deposited in the Paleoproterozoic during rifting of the eastern margin of the Superior craton. The sequence of rocks is represented from base to top by the metaquartzites and metapelites of the Manasan formation, hybrid carbonate rocks of the Thompson formation, metapelites and iron formations of the Pipe formations, and metapelites and metaqaurtzites of the Setting formation (Fig. 1B).

Paleoproterozoic detrital zircons have been extracted from the Manasan and Setting formations yielding maximum ages for deposition of ca. 2.24 Ga and 1.97 Ga, respectively (Bleeker and Hamilton, 2001; Machado et al., 2011). A minimum age for the Ospwagan Group is provided by cross-cutting amphibolitized dykes interpreted to be part of the ca. 1880 Ma Molson dyke swarm and possibly co-magmatic nickel ore-bearing ultramafic sills, which intruded the Ospwagan Group supracrustals at all stratigraphic levels at ca. 1880 Ma (Bleeker, 1990; Heaman et al., 2009; Scoates et al., 2010).

Emplacement of a variety of mafic and ultramafic intrusive and volcanic rocks occurred during the latter stages of rifting of the Superior craton. This suite of rock is represented by ultramafic sills, mafic-ultramafic dykes of the Molson Suite and mafic-ultramafic rocks of the Bah Lake assemblage. The oldest mafic and ultramafic rocks are those of the Bah Lake assemblage, which are located at the stratigraphic top of the Ospwagan Group and have an age bracket of 1974 to 1890 Ma based on U-Pb zircon ages for crosscutting felsic intrusions (Zwanzig, 2005). In comparison, Thompson-type ultramafic sills have been dated at 1880 ± 5 Ma at Setting Lake (Hulbert et al., 2005) and 1880.8 ± 2.5 Ma at the Pipe II open pit based on U-Pb dating of baddleyite (Scoates et al., 2010). Molson dykes occurring within and outside of the TNB span ages both older and younger than the Thompson-type ultramafic sills (Heaman et al., 2009). However, a mafic Molson dyke from the Thompson Mine South Pit yielded an age of 1860.9 ± 2.1 Ma (Scoates et al., 2010). Field observations show that Molson dykes cross-cut an ultramafic sill in outcrop at Lower Ospwagan Lake (J. Macek, pers. commun. 2012), Pipe open pit, as well as diamond drill core from South Manasan (this study).

Deformation and metamorphism of the basement rocks and supracrustal sequence occurred during the Hudsonian Orogeny which resulted from the collision of the Churchill and

Superior provinces. This collisional event subjected the rocks of the TNB to polyphase deformation and amphibolite facies metamorphism (Bleeker, 1990). Bleeker (1990) recognized four main deformation events. D1 is interpreted to be a recumbent isoclinal folding event which produced nappe structures. The D2 event was responsible for the development of fabric under peak metamorphic conditions. The age of peak metamorphism has been constrained to 1776 - 1779 Ma based on dating of monazite grains (Couëslan et al., 2013). D3 is interpreted to be a sinistral transpression event responsible for producing dome and basin interference patterns; the type example being the Thompson Dome. As a result of deformation the ultramafic sills were deformed into boudins or cigar-shaped bodies and the original contact relationships were destroyed. Finally, the D4 event produced local brittle structures that cross-cut the main metamorphic fabric and offset the mineralized horizons.

The TNB can be divided into three regional, nested metamorphic zones – middle amphibolite facies, upper amphibolite facies, and granulite facies – which subparallel the strike of the belt and the regional D3–D4 structures (Couëslan and Pattison, 2012).

The majority of the economically important TNB ultramafic intrusions are located within the P2 pelitic schist member of the Ospwagan Group (e.g., Pipe, Birchtree) and at the contact of Thompson formation marbles and P1 iron formation member (Eckstrand et al., 1989; Peredery et al., 1982) (e.g., Thompson; Fig. 1B). There are considerable variations in the stratigraphy and metamorphic grade of Ospwagan Group metasedimentary rocks throughout the TNB (Peredery and Staff, 1982; Macek and Bleeker, 1989), but the recognition of the stratigraphic position of intrusions and mineralization underpins successful exploration. The stratigraphic record in Figure 1B provides an important foundation for stratigraphic and structural models of the TNB.

Mineralization in the Thompson Nickel Belt

Exploration using geophysical methods and diamond drilling begun in the 1950's (Zurbrigg, 1962) and resulted in the discovery of the Thompson, Birchtree, Pipe, Soab North and South, Moak, Manibridge and Bucko deposits, as well as a large number of significant Ni sulfide occurrences. The styles of sulfide mineralization in the TNB occur as three endmembers: (i) metasedimentary rock-hosted massive sulfide (Thompson), (ii) sulfide-matrix ultramafic (e.g. Birchtree, Soabs), and (iii) ultramafic-hosted disseminated sulfide (e.g. Pipe, South Manasan). The distribution of massive and semi-massive Ni-sulfide mineralization is heavily controlled by structural fabric. In the cases of Thompson and Pipe deposits important ore zones occur in dilation zones parallel to the fold axis (Gribbin et al., 2011). The sulfide assemblage is comprised principally of pyrrhotite and pentlandite with minor chalcopyrite. Locally, within the Birchtree and Thompson orebodies for example, arseno-sulfides are present whereas millerite and violarite are locally present within the Pipe orebody. The timing of sulfide mineralization at Thompson Mine is constrained to 1885 ± 49 Ma based on Re-Os determination from sulfide ore samples (Hulbert et al., 2005). The nickel content of sulfide ore (nickel tenor) is typically in the range of 2 to 14, with a narrow range of moderate tenor mineralization in the ultramafic-hosted deposits (~4-8 wt. % Ni) to a much wider range of tenors in metasediment-hosted mineralization (~2-16 wt. %) (Lightfoot et al., 2012). Rock types hosting ore include dunite, peridotite and pyroxenite.

Petrological Features of the Ultramafic Bodies of the Thompson Nickel Belt

The ultramafic bodies of the TNB are lensoid or tabular in shape and measure from less than one meter to about a kilometer in width (Peredery et al., 1982). The ultramafic intrusions are typically weakly differentiated with MgO-depletion trend towards the stratigraphic base and top, occasional weak gradational layering and occasional pyroxenitic upper contact zone (Peredery et al., 1982). These bodies all show the effects of deformation and most had been affected by metasomatism. Partially serpentinized peridotites are reported from the centers of North Manasan and Spur South ultramafic bodies (Layton-Matthews, 2001), locally within Ospwagan Lake and Muskeg City. Unserpentinized dunites and peridotites that show evidence of recrystallization occur at the Thompson Mine (Paktunc, 1983), Joey Lake and South Manasan (this study).

Alteration and metasomatism of the ultramafic bodies has been investigated by Layton-Matthews (2001) who reports that common assemblages are either: (1) serpentine ± magnetite ± brucite or (2) serpentine ± talc ± magnesite ± calcite ± biotite. The order of metasomatic alteration, from the oldest to the youngest is serpentinization, K-metasomatism, and carbonate metasomatism.

Two types of serpentinization are reported: (1) permeability-controlled (pseudomorphic and non-presudomorphic) and (2) fracture-controlled. Pseudomorphic serpentine is typically of the lizardite species and is often associated with fine-grained brucite ($Mg(OH)_2$), whereas the vein-type serpentine occurs either as antigorite or as chrysotile. Serpentinization is suggested to occur in the following reaction:

$$30Mg_{1.8}Fe_{0.2}SiO_4 + 41H_2O = 15Mg_3Si_2O_5(OH)_4 + 2Fe_2O_3 + 2H_2 + 9Mg(OH)_2$$

forsterite serpentine magnetite brucite

Brucite is found as a fine-grained, low-relief and low-birefringence mineral intergrown with serpentine with Mg as a major cation. Many of the serpentinized ultramafic rocks have loss on ignition (LOI) contents that exceed the structural H_2O capacity of serpentine (~16 wt. %) (O'Hanley, 1996). Ultramafic rocks with a significant carbonate component (>1 C wt. %) typically have >20 wt. % LOI, likely due to the contribution of magnesite (52.2 % CO2¬). However, serpentinized ultramafic rock with an insignificant amount of carbonate component (<1 C wt. %) typically have LOI in the 15-20 wt. % range. This is likely due to the contribution of brucite (30.9 wt. % H_2O).

K-alteration is generally accommodated by modal increase in biotite as two distinct morphologies: (1) porphyroblastic growth and (2) mineral intergrowths. In serpentinized rocks the porphyroblastic phlogopite forms <2 mm subhedral grains that cross-cut serpentinization fabrics with chlorite rims that penetrate along serpentine cleavage plains. In contrast, the late biotite porphyroblasts form <5 μm intergrowths that lie along cleavage plane of serpentine. The timing of this K-alteration event postdates serpentinization, but predates carbonate alteration.

Carbonate alteration is the youngest alteration phase in the TNB and appears to be unrelated to serpentinization. The dominant carbonate alteration mineral in ultramafic bodies in the TNB is magnesite, which can be accompanied by talc and calcite.

Geology and Mineralization of the South Manasan occurrence

Since the South Manasan ultramafic body rests beneath 10-30 m of overburden the following observations come from drill core and the interpretation of geophysical data. The ultramafic body was discovered by Vale (formerly INCO) in 1966 and by 1971 had been delineated by 23 diamond drill holes. Between 2008 and 2009 three additional diamond drill holes were cored and analyzed which led to the recognition of anomalous PGE mineralization associated with the occurrence of sulfide. Diamond drilling has intersected intervals of ultramafic rock of up to 220 m thickness which contains 1-5% fine-grained disseminated sulfide. Individual drill core samples within these intervals have yielded grades of up to 1.7% Ni with a TPM (Pt, Pd and Au) value of up to 1.5 ppm. The sulfide mineralization is dominated and characterized by the presence of interstitial and platy pentlandite accompanied by subordinate amount of pyrite and pyrrhotite. Chalcopyrite, heazlewoodite, cubanite and tochilinite locally constitute a trace component of the total sulfide in the rocks.

The South Manasan ultramafic body is sill-like with a boudinaged outline having a strike length of approximately 1200 m and maximum width of 220 m, but averaging 125 m width. The body dips steeply to the south-east with a depth extent of at least 1000 m, as demonstrated by diamond core drilling. Structurally, it is located on the eastern limb of the isoclinal, subvertical Birchtree-South Manasan synform (Fig. 1C and 1D). This synform is bounded by the Grass River mylonite zone to the east and the Churchill boundary fault to the west and is truncated by the Apussigamassi shear to the north and closed off by a steeply plunging macrofold at Pipe to the south. The S3 foliation and compositional banding in the area strikes NNE and the fold structure comprises a series of shallowly plunging non-cylindrical folds. The southern and

northern terminations of the South Manasan intrusion have a subvertical plunge, similar to the trend of mineralization and ultramafic intrusion at the Birchtree Mine, which is also attributed to F3 fold plunges.

The Ospwagan Group metasedimentary rocks in the immediate vicinity of the South Manasan ultramafic body have attained middle-amphibolite facies metamorphic grade based on regional isograds established by Coueslan and Pattison (2012); they have subsequently retrogressed to greenschist facies.

The South Manasan ultramafic body is believed to be of intrusive origin as it shows stratigraphically conformable contacts with the host Ospwagan Group metasedimentary rock. The stratigraphic younging direction within the intrusive body is not readily apparent from the trend of MgO content, but sill tops can be inferred from the stratigraphy of the host Ospwagan Group metasedimentary rocks. No flow differentiation, flow top breccias or spinifex textures are known at South Manasan.

The main rock type within this ultramafic intrusion is a cumulate-textured dunite that gradually transitions to serpentinite away from its core. Pervasive carbonate alteration of the dunite and serpentinite lithological units is strongest near to the contacts and along narrow shear zones within the intrusion.

Sampling and Analytical Methods

Samples of the intrusion were taken from three HQ sized (63.5 mm diameter) diamond drill cores (hole numbers 115175, 115191 and 115194) that intersected the South Manasan intrusion. The core was subdivided into rock units based on macroscopic mineralogical

observations, colour and texture. Continuous samples were taken from each of the rock units. Samples were sent to ALS labs, Actlabs and Geolabs for analysis. For each rock type the representative chemistry, along with the analytical method and detection limits is summarized in Table 1. Drill hole 115175, which intersects the ultramafic sill in its thickest part, was selected to showcase the geological observations. Figure 2A shows rock type, Ni and PGE concentrations, trace-element geochemistry and physical properties (e.g., density) plotted against the depth of the hole. Figure 2B shows rock type and whole-rock concentrations of SiO_2, Fe_2O_3, Al_2O_3, Cr, V, Sr and As plotted against the depth of hole.

Reconnaissance petrography of 97 polished thin sections yielded modal mineralogy, grain size and micro-textures for these samples. From this suite of samples a representative subset of polished thin sections was used for SEM-EDS analysis to document mineral chemistry: principally sulfide and textural relationships. The SEM-EDS system used was an Oxford Sight EDS (energy dispersive detector) mounted on a JEOL 6400 scanning electron microscope at the Central Analytical Facility of Laurentian University, Canada. Data were acquired at an accelerating voltage of 15 kV, a 1.005 nA beam current and with acquisition count times of 5-10 s, and a working distance of 15 mm. Jadeite, diopside, orthoclase, corundum, quartz, chalcopyrite, and pyrophanite were used as standards for the instrument calibration.

The mineral chemistry of olivine and serpentine were obtained by wavelength dispersive analysis using a CAMECA SX50 electron microprobe at Indiana University. An accelerating voltage of 15 kV was used. Beam current and peak counting time for major elements were 20 nA and 20 s, respectively. Nickel was analyzed at a beam current of 100 nA, a peak counting time of 100 s and a beam diameter of 10 μm. The detection limit for Ni under these conditions was about

60 ppm in olivine and about 100 ppm in serpentine. The accuracy of analysis was monitored using a reference material of similar compositions.

Ni tenor (i.e., wt. % Ni in 100% sulfide) was calculated using the following formula:

[1] $$\text{Ni tenor} = (Ni_{\text{whole-rock}} - Ni_{\text{silicate}})/S*39$$

where $Ni_{\text{whole-rock}}$ is the total Ni measured by whole-rock geochemical analysis and Ni_{silicate} is the amount of Ni measured in olivine and serpentine from the results of the electron microprobe analyses. The difference between $Ni_{\text{whole-rock}}$ and Ni_{silicate} qualitatively reflects the amount of Ni contained in the sulfide component of the sample of interest. Significant errors can occur when calculating tenor at sulfur values below 2.5 percent in olivine-rich rocks (Kerr, 2003). Consequently, in order to overcome this limitation in this study a cut-off of 0.2 wt. % was used due to the very low sulfur values. However, when taken as an average for a group of samples Ni tenor qualitatively reflected the sulfide variability across lithologies. To prevent unrealistically high Ni tenors the calculation was capped at 39 to reflect the pentlandite dominated sulfide assemblage observed in thin section.

TPM tenor (i.e., ppm (Pt+Pd+Au) in 100% sulfide) was calculated using a similar formula, also using a 0.2 S wt. % cut-off:

[2] $$\text{TPM tenor} = (Pt+Pd+Au)/S*39$$

The study is supplemented with the Canadian Mining Industry Research Organization (CAMIRO) dataset of whole-rock and mineral chemistry collected from a range of rocks from the TNB (Burnham et al., 2009).

Petrology of the South Manasan Intrusion

In this study six rock types are distinguished for the South Manasan intrusion based on the intensity of serpentine alteration, carbonate alteration and shearing of the dunite protolith (Table 2). Dunite-0 represents the freshest rock and dunite-5 the most altered. Representative photomicrographs of the textures observed in each lithology are shown in Figure 4, a generalized schematic summary of the progressive alteration is given in Figure 5 and an interpreted time of the formation of each observed mineral is given in Figure 6. In general, the degree of alteration is manifested by a change in silicate mineralogy and mineral chemistry, as well as physical properties obtained from drill core; these changes are also accompanied by a variation in sulfide composition and texture. Serpentine is present within all the samples analyzed, but ranges in abundance from <1 modal % to being a major component of the mode. Serpentine is intergrown with other phases: up to 25% of brucite and <1% of iowaite and pyroaurite. Serpentine and brucite are difficult to distinguish optically, hence and the amount of brucite is estimated instead using the whole-rock LOI and C content.

Dunite-0 is a medium grey adcumulate rock composed of 90% olivine, 5% serpentine and 5% chrome spinel and sulfide (Fig. 3A). Olivine crystals are tightly packed and have an adcumulate texture with interstitial serpentine, sulfide, chromite and chlorite (Fig. 3B). Olivine crystals are typically between 1 to 2 mm; yet 10 modal % are megacrysts ≤5 mm in diameter with rare twinning (Fig. 3B). In plane transmitted light olivine displays a weakly banded "dusty" internal texture defined by trails of abundant micron-scale inclusions (Fig. 3C). These inclusion trails are parallel within single crystals, but do not have a preferred orientation in the rock (Fig. 3C). Serpentine is present at grain boundaries and lining fractures within olivine (Fig. 3D, E).

Rounded intercumulus Cr-spinel grains range in size between 0.1 to 1 mm and occasionally carry inclusions of sulfide minerals. Carbonate veins that comprise <1 modal % and <1 mm in width locally crosscut the cumulate fabric (Fig. 3F). The sulfide assemblage is composed of 90% pentlandite, 10% pyrite and trace amounts of chalcopyrite. Pentlandite crystals range in size from 0.2 to 1 mm and commonly display a cuspate morphology that is typical of mineral phases that grow interstitial to other grains (Fig. 4A). Pyrite grains are an order of magnitude smaller than pentlandite (i.e., ≤0.1 mm) and occur as blebs and symplectic textured intergrowths within pentlandite (Fig. 4B). Chalcopyrite occurs as <0.1 mm size grains or elongated crystals within or proximal to pentlandite (Fig. 4C).

Dunite-1 is a dark grey adcumulate-textured rock comprising 50% olivine, 45% serpentine and 5% Cr-spinel and sulfide. The mineralogy is similar to dunite-0, but with a higher proportion of serpentine that occupies more space along olivine grain boundaries and cracks. The intercumulus Cr-spinel is often rimmed by a thin band of metamorphic aluminum-chrome spinel with a pitted texture and a halo of radiating chlorite platelets that penetrate the sulfide (Fig. 4C). The sulfide assemblage is similar to that in dunite-0; however, the sulfides are locally intergrown with chlorite platelets.

Dunite-2 is a black to green rock with remnant adcumulate texture composed of 80% serpentine, 10% olivine and 10% of magnesite, sulfide, spinel and chlorite. Mesh-textured serpentine pseudomorphs after olivine form a tightly packed, remnant-cumulate texture similar to dunite-0. The original cumulate texture of the dunite precursor rock becomes less apparent with an increasing overprint of patchy serpentinization. Veinlets of fibrous serpentine occur at sites of former fractures in olivine that transect the remnants of mesh-textured serpentinized olivine. Magnesite is found as patchy zones overprinting serpentinized olivine pseudomorphs and as

veins cross-cutting remnant cumulate texture. Pitted Cr-spinel occurs at sites of former intercumulus Cr-grains. Magnetite is found as two end-members: (1) micron-scale disseminations in black serpentinite and (2) discrete millimeter-size veinlets in green serpentinite. The sulfide assemblage is pentlandite-pyrite with an interstitial texture completely disrupted by a platy sulfide-gangue intergrowth (Fig. 4D) similar to that noted previously in dunites-0/1(Fig. 4C). In these intergrowths, the outlines of a group of sulfide platelets together define an interstitial texture, but each individual platelet is in contact with chlorite, serpentine or brucite (Fig. 4D). Within the adjacent serpentine, formerly adcumulate olivine, micron-scale disseminated crystals of heazlewoodite and intergrowths of chalcopyrite, cubanite or tochilinite with serpentine, pyroaurite or iowaite are found.

Dunite-3 is a grey to green rock with a locally sheared, remnant adcumulate texture comprising 75% serpentine, 15% magnesite and 10% sulfide, spinel, talc and chlorite. This rock is very similar to dunite-2, but contains more carbonate veins and has a locally sheared fabric. The sulfide assemblage ranges from angular aggregations of pentlandite platelets (Fig. 4E) to pyrrhotite stringers with pentlandite eyes.

Dunite-4 is a dark grey rock with a sheared, remnant adcumulate texture. This rock grouping is the most compositionally diverse of the 6 rock groups identified. It typically comprises 45% olivine, 40% serpentine, 5% magnesite, 3% chlorite and 7% sulfide, spinel and talc. The sulfide comprises pyrrhotite stringers containing pentlandite eyes (Fig. 4F).

Dunite-5 is a medium grey rock with a sheared texture with zones of remnant adcumulate texture comprising 50% serpentine, 30% magnesite, 10% dolomite, 5% talc and 5% sulfide, spinel and chlorite. The sulfide assemblage is similar to that of dunite-4 comprising pyrrhotite stringers with pentlandite eyes.

Throughout the intrusion late veins of serpentine and carbonate minerals cross-cut the primary features and the pseudomorphed fabric. The scale of the veins ranges from 0.1 to– 2 mm in fresh dunite (dunite-0) to several meters of sheared ultramafic rock invaded with carbonate minerals.

The progression from dunite-0 to dunite-5 generalized in Figure 5 and 6 highlights the important features summarized above and includes: (1) early grain boundary localized alteration of cumulate- and adcumulate-textured olivine which progresses in abundance (Fig. 5A, B); (2) presence of interstitial sulfide dominated by pentlandite, but with variably textured pyrite, which includes symplectite, and development of a bladed intergrowth with chlorite (Fig. 5B); (3) further alteration of olivine which forms a pervasive replacement by serpentine and magnesite but with preservation of the cumulate texture (Fig. 5C, D), eventual loss of olivine cores in this altered rock (Fig. 5D vs. 5C) along with concomitant development of an abundance of the bladed texture interstitial sulfide with chlorite near chromite (Fig. 5B, C, D); and (4) loss of the cumulate texture in the most advanced stages of alteration (Fig. 5E, F) and formation of cross-cutting magnesite veinlets and sulfide blebs, the latter due to the shearing out of the interstitial-textured sulfide domains (Fig. 5F).

Physical properties

There is a strong correlation among density, magnetic susceptibility and intensity of alteration and metamorphic foliation; the latter two corresponding to the increase in the concentration of both LOI and C. In Figure 7A, a plot of density versus magnetic susceptibility with symbols sized to wt. % C and colour-coded by lithology, the variation in density can be seen to range from 3.0-3.3 g/cm^3 in the freshest dunite-0 samples to 2.4-2.6 g/cm^3 in the serpentinized dunite-2 samples. Carbonate altered samples (dunite-3 to 5) occupy the intermediate range of 2.6-3.1 3.0-3.3 g/cm^3. This increase in density between the most serpentinized rocks (dunite-2) and carbonate altered rocks (dunites-3 to 5) corresponds to increasing amounts of magnesite (see C wt. % bubbles) which has a density of 3.01 g/cm^3. The variation of magnetic susceptibility, from 50-2,200 (SI units) in fresh dunites to 10,000 in serpentinized dunites, reflects the breakdown of olivine to serpentine and brucite which is accompanied by the formation of magnetite (O'Hanley, 1996). The degree of carbonate alteration is interpreted to be proportional to the carbon content, which ranges 0.13-2.87 wt. % C in the freshest dunites to 0.08-6.05 wt. % C in altered and serpentinized dunites.

Figure 7B is a plot of density versus LOI with symbols sized to C concentration and colour-coded by lithology; this plot shows that the LOI ranges between 1 and 7 wt. % in the fresher dunites (dunites-0 and 1) and between 12 and 26 wt. % in the altered and serpentinized dunites (dunite-2 to 5). The increase in concentration of LOI is interpreted to reflect the combined effects of serpentinization and carbonate alteration of the dunites. Serpentinized dunites (dunite-2) have 15-20 wt. % LOI range and correspond to a serpentine-brucite mixture.

LOI values greater than 20 wt. % tend to be found in carbonate altered rocks, which is consistent with the 52.2 wt. % LOI content of magnesite.

The integration of the physical properties (density and magnetic susceptibility) and chemical composition (wt. % LOI and C) provide a robust way to identify the both the alteration assemblages present and the intensity of this alteration of the dunite protolith.

Geochemistry of the South Manasan Intrusion

Major and minor element geochemistry

Whole-rock geochemical data are summarized in Table 1A, where the average composition, standard deviation and range of abundance of major element oxides and C wt. % for each of the 6 rock types are shown. Table 1B shows the range in concentration of trace elements that are above the limit of determination for the analytical methods used (see Appendix A). A subset of key geochemical and physical attributes is plotted against depth in a representative drill hole (115175) that cuts through the stratigraphy of the intrusion from the top in the West to the base in the East (Figs. 1B, C and 2).

The most abundant major element oxides in the rocks of the South Manasan intrusion are MgO and SiO_2, which together make up 65–85 wt. % of the whole rock; Fe_2O_3 comprises 5.4 – 13.6 wt. % of the whole rock (Fig. 2B). The high concentrations of MgO, SiO_2 and Fe_2O_3 are consistent with the olivine and serpentine content of the intrusion. The combined concentrations of TiO_2, Al_2O_3, MnO, CaO, Na_2O and K_2O typically do not exceed 5 wt. % in any of the samples, and this is consistent with <10% interstitial minerals.

Samples from the top third and the bottom third of the intrusion are serpentinized and carbonate altered (dunite-3 through 5) as indicated from their high LOI (up to 26.3 wt. %) and wt. % C values (up to 6.05 wt. %), variable density values (2.45-3.23) and MgO concentrations (25.4-41.7 wt. %) (Fig. 2A). The core of the intrusion comprises fresh dunites (dunite-0) and variably serpentinized dunitic rocks (dunite-1 and 2) that on average have slightly higher MgO concentrations (34.9-47.8 wt. %) (Fig. 2A). Whole-rock compositions are corrected for alteration by the removal of LOI, which reduces the range in MgO concentration. Recalculated to volatile-free composition, the carbonate-altered and serpentinized parts of the intrusion have MgO concentrations of 30.6-51.6 wt. %, whereas the fresh dunites have 40.9-51.1 wt. % MgO.

Samples from the South Manasan intrusion have low TiO_2, Al_2O_3, MnO, CaO, Na_2O and K_2O, as well as concentrations of incompatible trace elements which fall below the detection limit of the analytical methods (Table 1). Figure 2B shows Fe_2O_3, Al_2O_3, Cr, V and Ti against the depth of hole where there is a small, but noticeable enrichment of the above elements in the lower part of the intrusion corresponding to rock unit dunite-4. However, this enrichment is intermittent over about 50 core meters before values approach background levels. Relative to geochemical transects through Thompson-type ultramafic rocks, there is no evidence to suggest that there are more differentiated marginal phases of the South Manasan intrusion such as the types described by Peredery (1982) and Layton-Mathews (2001).

The range of whole-rock Cr abundances is relatively narrow at 688 – 3,490 ppm with an average value for all samples of 1,317 ppm. Average whole-rock Cr content is reported by rock type in Table 1. Dunite-4 is characterized by elevated Cr (average 2,756 ppm) relative to fresh dunite-0 (average 1,572). Although dunite-4 is serpentinized and carbonate altered, its Cr concentrations are unusually high. There is no clear correlation between the presence of Cr-

spinel and nickel sulfide content of the ultramafic rock. The only major contributors to the whole-rock Cr budget are Cr-spinel and chlorite.

Nickel and PGE sulfide mineralization

Table 1C illustrates Ni, Cu, S and precious metal concentrations in each of the rock types of the South Manasan intrusion. Variations in the whole-rock Ni concentrations with stratigraphic position in the intrusion are shown in Figure 2. Nickel concentrations vary from 0.2 to 1.7 wt. %; the highest concentrations are associated with sulfide mineralization located in the upper half of the intrusion. The elevated Ni concentrations are associated not only with the fresh dunite (dunite-0), but also with the serpentinite (dunite-1 and 2). Rocks with elevated Ni contents typically have elevated Ni tenor (28-39 wt. % in 100% sulfide) and TMP (Pt+Pd+Au) tenor of 21-28 ppm in 100% sulfide.

The variation of Pd versus Ni and Pd versus Pt are shown in Figure 8A and 8B. The trend of Pd versus Ni is a tight array (R^2=0.93) with a slope of 1.73 and an intercept of 0.3, but there are a few dunite-2 samples which fall above the array at Ni concentrations of 0.8-1.2 wt. %. The trend of Pd versus Pt is a tight array (R^2=0.987) with a slope of 0.41 and an intercept of 0. A small number of high quality analyses of the six platinum group elements and gold (Table 1B, Data repository 2) show that the ratios of Pd/Ir (R^2=0.987, slope 0.082), Pd/Os (R^2=0.97, slope 0.087) and Rh/Ru (R^2=0.952, slope 3.697) are constant in rocks which show a range in degree of alteration.

Variation in Ni tenor is shown on a plot of wt. % Ni versus wt. % S as a function of rock type in Figure 8C. The fresh dunites and serpentinized dunites (dunite-0, 1 and 2) define a tight trend of increasing Ni with S that corresponds to a Ni tenor of 25-39 wt. %, and for the same

rocks the TMP tenor is 21-28 ppm. Some of the serpentinized and weakly carbonate altered dunites (dunite-2 and 3) have a Ni tenor of 15-25 wt. % and for the same rocks the TMP tenor is 10-20 ppm. The carbonate altered rocks (dunite-4 and 5) plot on a shallower trend with a Ni tenor of 10-15 wt. %; these rocks have a correspondingly low TPM tenor. A histogram of Ni tenor shows a bimodal distribution with populations centered at 39 wt. % and 14 wt. % (Fig. 8D).

Mineral chemistry of the silicate and oxide phases

Figure 9A shows a plot of mineral chemistry of olivine and serpentine on an axis of Mg# (Mg at. % / [Mg at. % + Fe at. %]) versus Ni wt. %. The average forsterite content of olivine from the South Manasan intrusion is Fo91 with values ranging from Fo89 to Fo93; the average nickel content is 0.25 ± 0.08 wt. % and ranges from 0.15 wt. % to 0.31 wt. % (Fig. 2). The average Mg# of serpentine is 97.16 ± 3.40 and ranges from 90.06 – 99.57; the average Ni content is 0.11 ± 0.22 wt. % and a range from not detected to 0.51 wt. % Ni (Fig. 9A).

The composition of serpentinized whole-rock samples recalculated on a volatile-free basis is shown on a Pearce element diagram (Fig. 9B), where the atomic ratios of Si/Ti and ([Fe+Mg+Mn]/2)/Ti are plotted. The figure shows a single array for the vast majority of the samples which follows the control line. The low content of Ti is consistent with a negligible contribution of trapped liquid or pyroxene to the mineral assemblage.

The compositional diversity of serpentinite samples in the altered dunites is shown on a plot of SiO_2 versus FeO (Fig. 9C). The fresh olivine analyses anchor the low SiO_2 end of a tight array which passes through the compositions of serpentine from dunite-0 and extends to the

composition of dunites-1 and 2. Carbonate altered lithologies (dunite-3 through 5) tend to plot above the high SiO_2 end of the array produced by serpentinization.

Spinel is a minor mineral phase comprising up to 3 modal % of the rock. It is found as three end-members: (1) an Al-rich (average 17.0 wt. % Al_2O_3) Cr-spinel that has a subrounded shape and a grain size of 0.1 – 1 mm; the grains are localized towards the center of the intrusion which comprises the dunites-0, 1 and 2 rock types. In these rocks the chromite is interpreted to be a primary magmatic mineral (Figs. 10A and B); (2) an Al-poor (average 3.2 wt. % Al_2O_3) Cr-spinel with a pitted texture that is found as a rim on the primary magmatic spinel (Figs. 10A through D); and (3) finely disseminated and stringy magnetite is associated with serpentine (Figs. 10E, F). The compositional variations of spinel are summarized in Table 3 and presented in ternary diagrams (Fe-Al-Cr, Mg-Al-Cr) in Figure 11. In the latter diagrams it is observed that the core areas are relatively Al and Mg rich, whereas the rim areas characterized by a pitted texture are relatively Fe and Cr-enriched. The width of these pitted margins corresponds to the degree of host-rock alteration, such that the Cr-spinels in the least altered samples have the thinnest Al-poor rim (Fig. 10A) and Cr-spinels in the more altered samples have the thickest Al-poor rim (Fig. 10B). In some grains the degree of replacement reaches an apogee and there is very little of the primary core remaining. (Fig. 10D). The development of the Al-poor spinel rims is also associated with the development of radiating chlorite grains that penetrate the adjacent interstitial sulfide. Figure 4C illustrates this texture showing the intergrowth of sulfide and chlorite in reflected light, whereas Figure 10C shows a backscatter electron image of this texture.

Chlorite is a minor mineral phase comprising up to 3 modal percent. The compositional variation of chlorite is summarized in Table 3, where it can be seen that chlorite is Mg-rich

(average 34.94 wt. % MgO) and relatively Al-rich (average 14.38 wt. % Al_2O_3) compared to the Cr-spinel rims that are depleted in these elements.

Mineral chemistry of the sulfides

Sulfides constitute a small, but economically interesting component of the South Manasan ultramafic body. The principal sulfide minerals are pentlandite (0.5 – 5 modal %), pyrite (0.05 – 0.1 modal %) and chalcopyrite (0.05 – 0.1 modal %). Pyrrhotite is an important mineral within the carbonate altered lithologies (dunites-3, 4 and 5) with concentrations approaching 0.5 modal %. Heazlewoodite is also present, but occurs within the serpentine matrix in concentrations of less than 0.1 modal %.

Pentlandite has a diverse morphology with 3 principal habits: (1) interstitial to olivine cumulate (Figs. 4A and 10C), (2) platy aggregations intergrown with chlorite within remnant interstitial outlines (Figs. 4D, 4E, 10E and F), and (3) pentlandite eyes within pyrrhotite (Fig. 4F). The variation in the Ni (26 – 43 wt. %) and Co (0 – 1.5 wt. %) contents of the pentlandite are both greater than that observed in the ores of the Thompson deposit (Fig. 12B). Interstitial pentlandite found in dunite-0 has an average 34.6 wt. % Ni and 0.68 wt. % Co, whereas the platy pentlandite within remnant interstitial outlines found in dunite-2 averages 38.9 wt. % Ni and 1.11 wt. % Co. Pentlandite as eyes in pyrrhotite stringers found in dunite-5 averages 31.8 wt. % Ni and 0.67 wt. % Co.

Pyrite is found together with pentlandite as symplectic intergrowths and the Ni content of this pyrite ranges from below detection limit (0.5 wt. %) to 1.5 wt. %, whereas the Co content ranges from below detection limit (0.5 wt. %) to 2.7 wt. % (Fig. 12C).

Back-scatter electron images of several polished thin sections were completed in order to establish the nature of the hosts for the precious metal phases (Pt, Pd, Au), but no precious metal minerals were found. Based on a strong linear correlation of the Ni to TMP with an R^2 value of 0.93 (Fig. 8A) it is inferred therefore, that PMs are hosted in the pentlandite. The relationship between Ni and TPM can be expressed in the following equation:

[3] $$Ni = 1.16*TPM + 0.29$$

The intercept of 0.29 is in-line with Ni concentrations measured in olivine at 0.25 wt. % ± 0.08 and serpentine at 0.11 wt. % ± 0.22 (Fig. 9A).

Discussion

The South Manasan intrusion contains between 1 and 5 modal % disseminated sulfide with Ni and TPM concentrations of 0.2 – 1.7 wt. % and 0.05 – 1.5 ppm, respectively. The sulfide assemblage varies from pentlandite-dominated to pentlandite-poor and corresponds to an extremely wide range of metal tenors: between 5 and 39 wt. % Ni and 4 to 38 ppm TPM in 100% sulfide. The metal tenors of these sulfides are much higher than those typical of the Thompson deposit, which have values of 8-14 wt. % Ni (Lightfoot et al, 2012). The host rocks comprise variably altered dunites ranging from essentially fresh to serpentinized to carbonate altered. At issue is the extent to which the compositional diversity in the sulfides is a product of primary magmatic processes versus the effect of redistribution during serpentinization and carbonate alteration.

Relative contributions of primary magmatic versus secondary alteration processes in the South Manasan intrusion

The alteration history of South Manasan dunite, from a primary magmatic rock to serpentine and carbonate altered dunite, has been reconstructed using petrographic observations paired with whole-rock and mineral chemistry. Figure 5 is a schematic representation of mineral transformations as they would appear in a typical thin section and forms the basis for discussion of the step-by-step transformation of primary olivine, chromite, pentlandite, pyrite and chalcopyrite to secondary serpentine, chlorite, magnesite and pyrrhotite. The images in Figure 5 are complemented by Figure 6 and provide a paragenetic sequence for the formation of each mineral during magmatic stage, serpentine alteration and carbonate alteration.

Figure 5A shows the least altered rocks located near the center of the South Manasan intrusion (dunite-0); they comprise some of the freshest rocks in the TNB. Within dunite-0 the sulfide assemblage comprises 85% pentlandite occupying interstitial space between olivine, 10% pyrite in symplectic intergrowths with pentlandite and 5% chalcopyrite occurring as euhedral crystals in contact with pentlandite-pyrite or on its own (Fig. 4A, 4B). The same assemblage of minerals is observed as small inclusions in chromite crystals (Fig. 4C and 10D). The true thickness of dunite-0 has been established based on drillcore intersection in borehole 115175 (Fig. 2) and is estimated at 100 m. Dunite-0 exhibits a dominantly adcumulate texture with 120° grain boundaries (Fig. 3B). Paktunc (1984) describes olivine from ultramafic boudins in the Thompson deposit which appears to have been recrystallized and the textures are often granoblastic. The freshest dunites from the South Manasan intrusion locally develop granoblastic and megacrystic textures and sometimes olivine is twinned, but the majority of the rocks are cumulate-textured with no clear record of recrystallization (Fig. 3B). A primary magmatic origin

for these rocks is suggested based on the following evidence: (1) the textures comprise adcumulate olivine with minor amounts of serpentine and brucite (Fig. 3). In other parts of the intrusion, where olivine is thoroughly serpentinized and carbonate altered, this texture is still preserved; (2) the sulfides display an interstitial morphology at olivine triple junctions and occur along olivine boundaries (Figs. 4A, B, C); (3) the Pt/Pd ratios (Fig. 8B) of 2.36 ± 0.26 are similar to values obtained from komatiitic Ni deposits of the Yilgarn Craton (Barnes and Weihua, 2012); (4) the compositional range of serpentine mineral chemistry, when taken on volatile-free basis, plots on an array that points towards average olivine composition (Fig. 9C). The points plotting furthest from the olivine composition are also displaced above the serpentinization array and correspond to the contribution from carbonate alteration; (5) the whole-rock MgO values, when recalculated to volatile-free status, are in the range of 30.6 to 51.6 wt. % which indicate a dunitic composition (Table 1A).

Figures 5B through F illustrate the primary magmatic features of the intrusion overprinted by serpentinization and carbonate alteration. The stratigraphically upper portion of the intrusion is dominated by serpentine alteration (dunite-1 and 2) with mostly preserved cumulate textures (approximately 90 m true width), whereas the stratigraphically lower position of the intrusion is serpentinized and carbonate altered (dunite-3, 4 and 5), and is considerably more sheared (approximately 80 m true width) (Fig. 2).

Figure 5B shows the earliest style of alteration, which is the gradual serpentinization of olivine along grain boundaries and crystal fractures (dunite-1). Figure 5C exemplifies the partial development of pseudomorphing serpentinization with olivine cores locally still intact (dunite-2). Figure 5D represents the completion of the serpentinization process and the gradual onset of carbonate alteration (dunite-3). Serpentinization of olivine is accompanied by the formation of

magnetite; first, as fine dusting and later as mm-scale veinlets. Iowaite appears early in the serpentinization process, as it crosscuts the early serpentine and brucite, but is itself crosscut by magnetite veinlets (Fig. 10E). Magmatic Cr-spinel with a euhedral form acquires a pitted texture on its rims which is considered to be of metamorphic origin and is accompanying radiating plates of chlorite (dunite-1 in (Figs. 10A and B)) until all of the Cr-spinel takes on the pitted texture (dunite-2 in (Fig. 10D)). The transformation of magmatic Cr-spinel to metamorphic Cr-spinel is accompanied by the loss of Mg and Al which it then taken up by the new chlorite that forms around this metamorphic Cr-spinel and is therefore, rich in Mg and Al (Fig. 11). The sulfide assemblage is similar to that found in the fresh dunite (dunite-0), but has a modified texture. Interstitial pentlandite (dunite-0 in Fig. 4A and B) becomes intergrown with chlorite platelets (dunite-1 in Fig. 4C), and all of the pentlandite is characterized by this texture (dunite-2 in Fig. 4D). In addition, <0.1 modal % of <5 μm disseminated heazlewoodite is found in the serpentine matrix.

Figures 5E and 5F illustrate carbonate alteration, which postdates serpentinization as observed from cross-cutting relationships and is manifested in the increase of modal % magnesite (up to 30%) with subordinate amounts of dolomite (to 12%) and talc (to 5%). Carbonate minerals occur either as pseudomorphs of earlier serpentine phases or as cross-cutting veins in dunite-3, 5 and 6. In dunite-4, serpentinization had not progressed to completion at the time of the onset of carbonate alteration which may be attributed to the strong shearing in dunite-4 that enhanced the permeability of the rock and allowed preferential access to the later CO_2-bearing fluids. Platy pentlandite and pyrite lose their interstitial outlines and progressively deform along gangue intergrowths. The resulting sulfide texture comprises <0.1 mm angular plates of pentlandite (dunite-3 in Fig. 4E). Samples of rock that illustrate the greatest

deformation (dunite-4 and 5) develop stringers of pyrrhotite (Fig. 4F). The intergrowth textures of sulfide and chlorite are no longer observed in these rocks.

Origin of the interstitial pentlandite and pentlandite-pyrite intergrowth

Dunite-0 has a primary interstitial sulfide assemblage consisting of pentlandite and pyrite with minor chalcopyrite. This is an unusual assemblage for primary magmatic sulfide deposits (Naldrett, 2004). However, Harris and Nickel (1972) describe this assemblage from the Texmont A and C deposits in the Abitibi belt of Ontario, Canada. Pentlandite and pyrite intergrowths are also found in the Betheno deposit in the Agnew-Wiluna belt, Western Australia and Santa Rita deposit in the Itabuna-Salvador-Curaca belt, Brazil, which are both ultramafic-hosted low-grade Ni sulfide deposits (Barnes et al., 2011a; Barnes et al., 2011b). Based on experimental data it has been estimated that tie lines between pentlandite and pyrite are established at about 280°C (Misra and Fleet, 1973), thus well below the temperature of primary formation for the South Manasan intrusion. In a similar experiment by (Craig 1973), a compositional range of S, Fe and Ni was subjected to two stage annealing, fist at 400°C and then at 200°C. These experimental runs produced synthetic pentlandite-pyrite textures similar to those observed in the South Manasan intrusion.

Pentlandite-pyrite at South Manasan within fresh dunite (dunite-0) comprises 90% pentlandite and 10% pyrite resulting in a composition of 51.8 at. % S, 23.9 at. % Fe, 23.8 at. % Ni and 0.6 at. % Co (37.7 wt. %. S, 30.3 wt. % Fe, 31.3 wt. % Ni and 0.8 wt. % Co). Gibbs energy modeling based on experimental data provides a Ni at. % versus T/°C section at 47.1 S at. % (Waldner and Sitte, 2008). Given that the S at. % content of interstitial the South Manasan sulfides is sufficiently similar to the experimental data provided by Waldner and Sitte (2008) the

sulfides crystallized pyrrhotite at 1000°C and pentlandite at 640°C. The pyrrhotite-pentlandite assemblage was then recrystallized as pentlandite-pyrite at approximately 235°C.

Origin of the sulfide-chlorite intergrowth

Disseminated sulfides of the South Manasan occur in three principal morphologies: (1) interstitial cuspate grains, (2) to stacks of thin platelets with interstitial outlines, and (3) stringers (Fig. 12A). The principal reason for the development of thin plates of sulfide in place of interstitial grains is the growth of chlorite plates that penetrate the sulfide grain. The early development of this texture can be seen in sulfides of dunite-1 (Fig. 4C). The textural relationships between chlorite and sulfide indicate that both minerals grew at the same time and thus, resemble a magmatic texture. However, both the chlorite mineral and the pentlandite-pyrite assemblages are stable only at low temperatures. The stability field of chlorite extends between 100°C and 350°C (Caritat et al., 1993) and pentlandite-pyrite assemblage has been experimentally constrained below 235°C (Craig, 1973; Misra and Fleet, 1973; Waldner and Sitte, 2008). Although an exact analogue of the chlorite-sulfide texture has not been found in the literature, a comparable texture of Cr-spinel and chlorite has been reported from the Pedra Branca Mafic-Ultramafic Complex, Ceara, Brazil (Fleet et al., 1993). The resemblance is in both the pitted texture of Cr-spinel rims with laths of chlorite and in the composition of the Cr-spinel and the resulting chlorite. In the case of Pedra Branca Mafic-Ultramafic Complex the growth of Cr-spinel rims and chlorite is attributed to rock-fluid processes at low-grade metamorphic conditions.

Further along the alteration pathway, in dunite-2 the intergrowth of chlorite and sulfide reaches a culmination point and the formerly interstitial sulfide grains consist of tens of microns

wide by hundreds of microns long plates of sulfide, chlorite and serpentine (Figs. 4D, 10E and F). Some of the platy pentlandite grains are slightly curved, indicating influence of deformation. In the case of South Manasan ultramafic intrusion the growth of Cr-spinel rims is contemporaneous with the serpentinization of olivine; however, the timing of serpentinization is uncertain.

The timing of serpentinization and carbonate alteration

The timing of serpentinization in the TNB has been addressed by Peredery (1979) and Bleeker and Macek (1996) who suggested that it represents late retrograde (post-metamorphic) serpentinization. Layton-Matthews (2001) suggested that deformation along ultramafic body contacts and the absence of thick metamorphic aureoles in the Ospwagan metasediments may indicate pre-metamorphic serpentinization, assuming the ultramafic sills were intruded into previously dehydrated metasedimentary rocks. This study documented the presence of iowaite (Cl-rich species of the hydrotalcite group) in intergrowth with serpentine. The presence of abundant iowaite veins had been reported from several serpentinized mantle peridotites (Fruh-Green et al., 2004) and may indicate seafloor serpentinization.

Carbonate alteration clearly postdates serpentinization as evidenced by cross-cutting relationships. It is interpreted to have taken place during regional metamorphism in the TNB (Layton-Matthews, 2001 and this study).

The sulfide tenor of the South Manasan mineralization and diversity in TNB sulfide composition: relative roles of primary and secondary processes

Most disseminated sulfide mineralization in magmatic sulfide deposits hosted in fresh rocks has a magmatic origin where the abundances of metals in the sulfide assemblage is controlled by the processes of immiscibility, sulfide segregation and partitioning of metal into the sulfide phase. In these cases, the metal tenor of the sulfide is controlled by the R-factor (Campbell and Naldrett, 1979):

[4] $$Y1 = [D1*C0i*(R+1)]/(R+Di)$$

where, Y1 is the final concentration of metal i in the sulfide melt; R is the ratio of the mass of silicate magma to the mass of the sulfide, and C0i refers to the original concentration of metal i in the silicate magma before reaction with sulfide commenced.

In variably altered ultramafic intrusions there has been some debate on the relative roles of primary magmatic processes versus secondary alteration as a control on the composition of the sulfides. For example, the pentlandite-heazlewoodite-awaruite-millerite assemblage for the disseminated sulfides in the Dumont deposits in Quebec, Canada has been attributed to serpentinization-related Ni-enrichment of magmatic sulfides (Eckstrand, 1975). The occurrence of Ni-enriched sulfide assemblages within serpentinized rock has also been reported from Archaean dunites from Western Australia (Donaldson, 1981). Some studies of the Mt. Keith ultramafic body suggest that the elevated Ni concentrations in sulfide are a product of the incorporation of Ni into the sulfide from the silicate and the loss of S (Hopf and Head, 1998).

The Ni, PGE and Au ratios of the sulfides from the South Manasan intrusion have an unfractionated pattern; the ratios of these metals remained uniform even through the progressive

stages of alteration developed in dunite-0 through to dunite-5 (Fig. 8A and B). Although, it is possible that the metal concentrations in sulfide at South Manasan were uniformly enriched during alteration, it is far more likely that the ratios of the metals reflect a primary magmatic origin.

An estimate of the R-factor was obtained by using the abundances of metals in the South Manasan sulfides (normalized to 100% sulfide) from the least altered dunite-0. Estimates of Ni, Cu, and PGE abundance in the starting komatiite composition were adopted from Burnham et al., (2009), who performed a similar calculation for other TNB deposits. The partitioning coefficients used in the calculation of R-factor are summarized in Table 4 (Bezmen et al., 1994; Burnham et al., 2009; Fleet et al., 1999; McDonough and Sun, 1995; Peach et al., 1990). The concentrations were normalized to primitive mantle abundances (McDonough and Sun, 1995).

Figure 13A shows the range metal enrichment found in the South Manasan intrusion (n=12); the highest metal enrichment is found in the least altered samples for which an average trend line is shown (South Manasan average dunite-0). Figure 13B illustrates the metal enrichment pattern of South Manasan dunite-0 in relation to the range of metal enrichment of the TNB. The lowest metal enrichments in the TNB are found in the South Mystery ultramafic body, located in the northern part of the TNB. Prior to this study the highest metal enrichments in the TNB were found in the William Lake ultramafic body, located in the southern part of the TNB which is covered by Paleozoic sedimentary rocks. It can be seen the South Manasan has a pattern similar to the ultramafic rocks from the rest of TNB, with a positive Rh and Pd anomaly and negative Pt anomaly. The R-factor required to attain the metal concentrations observed in sulfide within in dunite-0 range from 500 to 2500 (Fig. 13C). These values are towards the upper limit of the values when compared to the range published for sulfides from the TNB (Burnham et al.,

2009), and are significantly higher than values estimated for the Thompson deposit (20-200) (Lesher et al., 2001). The high R-factor is consistent with S/Se ratios of 260, which are higher than primitive mantle, but lower than the range found in the Thompson deposit (range from Eckstrand et al., 1989).

The lowest Ni tenors and TPM tenors are found within sheared and carbonate altered rocks (dunites-4 and 5) (Figs. 8C and D). Carbonate alteration affects Ni and TPM contents in two ways: (1) these rocks contain pyrrhotite, and (2) the average Ni content of pentlandite of these samples is 32 wt. % versus 35 wt. % for dunite-0 hosted pentlandite (Fig. 12A). At the same time as Ni and TPM tenor decreases, the ratios of metals remain the same (Fig. 8A, B).

Figure 9C illustrates the transformation of olivine to serpentine; it is seen that most samples plot along the serpentinization array which is essentially an isochemical reaction (except for the addition of H_2O). Samples at the right end of the serpentinization array are displaced above the array due to the addition of some Fe. Preferential Fe partitioning into serpentines has been observed, but the mechanism is not fully understood (Evans et al., 2013). Since the sulfides constitute only 1-5 modal % and have a high surface area, the opportunity to accommodate excess Fe is present. Therefore, the addition of Fe to sulfide can dilute the magmatic concentrations of Ni and TPM in sulfide while preserving their magmatic ratios.

Comparison of the South Manasan intrusion to other Thompson Nickel Belt deposits

The South Manasan intrusion is clearly one of a large group of ultramafic bodies in the TNB and even though it is heavily deformed and metamorphosed it exhibits a similar set of features to other TNB ultramafic intrusions. These features include: (1) the stratigraphic position of South Manasan is like those of Pipe and Birchtree deposits, being located between the

Thompson and Pipe formation; (2) the size of South Manasan is on par with South Mystery, Pipe and Moak ultramafic bodies; (3) Ni-sulfide mineralization displays a pattern of PGE, Au, Ni and Cu enrichment similar to the rest of TNB (Fig. 13); (4) the alteration assemblage of South Manasan comprising serpentine, brucite, magnetite, magnesite and talc is representative of the vast majority of Thompson-type ultramafic bodies.

Several features of South Manasan make it unique in the TNB: (1) the pentlandite-dominated sulfide assemblage and the corresponding Ni tenor of 36 wt. % in 100% sulfide within fresh dunite; (2) the TPM tenors of South Manasan show an extreme degree of TPM enrichment (up to 28 ppm in 100% sulfide) relative to the rest of the TNB (Fig. 13); and (3) the higher MgO content of the host rocks. A rather uncommon feature in the TNB is the unserpentinized dunite core of the South Manasan intrusion. Only a small number of bodies, including some dunites and peridotites in the Thompson Mine (Paktunc, 1984), Joey Lake and Ospwagan Lake ultramafic bodies have been described as having significant portions of unserpentinized dunite in the core.

The significance of this observation is important at two levels. Firstly, the elevated metal tenors provide an opportunity to evaluate the potential for a high quality concentrate. Secondly, the potential exists for the discovery of a more heavily mineralized domain within the South Manasan intrusion that has similar high tenor, or for the discovery of another ultramafic body with a similar style of mineralization.

Comparison of the South Manasan intrusion to other global low grade ultramafic-hosted Ni deposits

In a global context, South Manasan can be compared with other examples of low-grade ultramafic-hosted Ni-(Cu-PGE) deposits. Examples include deposits which are actively mined (Mt. Keith, Jinchuan and Santa-Rita) as well as deposits that have large undeveloped resources (Yakabindie, Dumont, Betheno). Some important similarities and differences are summarized in Table 5.

The Mt. Keith ultramafic body is located in the northern part of the Yilgarn craton in Western Australia and hosts a deposit comprised of 506 Mt @ 0.55 Ni% (Grguric et al., 2006) in weakly to strongly serpentinized dunite and talc-carbonate altered dunite (Grguric et al., 2006; Hopf and Head, 1998). The sulfide mineralization comprises pentlandite, pyrite, millerite and heazlewoodite with a Ni tenor near 16 wt. % and TPM tenor in the low ppb range (Grguric et al., 2006). It is now generally accepted that Mt. Keith was formed as a result of sulfur saturation in an intrusive channel way (chonolith) as it made its way to the surface (Rosengren et al., 2005) or within a near-surface magma channelway (Goles, in press). The proportions of fresher ultramafic rock to talc-carbonate altered rocks are lower than those found in the South Manasan intrusion.

The serpentinized ultramafic rocks contain a rare Cl-rich mineral woodalite (Grguric et al., 2001), which is analogous to the presence of iowaite at South Manasan. Hence, it is possible that the process of serpentinization at South Manasan is similar to Mt. Keith. One key difference between South Manasan and Mt. Keith is the low-PGE abundance of the latter; a feature that is indicative of a different mantle source material or previous phase of sulfur saturation.

Jinchuan is a large low-grade Ni-sulfide deposit located in Gansu Province, China. The historic resource is believed to be 500 Mt @ 1.2% Ni and 0.7% Cu (Barnes and Tang, 1999). The deposit is hosted in dunite, peridotite, lherzolite and pyroxenite that comprise a dyke-like body 6 km long and up to 700 m wide with an outcrop area of 1.5 km^2. The mineralization comprises disseminated to net-texture pentlandite, pyrrhotite and chalcopyrite (Chai and Naldrett, 1992) and has a Ni tenor of 8-10 wt. % and a TPM tenor of 1-9 ppm (Song et al., 2009). The deposit was formed in a magma chonolith, probably at fairly high level of the crust, but the relationships are clearly intrusive (Lehmann et al., 2007). The intrusion is quite heavily serpentinized, but talc-carbonate alteration is rare (Chai and Naldrett, 1992). It is unlikely that he intrusion was serpentinized by the same process as at Mt. Keith and South Manasan intrusion due to the lack of Cl-rich minerals.

Santa-Rita is located in the Bahia Province in central-eastern Brazil. The deposit is believed to contain 569.8 Mt @ 0.52% Ni (Inwood, 2011) and is hosted in a layered intrusion with a series of differentiated dunite, websterite and gabbroic rocks (Barnes et al., 2011b). The sulfide mineralization comprises pentlandite and heazlewoodite within the harzburgites and orthopyroxenites with a Ni tenor 15-25% and low abundances of PGE. The localization of mineralization appears to be concentrated to a "reef", although not in the same sense as the Merensky and Bushveld reefs. Although the olivine-rich rocks of Santa-Rita are moderately serpentinized, the host rocks to most of the mineralization are not. Taken together all these features make St. Rita quite different when compared to South Manasan.

Dumont is also an example of a low-grade ultramafic system located in the Abitibi greenstone belt in Quebec, Canada. The resource is 1,665 Mt @ 0.27 % Ni (Ausenco, 2013). The deposit is hosted in a series of sulfide-rich horizons in the lower dunitic unit of the intrusion. The

mineralization comprises abundant pentlandite with lesser awaruite, heazlewoodite, and millerite with the awaruite-rich zones locally comprising ore horizons (Duke, 1986). As such, the Ni tenor varies depending on the ore zone mineralogy, but is generally estimated to range 30-80 wt. % based on the mini-plant composite sample assays (data from Ausenco, 2013). The TPM tenor is highest in the lower contact zone and does not exceed 3 ppm (data from (Brugmann et al., 1990). The host rocks are variably serpentinized and talc-carbonate alteration is developed. Textures described by Duke (1986) are very similar to those observed at South Manasan, but the talc-carbonate alteration is more extensive at Dumont. Dumont is a type locality for the model that has been used to explain the elevated Ni tenor through serpentinization (Eckstrand, 1975). There is no development of awaruite and millerite at South Manasan; it is not clear whether this simply reflects a more extreme loss of sulfur during serpentinization at Dumont.

Betheno is another large ultramafic-hosted disseminated Ni-sulfide body located in the northern part of the Yilgarn craton in Western Australia. No resource numbers were available in the public domain, but the body is approximately 100 m thick and 500 m long with an average Ni grade of 0.6 wt. %. The sulfide is hosted in a fresh to weakly serpentinized dunite and sulfide mineralization comprises pentlandite with subordinate amounts of pyrite and millerite. The Ni tenor is 32% and the TPM tenor is 5-6 ppm (Barnes et al., 2009). The host rocks of Betheno and the high Ni tenor sulfide mineralization is most similar to South Manasan from the examples reviewed; however, the South Manasan has a higher TMP tenor higher than that of Betheno at 27 ppm in fresh dunite-0.

Despite the presence of fresh dunite core and pentlandite-dominated sulfide assemblage, South Manasan represents a member in a spectrum of ultramafic-hosted styles of Ni-PGE sulfide mineralization. Our evidence points to a primary magmatic source for the sulfides, and the

elevated Ni and PGE tenor of the sulfides are attributed to R-factor processes rather than post-magmatic serpentinization. The variations in composition in Betheno, Jinchuan, and Santa Rita also appear to be magmatic in origin. The extent to which post-magmatic process have modified the composition of Dumont sulfides remains less certain as the sulfide assemblage is exceptionally Ni rich and contains awaruite, which is not a feature of South Manasan.

Conclusions

A detailed petrological and geochemical study of the Ni-PGE mineralized South Manasan ultramafic intrusion in the richly mineralized Thompson Nickel Belt, Manitoba, suggests the following:

1. South Manasan is an example of a TNB low-grade Ni deposit with unusually high Ni (28-39 wt. %) and PGE (21-28 ppm) tenors;
2. The sulfide assemblage of pentlandite-pyrite, which is atypical of low-grade ultramafic-hosted Ni deposits, is consistent with the current phase equilibria diagrams;
3. Primary magmatic textures preserved for both the silicates and sulfides (e.g., cumulates and cuspate-shaped interstitial sulfide) are integrated with variations in geochemistry to calculate an R-factor of 500-2500 for the mineralization, which makes South Manasan the highest tenor deposit in the TNB;
4. The style of low-sulfide and high-tenor mineralization at South Manasan makes this a new exploration style for targeting in the TNB;
5. Local and late-stage carbonate alteration has modified the pentlandite-pyrite sulfide assemblage to pyrrhotite-pentlandite;

6. The proposed model for South Manasan mineralization has implications for the genesis of other similar deposits and points to the lack of evidence for metal mobility during serpentinization.

Although there is great potential for discovery and development of high-grade Ni sulfide deposits in the TNB, the potential importance of the South Manasan style of mineralization rests in its position as a unique new style of low-grade Ni sulfide mineralization. Future exploration efforts are positioned to find higher grade equivalents, as well as other intrusions with a similar style of mineralization.

CHAPTER 3: Thesis Conclusions

The primary objectives of this research were presented in journal manuscript form in Chapter 2. The study consisted of two fundamental components. The first component was to document the mineralogical zonation and textures that are generated by serpentinization and carbonate alteration of cumulate ultramafic rocks. The second component was to assess the relative roles of primary magmatic and secondary alteration processes to the current composition of sulfide mineralization.

Based on the work presented in Chapter 2 six different rock types were defined based on the presence and intensity of serpentine and talc-carbonate alteration. The sulfide assemblage was found to co-vary with the host rock alteration; with a pentlandite-pyrite-chalcopyrite assemblage in the fresh to serpentinized dunites and a pyrrhotite-pentlandite-chalcopyrite assemblage in the sheared and carbonate altered dunites. Nickel tenor calculated from whole-rock geochemistry and corrected for silicate Ni content reflected the mineralogy observed in thin section. Fresh and serpentinized dunite-hosted sulfides had a Ni tenor of 28-39 wt. % Ni in 100% sulfide and serpentinized, sheared and carbonate altered dunite had a Ni tenor of 9-15 wt. % Ni.

Future research on the South Manasan ultramafic intrusion is suggested to concentrate in the following areas:

1. Olivine inclusions. All olivine crystals are filled with aligned micron-scale inclusions (Fig. 3D). Similar inclusion in olivine can be observed within the Molson dykes that are located away from the Hudsonian metamorphic overprint (Macek, pers. comm.). It is therefore likely that these inclusions were formed during the intrusion of these mafic and ultramafic bodies rather than during the Hudsonian metamorphic event. An experiment by Tingle et al., (1992) on a

single olivine crystal under 2kbar pressure and 1200°C in the presence of CO_2 fluid produced strikingly similar textures described as etch tubes. The nature and composition of olivine inclusions can cast light to the conditions at the time of Molson dyke and Thompson-type ultramafic intrusions.

2. The timing of serpentinization in the TNB remains unresolved. Peredery (1979), Bleeker and Macek (1996) have suggested retrograde (post-metamorphic) serpentinization. Layton-Matthews (2001) suggested that deformation along ultramafic body contacts and the absence of thick metamorphic aureoles in the Ospwagan metasediments allow the possibility of pre-metamorphic serpentinization, assuming the ultramafic sills were emplaced into already dehydrated metasediments. This study documented the presence of iowaite, a Cl-rich species of the hydrotalcite group in intergrowth with serpentine. The presence of abundant iowaite veins has been reported from several serpentinized mantle peridotites (Fruh-Green et al., 2004). However, it is unclear if iowaite is exclusive to seawater serpentinization. Cl isotopes have been used to trace the hydration source in seafloor serpentinites with negative values indicating seawater as the source of alteration fluid (Barnes and Sharp, 2006).

3. The mineral phase hosting TPM mineralization is suspected to be pentlandite based on the strong correlation of Ni and TPM in whole-rock samples (R^2=0.92). The strongest correlation is with Pd at R^2=0.93, followed by Pt at R^2=0.91, followed by Au at R^2=0.46. Backscatter electron reconnaissance scanning of several polished thin sections did not reveal discrete TPM phases. Although TPM mineralization may still exist as a separate from the sulfide phase, there is a good indication that TPM mineralization is hosted as solid solution in pentlandite.

4. The sulfide composition of the South Manasan intrusion is very rich in Ni and TPM; the ultramafic body is otherwise very similar to other Thompson-type ultramafic bodies. A

comparative study of other high Ni-tenor sulfides in the TNB, such as Bucko, Bowden and William Lake ultramafic bodies can reveal if their mineralization is primary or secondary in origin.

REFERENCES

Ausenco, 2013, Technical Report on the Dumont Ni Project, Launay and Trécesson Townships, Quebec, Canada.

Barnes, J. D., and Sharp, Z. D., 2006, A chlorine isotope study of DSDP/ODP serpentinized ultramafic rocks: Insights into the serpentinization process: Chemical Geology, v. 228, p. 246–265.

Barnes, S.-J., and Lightfoot, P. C., 2005, Formation of magmatic nickel-sulfide ore deposits and processes affecting their copper and platinum-group element contents, in Hedenquist, J. W., Thompson, J. F. H., Goldfarb, R. J., and Richards, J. P., eds., Economic Geology, 100th Aniversary Volume, p. 179-213.

Barnes, S. J., 2004, Introduction to nickel sulfide orebodies and komatiites of the Black Swan area, Yilgarn Craton, Western Australia: Mineralium Deposita, v. 39, p. 679-683.

Barnes, S. J., Godel, B. M., Locmelis, M., Fiorentini, M. L., and Ryan, C. G., 2011a, Extremely Ni-rich Fe–Ni sulfide assemblages in komatiitic dunite at Betheno, Western Australia: results from synchrotron X-ray fluorescence mapping: Australian Journal of Earth Sciences, v. 58, p. 691–709.

Barnes, S. J., Osborne, G. A., Cook, D., Barnes, L., Maier, W. D., and Godel, B., 2011b, The Santa Rita nickel sulfide deposit in the Fazenda Mirabela Intrusion, Bahia, Brazil: geology, sulfide geochemistry, and genesis: Economic Geology, v. 106, p. 1083-1111.

Barnes, S. J., and Tang, Z. L., 1999, Chrome spinel from the Jinchuan Ni-Cu sulfide deposit, Gansu province, Peoples Republic of China: Economic Geology, v. 94, p. 343-356.

Barnes, S. J., and Weihua, L., 2012, Pt and Pd mobility in hydrothermal fluids: Evidence from komatiites and from thermodynamic modelling: Ore Geology Reviews, v. 44, p. 49-58.

Barnes, S. J., Wells, M. A., and Verrall, M. R., 2009, Effects of Magmatic Processes, Serpentinization, and Talc-Carbonate Alteration on Sulfide Mineralogy and Ore Textures in the Black Swan Disseminated Nickel Sulfide Deposit, Yilgarn Craton: Economic Geology, v. 104, p. 539-562.

Bezmen, N. S., Asif, M., Brugmann, G. E., Romanenko, I. M., and Naldrett, A. J., 1994, Experimental determinations of sulfide-silicate partitioning of PGE and Au: Geochimica et Cosmochimica Acta, v. 58, p. 1251-1260.

Bleeker, W., 1990, Evolution of the Thompson Nickel Belt and its nickel deposits, Manitoba, Canada: Unpub. PhD thesis, University of New Brunswick, 400 p.

Bleeker, W., and Hamilton, M. A., 2001, New SHRIMP U–Pb ages for the Ospwagan Group: implications for the SE margin of the Trans-Hudson Orogen., Geological Association of Canada – Mineralogical Association of Canada Joint Annual Meeting, Program with Abstracts, 26, p. 15.

Brugmann, G. E., Naldrett, A. J., and Duke, J. M., 1990, The platinum-group element distribution in the Dumont sill, Quebec. Implications for the formation of Ni-sulfide mineralization.: Mineralogy and Petrology, v. 42, p. 97-119.

Burnham, O. M., Halden, N., Layton-Matthews, D., Lesher, C. M., Liwanag, J., Heaman, L., Hulbert, L., Machado, N., Michalak, D., Pacey, M., Peck, D., Potrel, A., Theyer, P., Toope, K., and Zwanzig, H., 2009, CAMIRO Project 97E-02, Thompson Nickel Belt: final report March 2002, revised and updated 2003, Open file OF2008-11, Manitoba Geological Survey.

Campbell, I. H., and Naldrett, A. J., 1979, The influence of silicate:sulfide ratios on the geochemistry of magmatic sulfides: Economic Geology, v. 74, p. 1503-1506.

Caritat, P. d., Hutcheon, I., and Walshe, J. L., 1993, Chlorite geothermometry: a review: Clays and Clay Minerals, v. 41, p. 219-239.

Chai, G., and Naldrett, A. J., 1992, Characteristics of Ni-Cu-PGE mineralization and genesis of the Jinchuan deposit, Nortwest China: Economic Geology, v. 87, p. 1475-1495.

Couëslan, C. G., and Pattison, D. R. M., 2012, Low-pressure regional amphibolite-facies to granulite-facies metamorphism of the Paleoproterozoic Thompson Nickel Belt, Manitoba: Canadian Journal of Earth Sciences, v. 49, p. 1117–1153.

Couëslan, C. G., Pattison, D. R. M., and Dufrane, S. A., 2013, Peleoproterozoic metamorphic and deformation history of the Thompson Nickel Belt, Superior Boundary Zone, Canada, from in-situ U-Pb analysis of monazite: Precambrian Research, v. 237, p. 13-55.

Couëslan, C. G., Pattison, D. R. M., and Tinkham, D. K., 2011, Regional low-pressure amphibolite-facies metamorphism at the Pipe II Mine, Thompson Nickel Belt, Manitoba, and Comparison of metamorphic isograds in metapelites and meta-iron formations: The Canadian Mineralogist, v. 49, p. 721-747.

Craig, J. R., 1973, Pyrite-pentlandite assemblages and other low temperature relations in the Fe-Ni-S system: American Journal of Science, v. 273-A, p. 496-510.

Donaldson, M. J., 1981, Redistribution of Ore Elements during Serpentinization and Talc-Carbonate Alteration of Some Archean Dunites, Western Australi: Economic Geology, v. 76, p. 1698-1713.

Duke, J. M., 1986, Petrology and economic geology of the Dumont Sill: an Archean intrusion of komatitic affinity in Northwestern Quebec: Geological Survey of Canada Economic Geology Report, v. 35, p. 56.

Eckstrand, O. R., 1975, The Dumont serpentinite a model for control of nickeliferous opaque mineral assemblages by alteration reactions in ultramafic rocks: Economic Geology, v. 70, p. 183-201.

Eckstrand, O. R., Grinenko, L. N., Krouse, H. R., Paktunc, A. D., Schwann, P. L., and Scoates, R. F. J., 1989, Preliminary data on sulphur isotopes and Se/S ratios, and the source of sulphur in magmatic sulphides from the Fox River Sill, Molson Dykes and Thompson nickel deposits, northern Manitoba: Current Research, Part C, Geological Survey of Canada, Paper 89-1C, p. 235-242.

Evans, B. W., Hattori, K., and Baronnet, A., 2013, Serpentinite: What, Why, Where?: Elements, v. 9, p. 99-106.

Fleet, M. E., Angeli, N., and Pan, Y., 1993, Oriented chlorite lamellae in chromite from the Pedra Branca Mafic-Ultramafic Complex, Ceara, Brazil: American Mineralogist, v. 78, p. 68-74.

Fleet, M. E., Crocket, J. H., Liu, M., and Stone, W. E., 1999, Laboratory partitioning of platinum-group elements (PGE) and gold with application to magmatic sulfide-PGE deposits: Lithos, v. 47, p. 127-142.

Fruh-Green, G. L., Connolly, J. A. D., Plas, A., Kelley, D. S., and Grobety, B., 2004, Serpentinization of Oceanic Peridotites: Implications for Geochemical Cycles and Biological Activity: The Subseafloor Biosphere at Mid-Ocean Ridges, Geophysical Monograph Series, v. 144, p. 119-136.

Grguric, B. A., Madsen, I. C., and Pring, A., 2001, Woodallite, a new chromium analogue of iowaite from the Mount Keith nickel deposit,Western Australia: Mineralogical Magazine, v. 65, p. 427–435.

Grguric, B. A., Rosengren, N. M., Fletcher, C. M., and Hronsky, J. M. A., 2006, Type 2 Deposits: Geology, mineralogy and processing of the Mount Keith and Yakabindie orebodies, Western Australia: Economic Geology, v. Special Publication 13, p. 119-138.

Gribbin, G., 2011, Geology and Mines Exploration: An Overview of the Ni Sulfide Deposits of the Vale Thompson Manitoba Operations, Canadian Institute Mining Metallurgy.

Hamilton, M. A., and Bleeker, W., 2002, SHRIMP U-Pb geochronology of the Ospwagan group: provenance and depositional age constraints of a Paleoproterozoic rift sequence, SE externides of the Trans–Hudson Orogen (abstract): Geological Association of Canada–Mineralogical Association of Canada, Joint Annual Meeting, Saskatoon, Saskatchewan, Program with Abstracts, v. 27, p. 44.

Heaman, L. M., Böhm, C. O., Machado, N., Krogh, T. E., Weber, W., and Corkery, M. T., 2011, The Pikwitonei Granulite Domain, Manitoba: a giant Neoarchean high-grade terrane in the northwest Superior Province.: Canadian Journal of Earth Sciences, v. 48, p. 205–245.

Heaman, L. M., Peck, D., and Toope, K., 2009, Timing and geochemistry of 1.88 Ga Molson Igneous Events, Manitoba: Insights into the formation of a craton-scale magmatic and metallogenic province: Precambrian Research, v. 172, p. 143–162.

Hopf, S., and Head, D. L., 1998, Mount Keith nickel deposit, in Berkman, D. A., and Mackenzie, D. H., eds., Geology of Australian and Papua New Guinean mineral deposits: Melbourne, The Australian Institute of Mining and Metallurgy, p. 307-314.

Hulbert, L. J., Hamilton, M. A., Horan, M. F., and Scoates, R. F. J., 2005, U-Pb zircon and Re-Os isotope geochronology of mineralized ultramafic intrusions and associated nickel ores from the Thompson Nickel Belt, Manitoba, Canada: Economic Geology, v. 100, p. 29–41.

Inwood, N., 2011, Mirabela Nickel. Santa Rita reserves and resources: (http://www.mirabela.com.au/reserves.asp)

Kerr, A., 2003, Guidelines for the calculation and use of sulphide metal contents in research and mineral exploration: Current Research: Newfoundland Department of Mines and Energy, v. 03-01, p. 223-229.

Layton-Matthews, D., 2001, Metasomatism of ultramafic intrusions in the Thompson nickel belt, Manitoba, Canada: Unpub. MSc thesis, Laurentian University, 128 p.

Layton-Matthews, D., Lesher, C. M., Burnham, O. M., Liwanag, J., Halden, N. M., Hulbert, L., and Peck, D. C., 2007, Magmatic Ni-Cu-platinum-group element deposits of the Thompson Nickel Belt, in Goodfellow, W. D., ed., Mineral Deposits of Canada, Special Publication No. 5. A Synthesis of Major Deposit-Types, District Metallogeny, the Evolution of Geological Provinces, and Exploration Methods, Geological Association of Canada, Mineral Deposits Division.

Layton-Matthews, D., Lesher, C. M., Liwanag, J., Halden, N., Burnham, O. M., Hulbert, L., Peck, D. C., and Keays, R. R., 2011, Mineralogy, Geochemistry, and Genesis of Komatiite-Associated Ni-Cu-PGE Mineralization in the Thompson Nickel Belt, Manitoba: Reviews in Economic Geology, v. 17, p. 123-143.

Layton-Matthews, D. M., Lesher, C. M., Burnham, O. M., Hulbert, L., Peck, D. C., Golightly, J. P., and Keays, R. R., 2010, Exploration for Ni-Cu-(PGE) Deposits in the Thompson Nickle Belt: Society of Economic Geology, v. Special Volume 15, p. 513-538.

Lehmann, J., Arndt, N., Windley, B., Zhou, M.-F., Wang, C. Y., and Harris, C., 2007, Field Relationships and Geochemical Constraints on the Emplacement of the Jinchuan Intrusion and its Ni-Cu-PGE Sulfide Deposit, Gansu, China: Economic Geology, v. 102, p. 75-94.

Lesher, C. M., Burnham, O. M., Keays, R. R., Barnes, S. J., and Hulbert, L., 2001, Trace-element geochemistry and petrogenesis of barren and ore-associated komatiites: Canadian Mineralogist, v. 39, p. 673-696.

Lightfoot, P. C., Macek, J., Stewart, R., Gribbin, G., and Mooney, S., 2012, Relative contribution of magmatic and post-magmatic processes in the genesis of the Thompson Ni-Co sulfide ore deposits, Manitoba, Canada., 11th International Nickel Symposium, Abstract: Guiyang China.

Macek, J. J., McGregor, C. R., and Zwanzig, H. V., 2004, Thompson Nickel Belt Project, Manitoba (part of NTS 63P): geology of the South pit, Thompson mine: Report of Activities 2004, Manitoba Industry, Economic Development and Mines, Manitoba Geological Survey, p. 135-148.

Macek, J. J., McGregor, C. R., and Zwanzig, H. V., 2005, Geology of the South pit (northwest shoulder), Thompson mine, Thompson, Manitoba (part of NTS 63P12), Manitoba Industry, Economic Development and Mines, Manitoba Geological Survey, Geoscientific map 2005-1, 1 colour map. scale 1:200.

Macek, J. J., Zwanzig, H. V., and Pacey, M., 2006, Thompson nickel belt geological compilation map, Manitoba (parts of NTS 63G, J, O, P and 64A and B): Manitoba Science, Technology, Energy and Mines, Manitoba Geological Survey, Open File Report 2006-33, 1 CD-ROM.

Machado, N., Gapais, D., Potrel, A., Gauthier, G., and Hallot, E., 2011, Chronology of transpression, magmatism, and sedimentation in the Thompson Nickel Belt (Manitoba, Canada) and timing of Trans-Hudson Orogen – Superior Province collision: Canadian Journal of Earth Sciences, v. 48, p. 295–324.

McDonough, W. F., and Sun, S.-S., 1995, The composition of the Earth: Chemical Geology, v. 120, p. 223-253.

McDowell, G., Stewart, R., and Monteiro, R., 2007, In-mine Exploration and Delineation Using an Integrated Approach: Ore Deposits and Exploration Technology, p. Presentation.

McGregor, C. R., and Macek, J. J., 2003, Sedimentary processes in the Ospwagan Group supracrustal rocks: Manitoba Industry, Economic Development and Mines, Manitoba Mining & Minerals Convention 2003, Winnipeg, Manitoba, November 13-15, 2003, 2003, p. Program, p. 42.

McRitchie, W. D., 1995, Mineral Development Potential in Manitoba - Nickel in the Southwest Extension of the Thompson Nickel Belt: Winnipeg, Manitoba Energy and Mines, p. 29.

Misra, K. C., and Fleet, M. E., 1973, The Chemical Composition of Synthetic and Natural Pentlandite Assemblages: Economic Geology, v. 68, p. 518-539.

Mudd, G. M., 2010, Global trends and environmental issues in nickel mining: sulfides versus laterites.: Ore Geology Reviews, v. 38, p. 9-26.

Naldrett, A. J., 2004, Magmatic Sulfide Deposits. Geology, Geochemistry and Exploration.: Berlin, Springer.

O'Hanley, D. S., 1996, Serpentines: Records of Tectonic and Petrological History: New York and Oxford, Oxford University Press.

Paktunc, A. D., 1984, Metamorphism of the ultramafic rocks of the Thompson Mine, Thompson Nickel Belt, Northern Manitoba: Canadian Mineralogist, v. 22, p. 77-91.

Paktunc, D., 1983, Petrology and geochemistry of some ultramafic rocks of the Thompson Nickel Belt and the Cuthbert Lake dikes of the Pikwitonei region, Northern Manitoba: Unpub. PhD thesis, University of Ottawa, 202 p.

Paktung, A. D., 1984, Petrogenesis of ultramafic and mafic rocks of the Thompson Nickel Belt, Manitoba: Contributions to Mineralogy and Petrology, v. 84, p. 348-353.

Peach, C. L., Mathez, E. A., and Keays, R. R., 1990, Sulfide melt–silicate melt distribution coefficients for noble metals and other chalcophile elements as deduced from MORB: Implications for partial melting.: Geochimica et Cosmochimica Acta, v. 54, p. 3379-3389.

Peredery, W. V., 1979, Relationship of ultramafic amphibolites to metavolcanic rocks and serpentinites in the Thompson Belt, Manitoba: The Canadian Mineralogist, v. 17, p. 187-200.

Peredery, W. V., and, and staff, g., 1982, Geology and nickel sulphide deposits of the Thompson belt, Manitoba: Precambrian sulphide deposits, v. Geol. Assoc. Can., H.S. Robinson memorial volume, p. 165-209.

Rosengren, N. M., Beresford, S. W., Grguric, B. A., and Cas, R. A. F., 2005, An intrusive origin for the komatiitic dunite-hosted Mounth Keith disseminated nickel sulfide deposit, Western Australia: Economic Geology, v. 100, p. 149-156.

Scoates, J. S., Wall, C. J., Friedman, R. M., Booth, K., Scoates, R. F. J., Coueslan, C., and Macek, J., 2010, Recent Progress in Determining the Precise Age of Ultramafic Sills and Mafic Dikes Associated with Mineralization in the Thompson Nickel Belt, Manitoba, Canada, Miscellaneous Release–Data 269, Ontario Geological Survey, p. 4.

Song, X.-Y., Keays, R. R., Zhou, M.-F., Qi, L., Ihlenfeld, C., and Xiao, J.-F., 2009, Siderophile and chalcophile elemental constraints on the origin of the Jinchuan Ni-Cu-(PGE) sulfide deposit, NW China: Geochimica et Cosmochimica Acta, v. 73, p. 404-424.

Tingle, T. N., Roedder, E., and II, H. W. G., 1992, Formation of fluid inclusions and etch tunnels in olivine at high pressure: American Mineralogist, v. 77, p. 296-302.

Waldner, P., and Sitte, W., 2008, Thermodynamic modeling of Fe-Ni pentlandite: Journal of Physics and Chemistry of Solids, v. 69, p. 923-927.

Zurbrigg, H. F., 1962, Thompson Mine Geology: Annual General Meeting, Ottawa, April, 1962, v. LXVI, p. 227-236.

Zurbrigg, H. F., 1963, Thompson Mine Geology: Canadian Institute of Mining and Metallurgy Bulletin, v. 56, p. 451-460.

Zwanzig, H. V., 2005, Geochemistry, Sm-Nd isotope data and age constraints of the Bah Lake assemblage, Thompson Nickel Belt and Kisseynew Domain margin: relation to Thompson-type ultramafic bodies and a tectonic model (NTS 63J, O and P): Report of Activities 2005, Manitoba Industry, Economic Development and Mines, Manitoba Geological Survey, p. 40-53.

Zwanzig, H. V., Macek, J. J., and McGregor, C. R., 2007, Lithostratigraphy and Geochemistry of the High-Grade Metasedimentary Rocks in the Thompson Nickel Belt and Adjacent Kisseynew Domain, Manitoba: Implications for Nickel Exploration: Economic Geology, v. 102, p. 1197-1216.

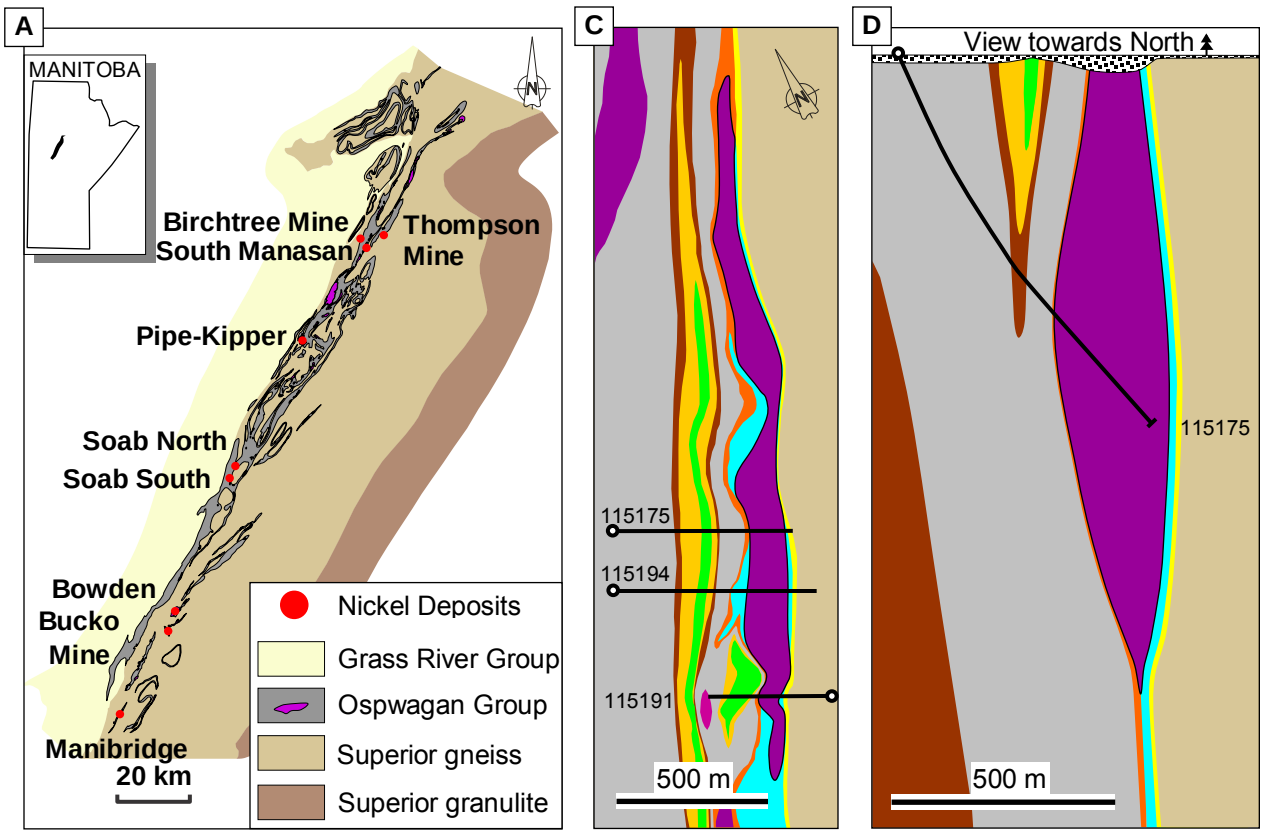

B

FORMATION	MEMBER	LITHOLOGY	SILICLASTIC COMPONENT 0% 100%	ULTRAMAFIC SILLS	NICKEL DEPOSIT POTENTIAL
BAH LAKE	B1, 2, 3	Mafic flows and sills			
SETTING	S1, 2	Upper clastic rocks: metapelite - quartzite			
PIPE	P3	Hybrid ferruginous rocks: metamorphosed ironstones; silicate, carbonate and oxide iron formations; chert, dolomite marble			
	P2	Impure siliclastic pelite: schist/gneiss, sulfide iron formation			**
	P1	Sulphide and silicate iron formations			*
THOMPSON	T3	Hybrid calcareous rocks: diopside-olivine-phlogopite-dolomite marble, calcareous metapelite schist, metamarlstone			
	T2				
	T1				
MANASAN	M2	Schist / veined gneiss, quartzite			
	M1				

Figure 1. Location of the South Manasan intrusion in the Thompson Nickel Belt, Manitoba, Canada. A) Simplified map of the Thompson Nickel Belt showing its location between the Proterozoic terrain in the west and the deformed Superior Province in the East; the belt extends NNE-SSW through central and southern Manitoba, Canada. After Macek (2006). B) Stratigraphy of the Ospwagan Group metasedimentary and metavolcanic rocks showing the position of the ultramafic sills and the peak development of Ni sulphide mineralization (after Macek et al., 2004; 2005). *denotes the stratigraphic setting of South Manasan, Birchtree and Pipe-Kipper ultramafic bodies in the P1 member. **denotes the stratigraphic setting of Thompson ore in the upper part of the P2 member. C) Plan map of the South Manasan Intrusion showing the projection of drillholes used in this study and the principal rock types. The

model was built using data from 28 drill holes. D) North-facing cross-section through South Manasan intrusion centered on borehole 115175 showing the geology logged in drill core. Shades of purple denote the zonal alteration from fresh dunite to serpentine altered and carbonate altered dunite. Note that bedrock is covered with 10-30 m of overburden which prevents surface mapping.

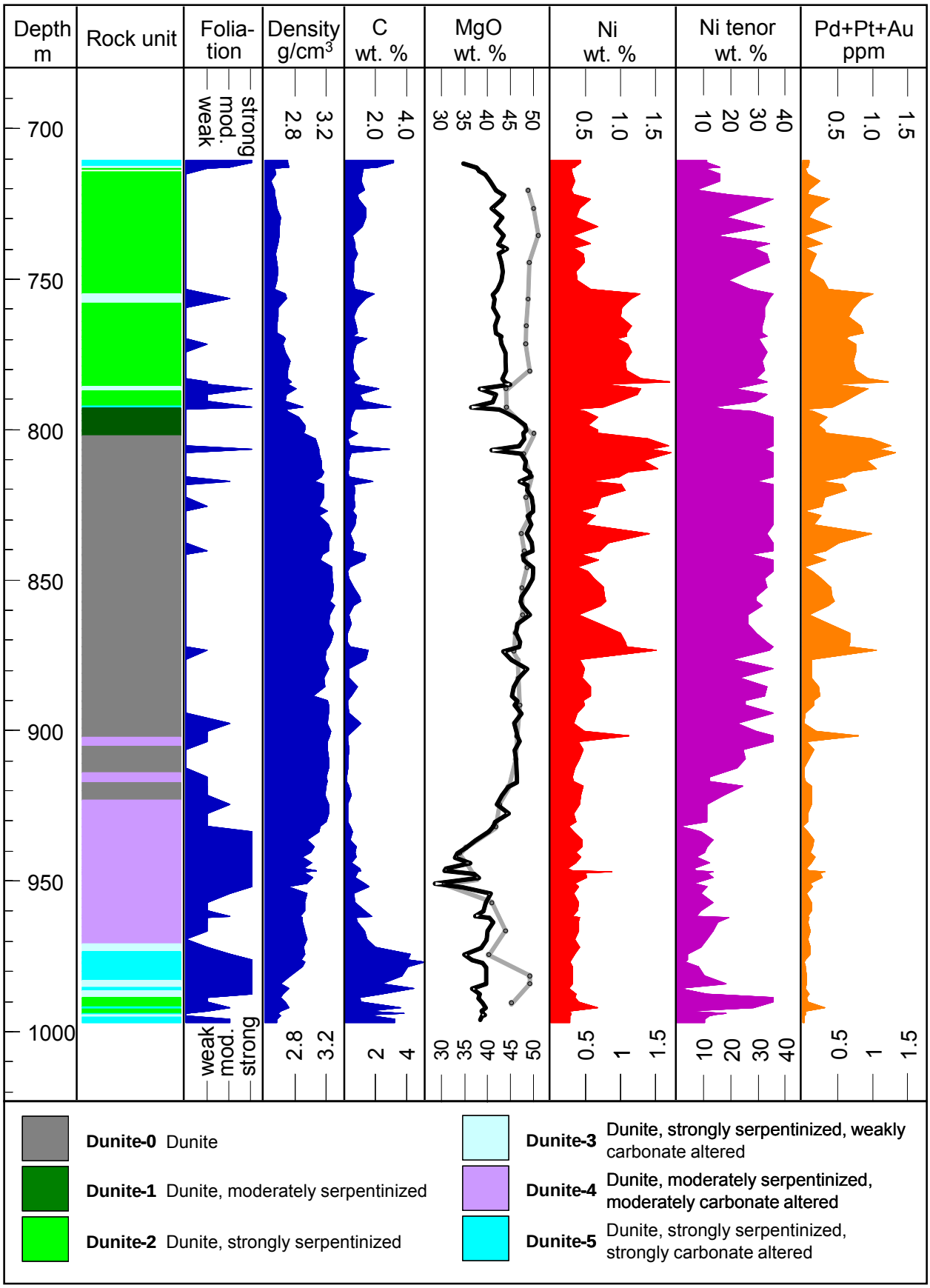
Depth m
Rock unit
Folia-tion
Density g/cm3
C wt. %
MgO wt. %
Ni wt. %
Ni tenor wt. %
Pd+Pt+Au ppm
700
750
800
850
900
950
1000
weak
mod.
strong
2.8
3.2
2.0
4.0
30
35
40
45
50
0.5
1.0
1.5
10
20
30
40
2
4
1
Dunite-0 Dunite
Dunite-1 Dunite, moderately serpentinized
Dunite-2 Dunite, strongly serpentinized
Dunite-3 Dunite, strongly serpentinized, weakly carbonate altered
Dunite-4 Dunite, moderately serpentinized, moderately carbonate altered
Dunite-5 Dunite, strongly serpentinized, strongly carbonate altered

Figure 2A Geological log of drill hole 115175 which intersects the central portion of South Manasan Intrusion, Thompson Nickel Belt. Rock type, intensity of foliation, density of drill core samples, whole-rock C, MgO (solid black line) and MgO recalculated to volatile-free basis (grey line), Ni, TPM (Pd+Pt+Au) and Ni tenor (Ni wt. % in 100% sulfide) are plotted against the depth of hole in meters. Dunite types 0-5 are explained in the text and Table 2. There is coincidence of carbonate altered rock units (dunite-3, 4 and 5), elevated whole-rock C content and the intensity of foliation. There is also a general coincidence of carbonate altered rock units with lower Ni tenor. The MgO profile shows a relatively uniform pattern punctuated by sharp drops corresponding to carbonate altered rock units (dunite-3, 4 and 5).

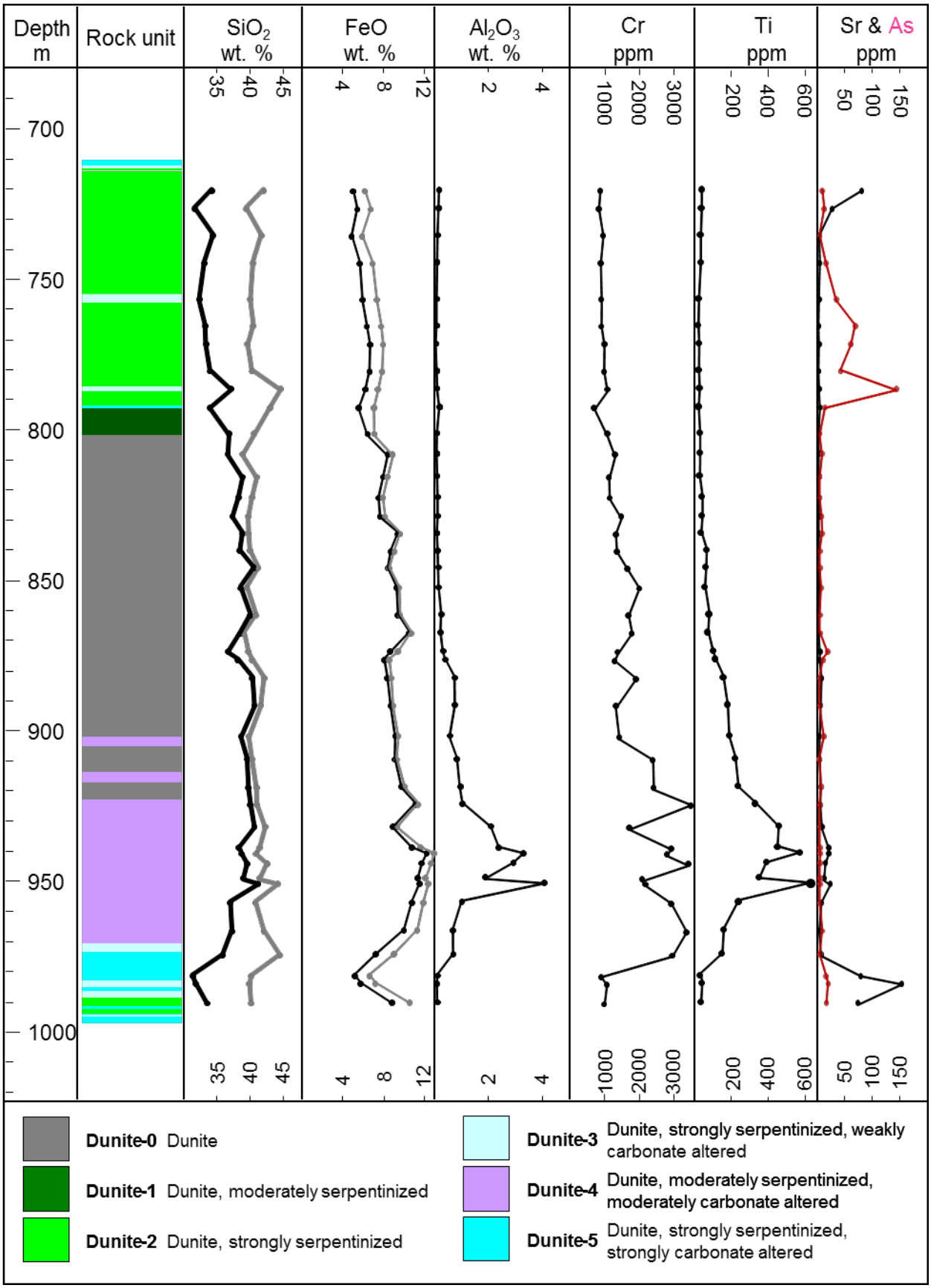
Depth
m
Rock unit
SiO2
wt. %
FeO
wt. %
Al2O3
wt. %
Cr
ppm
Ti
ppm
Sr & As
ppm
700
750
800
850
900
950
1000
35
40
45
4
8
12
2
4
1000
2000
3000
200
400
600
50
100
150
Dunite-0 Dunite
Dunite-1 Dunite, moderately serpentinized
Dunite-2 Dunite, strongly serpentinized
Dunite-3 Dunite, strongly serpentinized, weakly carbonate altered
Dunite-4 Dunite, moderately serpentinized, moderately carbonate altered
Dunite-5 Dunite, strongly serpentinized, strongly carbonate altered

Figure 2B Geological log of drill hole 115175 which intersects the central portion of South Manasan Intrusion, Thompson Nickel Belt. Rock type, whole-rock SiO_2 (black line) and in the same column SiO_2 recalculated to volatile-free basis (grey line), whole-rock FeO and in the same column FeO recalculated to volatile-free basis (grey line), Al_2O_3, Cr, V, Ti, Sr (black line) and in the same As (red line) are plotted against the depth of hole in meters. Dunite types 0-5 are explained in the text and Table 2. There are elevated values of SiO_2, FeO, Al_2O_3, Cr, V and Ti in the lower part of intrusion; this may correspond to intercumulus melt in dunite-4. Note the elevated values of Sr on the upper and lower contacts of the sill; there is also a small but noticeable enrichment of Sr in the dunite-4.

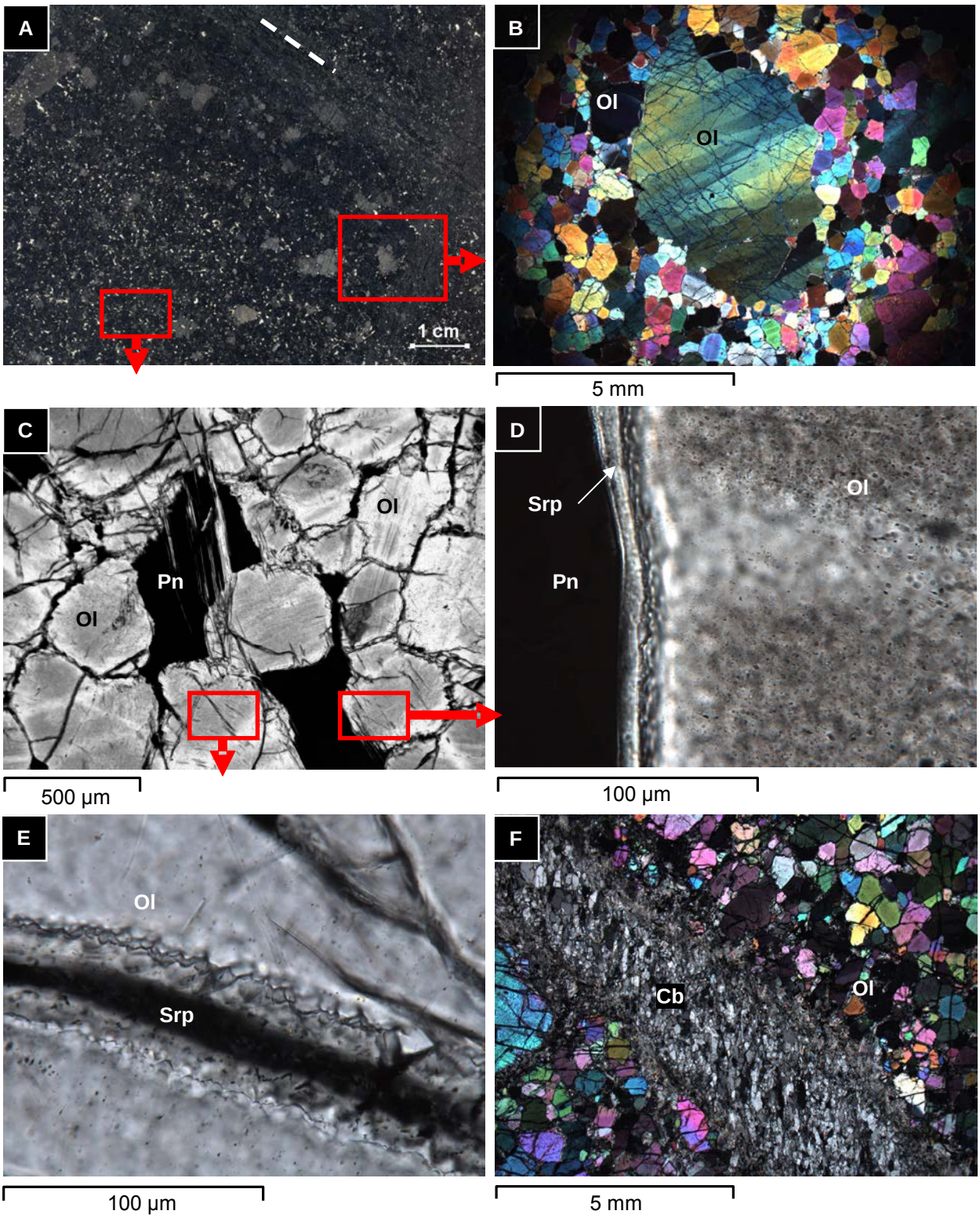

Figure 3 Photomicrographs of the silicate mineralogy of the fresh dunite (dunite-0) from the central part of the South Manasan intrusion. List of abbreviations: Cb – carbonate mineral, Ol – olivine, Pn – pentlandite, Srp – serpentine. A) Dunite-0 in hand specimen showing the development of adcumulate olivine texture, olivine megacrysts and thin veins of magnesite (direction showed with dashed line, details in Figure 3F). B) Photomicrograph of a representative sample of dunite-0 in cross-polarized light showing adcumulate texture of

olivine and the development of a twinned olivine megacryst. C) Photomicrograph of a dunite-0 in transmitted light showing adcumulate olivine texture, fractured olivine crystals with aligned dusting comprised of tiny inclusions (light grey stripes) and interstitial opaque sulfides. D) Photomicrograph of olivine in transmitted light showing aligned internal crystal dusting comprised of inclusions and crystal edge punctuated by serpentine rim. The dark area is opaque pentlandite. E) Photomicrograph of a fracture in an olivine crystal in transmitted light showing a serrated crystal edge punctuated by serpentine. F) Photomicrograph of a magnesite vein in dunite-0 in cross-polarized light showing the crosscutting relationship between the carbonate vein and adcumulate olivine.

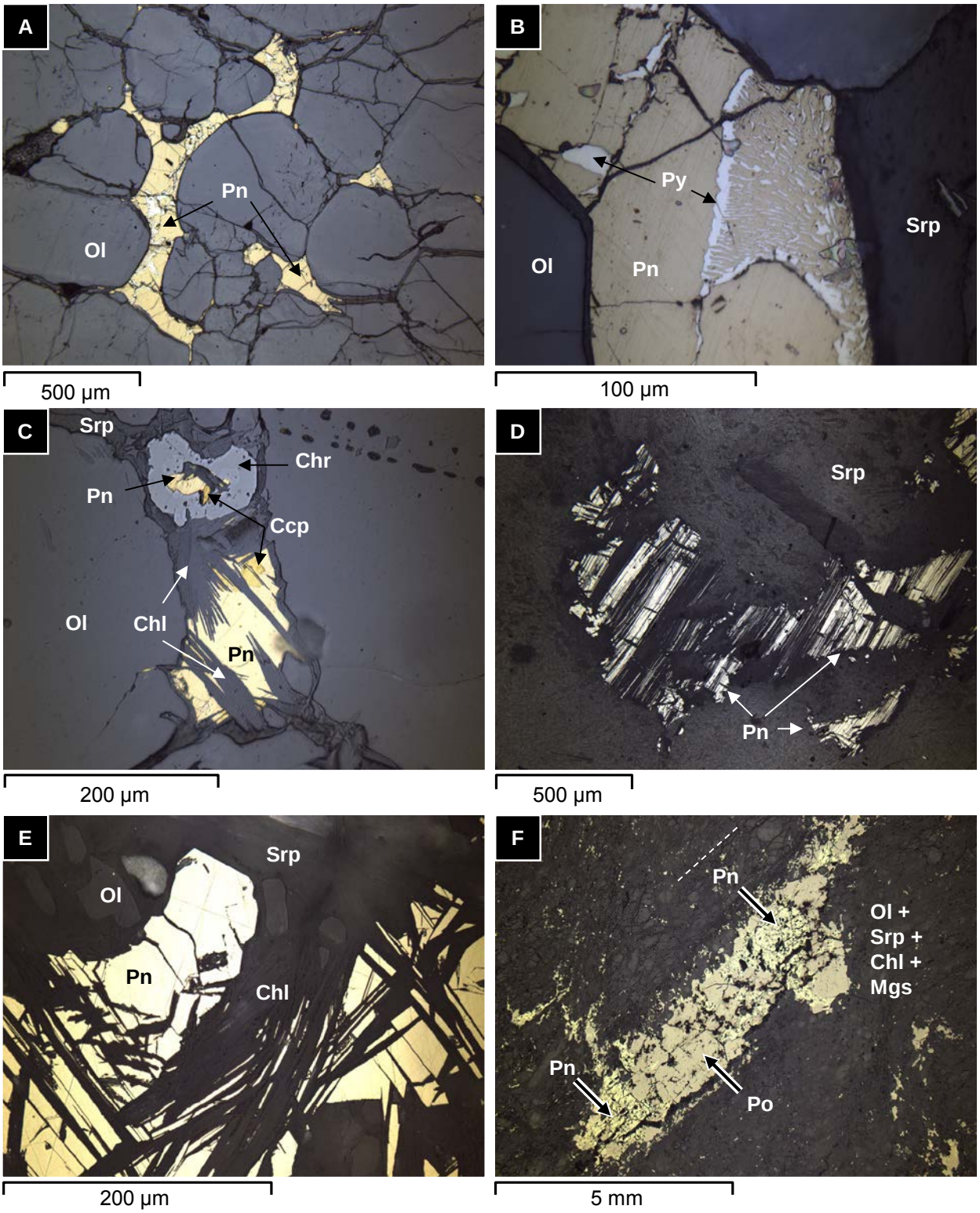

Figure 4. Photomicrographs showing the details of the sulfide mineralogy of the dunitic rocks in the South Manasan intrusion. List of abbreviations: Chl – chlorite, Chr – chrome spinel, Ccp – chalcopyrite, Mgs – magnesite, Ol – olivine, Pn – pentlandite, Py – pyrite, Srp – serpentine. A) Photomicrograph of fresh dunite-0 in reflected light showing the development of pentlandite with minor symplectic pyrite intergrowths; both sulfides display a characteristic interstitial magmatic relationship with the fresh olivine. B) Photomicrograph of fresh dunite-0 in

reflected light showing the interstitial sulfide grain comprising pentlandite and pyrite displaying symplectic intergrowth. C) Photomicrographs of weakly serpentinized dunite-1 showing interstitial pentlandite, Cr-spinel and chlorite grains. Note a small bleb of sulfide within the Cr-spinel grain consisting of pentlandite and pyrite. Also note the radiating character of chlorite crystals forming around Cr-spinel grain and the resulting sulfide-chlorite intergrowth. D) Photomicrograph of strongly serpentinized dunite-2 showing pentlandite-gangue intergrowth. Gangue minerals are: serpentine, chlorite, brucite and iowaite. Note the remnant interstitial outline of the original pentlandite crystal. E) Photomicrograph of serpentine and carbonate altered dunite-3 showing pentlandite-gangue intergrowth and the deformation of the formerly interstitial sulfide grain. F) Photomicrograph of serpentine and carbonate altered dunite-4 showing sulfide stringer consisting of pyrrhotite with pentlandite eyes. Note metamorphic foliation denoted by the dashed line.

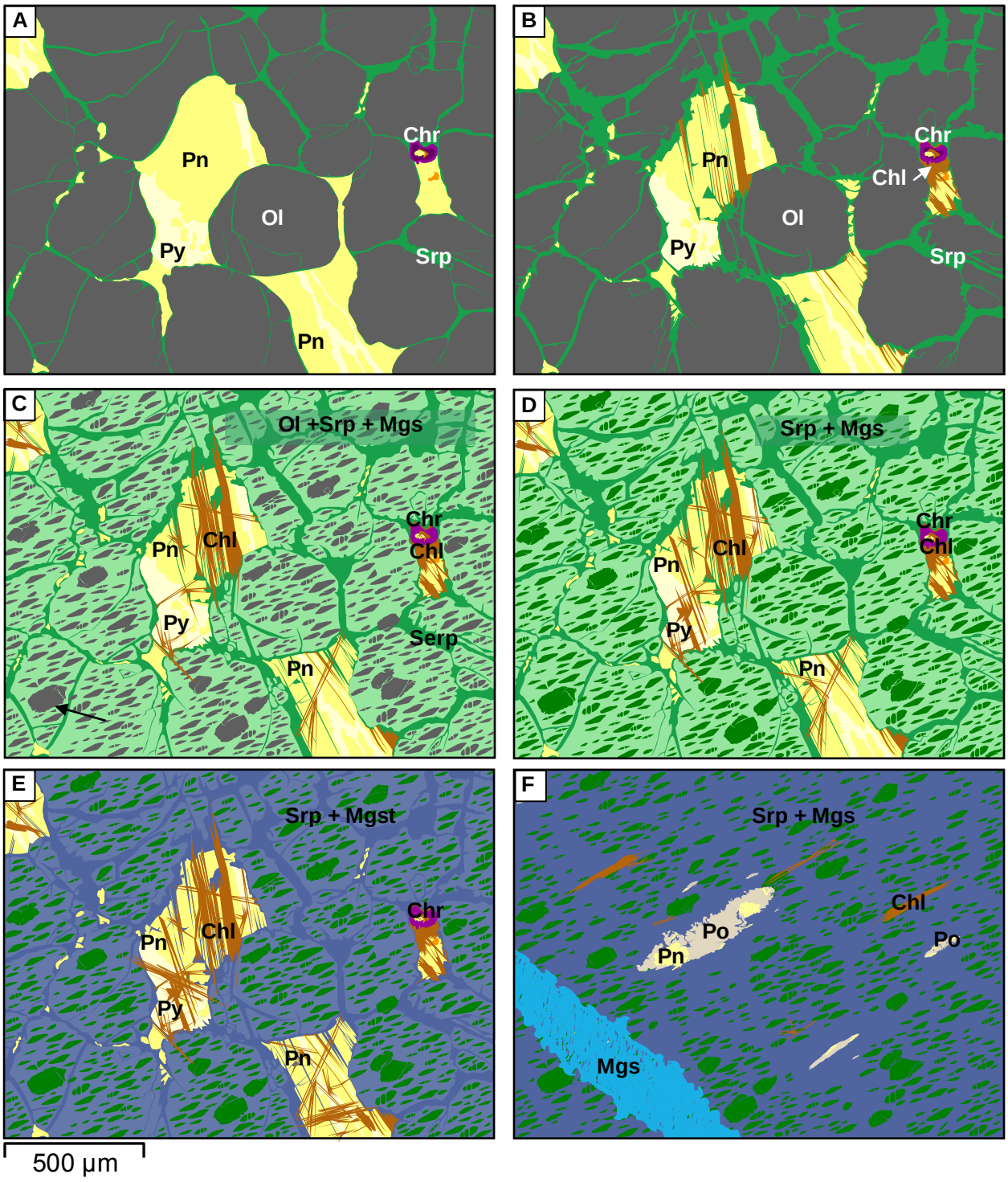

Figure 5 A series of diagrams showing the sequence of development of the different textures and mineral parageneses in the South Manasan intrusion. List of abbreviations: Chl – chlorite, Chr – chrome spinel, Mgs – magnesite, Ol – olivine, Pn – pentlandite, Py – pyrite, Srp – serpentine. A) The freshest rocks comprise dunite (dunite-0) where adcumulate olivine and interstitial sulfide grains are developed; the sulfide consists of pentlandite with pyrite intergrowths. Note the presence of interstitial Cr-spinel in contact with the pentlandite. B) Weakly serpentinized dunite (dunite-1) comprises adcumulate olivines rimmed by serpentine. Note the development of chlorite platelets in sulfide locally spatially associated with Cr-spinel. The detail of the transformation of Cr-spinel

to chlorite in provided in Figure 11. C) Serpentinized dunite (dunite-2) comprises remnant cumulate texture. Note that olivine cores are retained in what previously were fractured olivine crystals. Also note the increase in intensity of chlorite-sulfide intergrowth. D) Strongly serpentinized dunite with weak interstitial carbonate alteration (dunite-3) comprises remnant cumulate texture. Note that olivine cores are now serpentine altered. Note the progressive development of the platy pentlandite morphology. E) Serpentine and carbonate altered dunite (dunite-4) displaying remnant cumulate texture. Note that the texture of the rock is essentially the same; however, the interstitial to olivine pseudomorphs space is occupied by carbonate alteration minerals – mainly magnesite. F) Foliated strongly carbonate altered serpentinite (dunite-5). Note that within this lithology stringers of sulfide comprising pyrrhotite and pentlandite are common. The schematic transformation of sulfide grains in shown in Figure 12A.

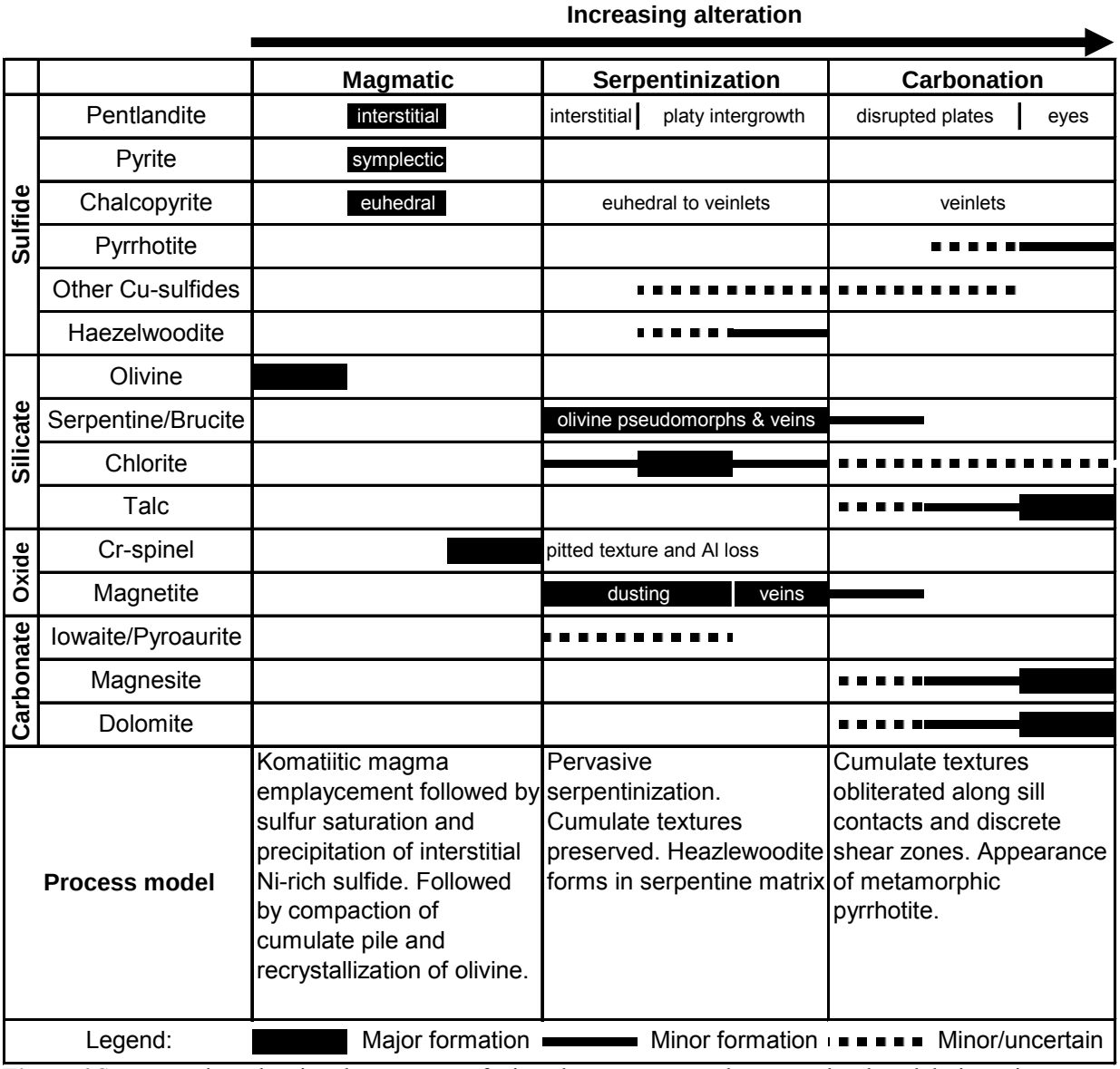

Figure 6 Summary chart showing the sequence of mineral parageneses and textures developed during primary magmatic, serpentinization, and carbonate alteration phases in the evolution of the SMI. Each stage is sub-divided into an "early", "middle" and "late" sub-stage proceeding from left to right. During the magmatic stage the first mineral to crystallize is olivine, followed by interstitial sulfides. The last mineral to crystallize during the magmatic stage is the interstitial Cr-spinel that occasionally hosts trapped sulfide grains. The serpentine alteration stage begins with alteration of olivine along grain boundaries and cracks to serpentine, brucite and fine dusting of magnetite. Within this early serpentine, zones/veinlets of iowaite appear. As the serpentinization of olivine progresses, interstitial Cr-spinel grains develop haloes of radiating chlorite platelets that penetrate interstitial sulfide grains. The serpentinization stage is culminated with complete serpentinization of olivine, development of magnetite veinlets and micron-scale grains of heazlewoodite in the serpentine matrix. The early carbonate alteration stage overlaps with late serpentine alteration stage; therefore the timing of some minerals is less certain. The latest and most abundant carbonate alteration mineral is magnesite with lesser dolomite and talc. These minerals typically crosscut the earlier adcumulate texture or remnant cumulate texture. Of special importance is the modification of sulfide assemblage to stringy pyrrhotite with subordinate amounts of pentlandite and the absence of pyrite. Other notable changes include the modification of chalcopyrite stringers to micron-scale Cu-sulfide and silicate intergrowths like chalcopyrite and cubanite with pyroaurite/iowaite and serpentine.

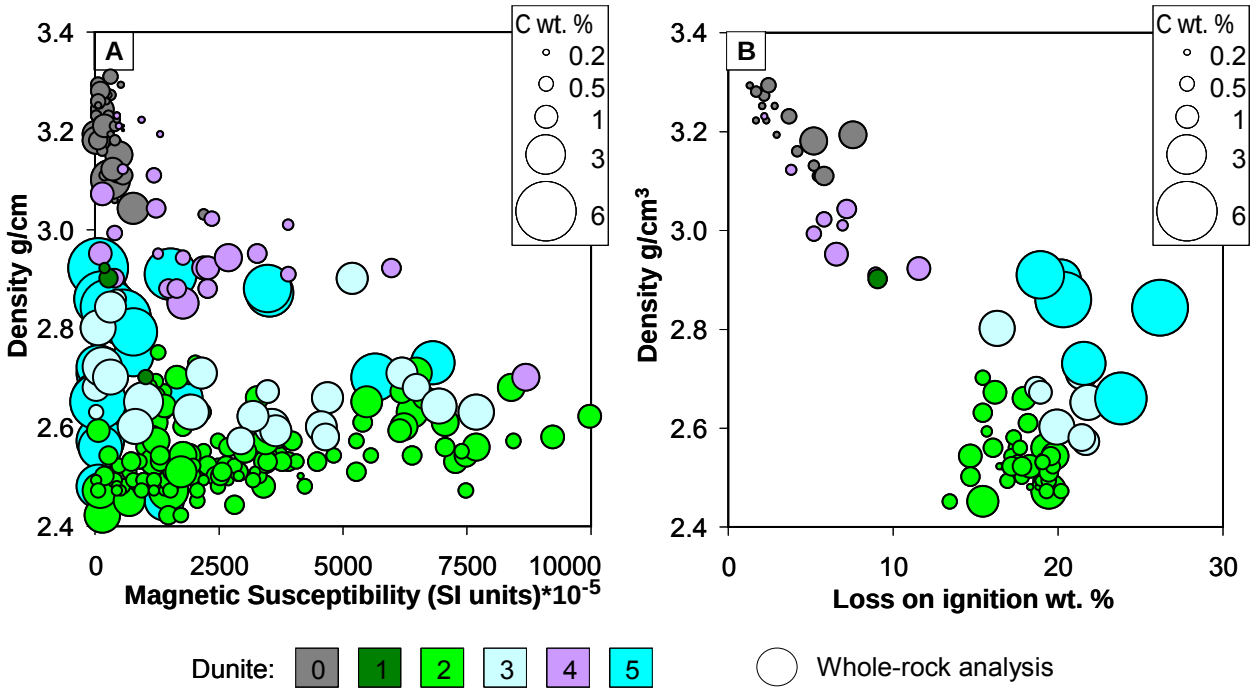

Figure 7 Physical properties of rock samples from the South Manasan intrusion. A) Magnetic susceptibility versus density with symbols sized to C wt. %. In more serpentinised rocks, there is a decrease in density and a small increase in magnetic susceptibility (dunite-0 and 1). With the development of pervasive serpentine alteration (dunite-2) a wide range of magnetic susceptibility is developed, which reflects the increase in mode % magnetite. The onset of carbonate alteration drives the density towards higher values as the magnetic susceptibility decreases. B) Loss on ignition versus whole-rock density with symbols sized to C wt. %. The rocks in the upper left corner are the freshest. As the serpentine alteration develops there is a simultaneous decrease in density and a corresponding increase in LOI content. As carbonate alteration develops there is a further increase in LOI content with a corresponding increase in density and an increase in C content.

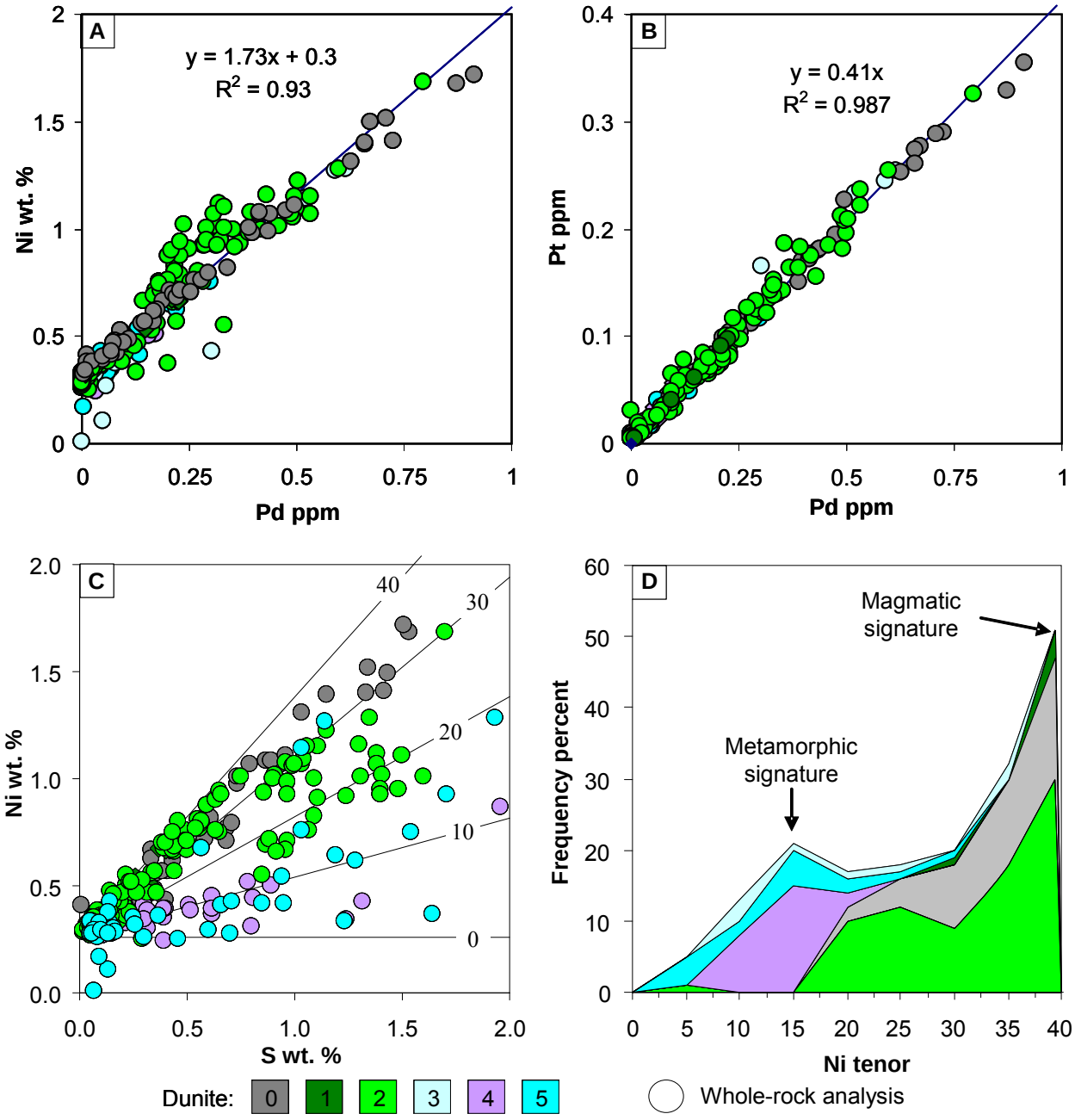

Figure 8 Whole-rock geochemistry of the South Manasan intrusion. A) Pd versus Ni concentrations in whole-rock with a trendline for all plotted sample. There is strong linear correlation between Pd and Ni (R^2=0.93). The intercept of the trendline at 0.3 wt. % corresponds well with direct measurements of Ni content in olivine and serpentine in Figure 9A. Note the Ni enrichment at around 1 wt. % Ni in dunite-2 samples; this may be due the contribution of 0.1 mode % heazlewoodite observed only in this rock type (Table 2). B) Pd versus Pt concentrations in whole rock. There is a very strong linear correlation irrespective of the rock type (R^2=0.99). C) S versus Ni concentrations in whole rock showing different populations of Ni tenor. Solid lines marked with 0, 10, 20 30 and 40 correspond to lines of constant Ni tenor. Fresh (dunite-0) and some serpentinized dunite samples (dunite-1 and 2) occupy the space between tenor lines of 40 to 30. Some of the serpentinized and carbonate altered dunites (dunite-3 and 4) occupy the space between tenor lines of 30 to 15. Carbonate altered dunite samples (dunite-4 and 5) occupy the space between tenor lines of 15 to 5. The intercept of the constant tenor lines has been set at 0.25 Ni wt. %, which was obtained by direct measurements of Ni in silicate minerals (Fig 9A). D) Tenor histogram diagram colour coded by rock type

showing a bimodal distribution. Sulfides with a Ni tenor of 30 to 39 occur in fresh and serpentinized dunites (dunite-0, 1, and 2) and sulfides with a Ni tenor of 5 to 20 occur in carbonate altered dunites (dunite-3, 4 and 5).

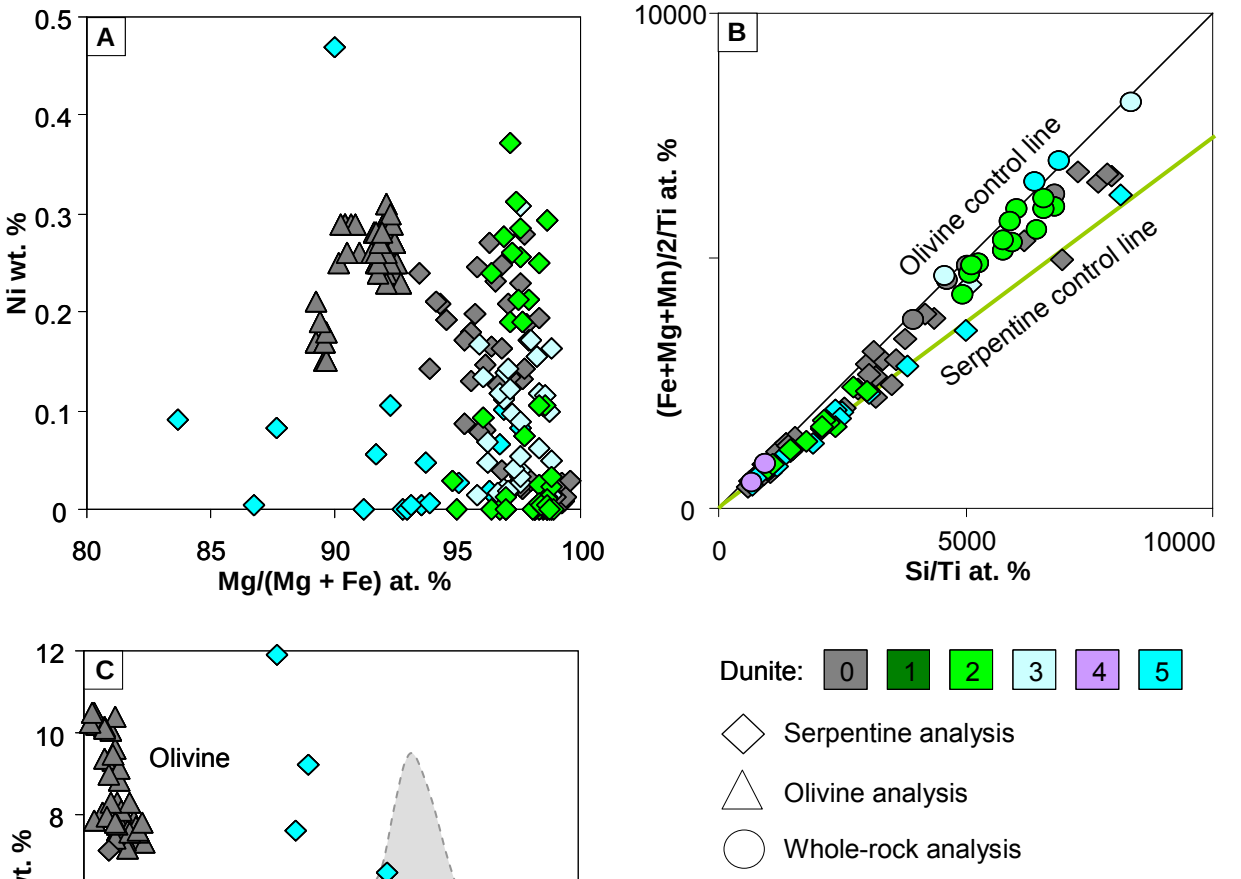

Figure 9 Silicate mineral chemistry of the South Manasan intrusion. A) Mg# (Mg/(Mg + Fe)) at. % versus Ni wt. % showing the range of Ni content in both olivine and serpentine. Olivine has a bimodal distribution of Ni content and serpentine has a broad range of Ni content that is not enriched in Ni compared to olivine. Note that serpentine samples are on average more Mg rich than olivine, except when they come from carbonate altered dunite-5. B) Pearce elements diagram with both whole-rock and serpentine analysis. Also included are the theoretical olivine control line and serpentine control line. Most whole-rock analysis plot on the olivine control line or just below it, indicating that the alteration of dunite was mostly and isochemical process. C) SiO_2 versus FeO diagram with olivine and serpentine mineral analysis. Note the most serpentine analysis plot on a tight array extending from the olivine field. Most of the serpentine analysis from carbonate altered rock units (dunite-3 and 5) plot above the serpentinization array indicating an enrichment in FeO. The grey area in the background denotes the field of compositional range of the serpentine analysis from the rest of TNB (Burnham et al., 2009).

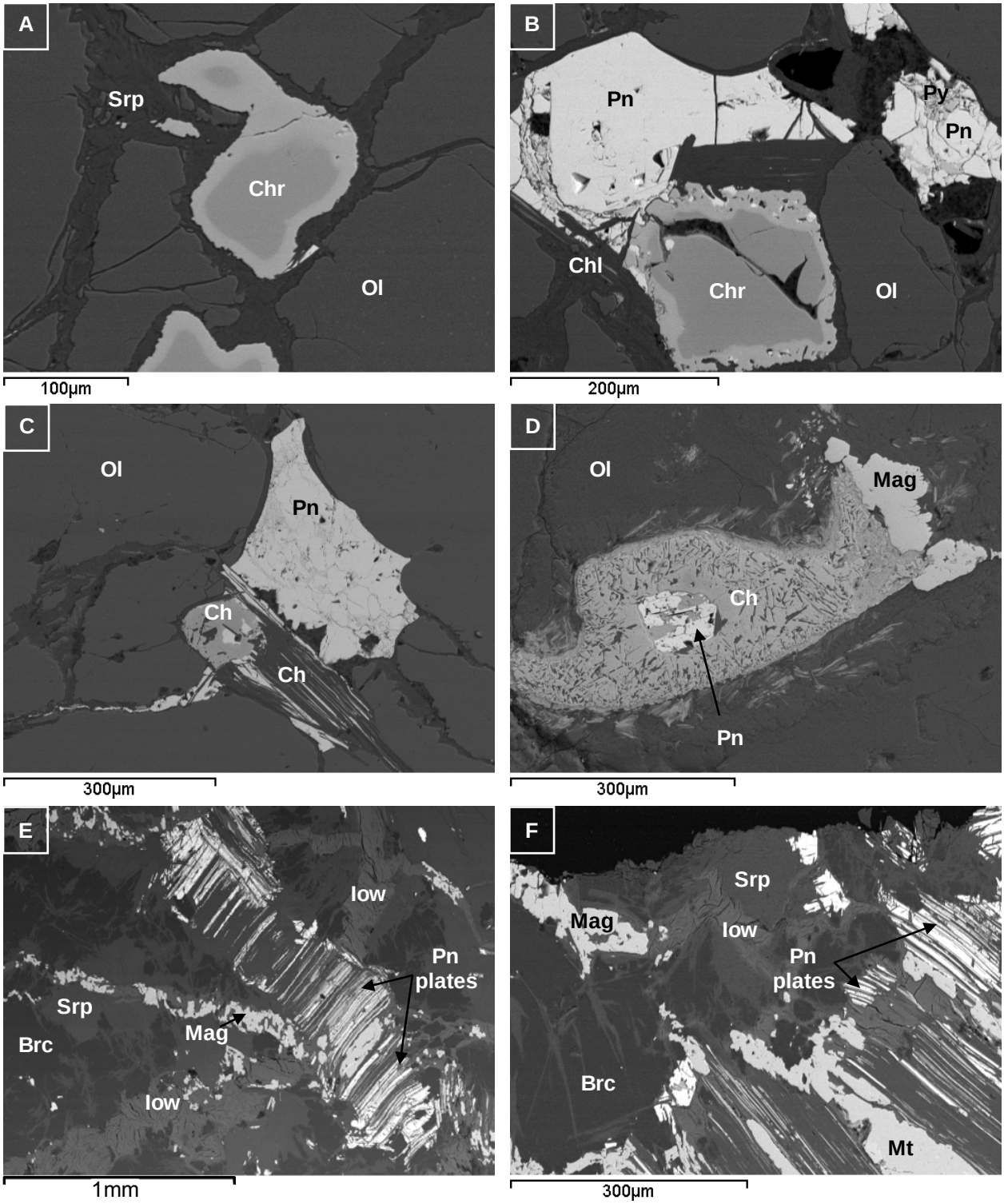

Figure 10 Backscatter electron images of minerals from the South Manasan intrusion, Thompson Nickel Belt, Manitoba. List of abbreviations: Brc – brucite, Chl – chlorite, Chr – chrome spinel, Iow – iowaite, Mag – magnetite, Ol – olivine, Pn – pentlandite, Py – pyrite, Srp – serpentine. A) Cumulate olivine rimmed by serpentine alteration with intercumulus chrome spinel with an alteration rim. B) Cumulate olivine rimmed by serpentine alteration with intercumulus chrome spinel with a pitted alteration rim, chlorite plates, pentlandite with wormy pyrite intergrowths. C) Partially serpentinized cumulate olivine with intercumulus partially altered chrome spinel. Note the pentlandite

crystal located in the centre of chrome spinel. D) Partially serpentinized cumulate olivine with intercumulus partially altered chrome spinel and pentlandite with wormy pyrite intergrowths. Note the platy chlorite located at the edge of the chrome spinel. E) Serpentinized dunite with brucite and serpentine intergrowths crosscut by a magnetite stringer and iowaite veinlet. Note the platy character of pentlandite crystals. F) Serpentinized dunite with brucite and serpentine intergrowth crosscut by a magnetite stringer that transitions to iowaite veinlet. Note the platy character of pentlandite. Also note that magnetite stringer runs in the interplate region.

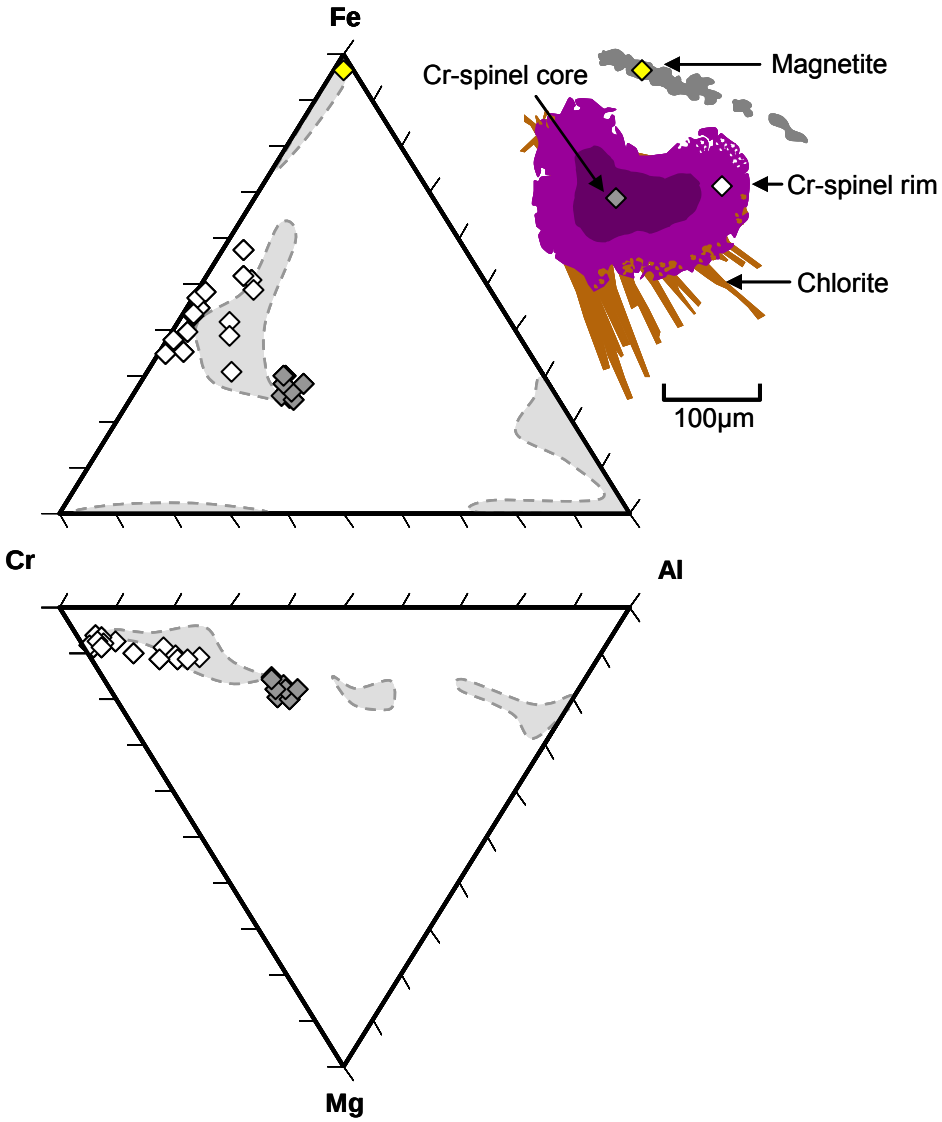

Figure 11 Ternary diagrams for Cr-spinels from the South Manasan intrusion in Fe-Cr-Al and Mg-Cr-Al space along with a schematic diagram that shows the locations of the points analysed with the SEM-EDS. Note that the Cr-spinel core is rummed with a relatively Al-poor and Fe-Cr rich spinel phase characterized by a pitted texture. The Cr-spinel is in turn associated with the development of radiating chlorite. Note the grey shaded areas on the ternary diagrams represent the range of compositions of Cr-spinels from the TNB (Burnham et al., 2009).

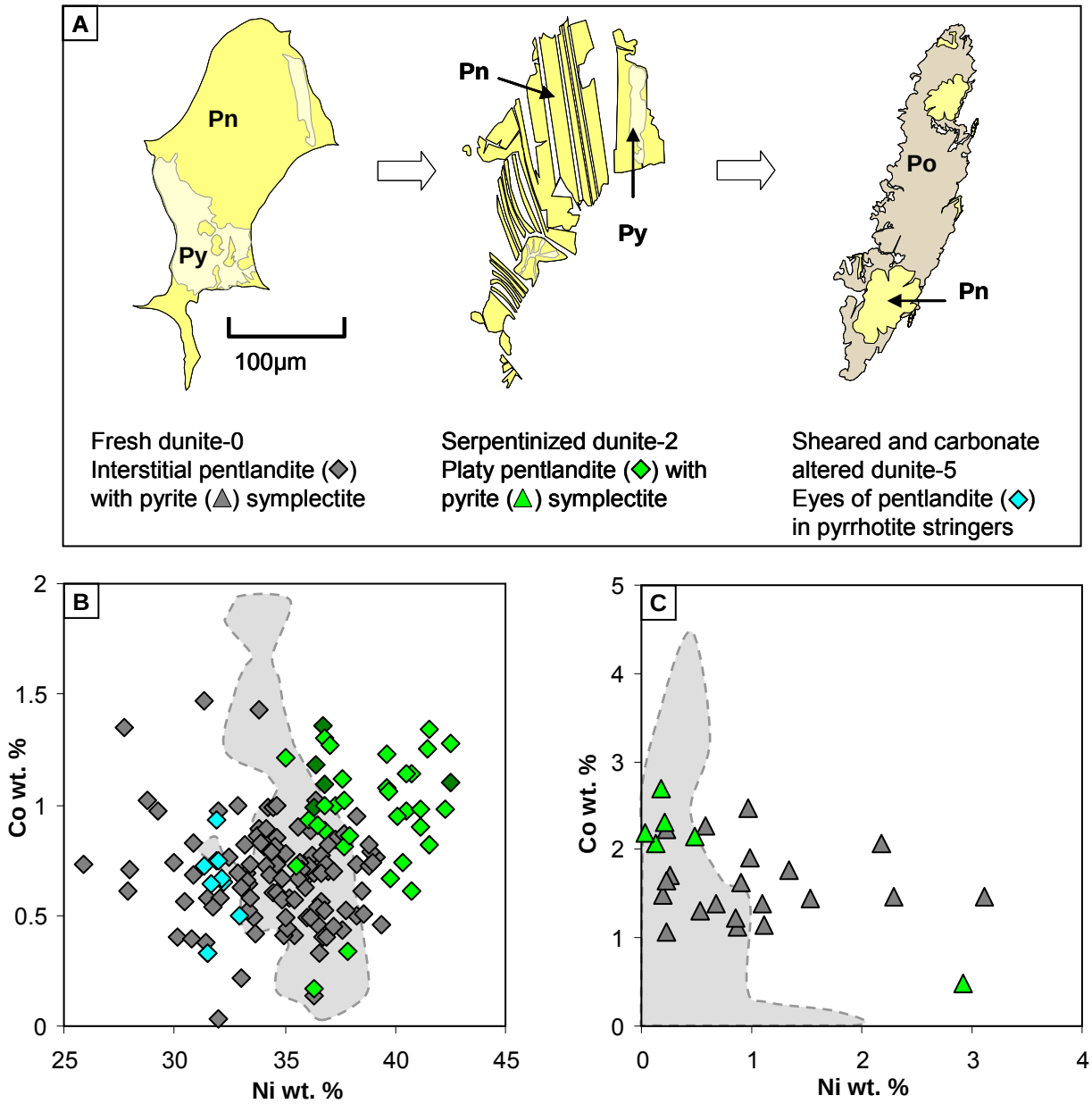

Figure 12. Schematic representation of sulfide grains and X-Y diagrams of compositional variation of pentlandite and pyrite from the South Manasan Intrusion, Thompson Nickel Belt, Manitoba. List of abbreviations: Pn – pentlandite, Po – pyrrhotite, Py – pyrite. A) The schematic representation of interstitial sulfide grains from fresh dunite (dunite-0), platy sulfides with remnant interstitial outlines from serpentinized dunite (dunite-2), and pyrrhotite stringers with pentlandite eyes from sheared and carbonate altered dunite (dunite-5). B) Ni versus Co variation of pentlandite composition colour-coded for rock type. Pentlandite displays a wide range of Ni content in fresh dunite (dunite-0), Ni-enrichment in pentlandite relative to dunite-0 in serpentinized dunite (dunite-2) and the Ni-depletion relative to dunite-0 in carbonate altered dunite (dunite-5). The grey shaded area represents the range of compositions of pentlandite from the TNB in the CAMIRO dataset. C) Ni versus Co variation of pyrite from fresh dunite (dunite-0). The grey shaded area represents the range of composition of pyrite from the TNB in the CAMIRO dataset. Note that pyrite from South Manasan is Ni-enriched relative to the rest of TNB pyrite.

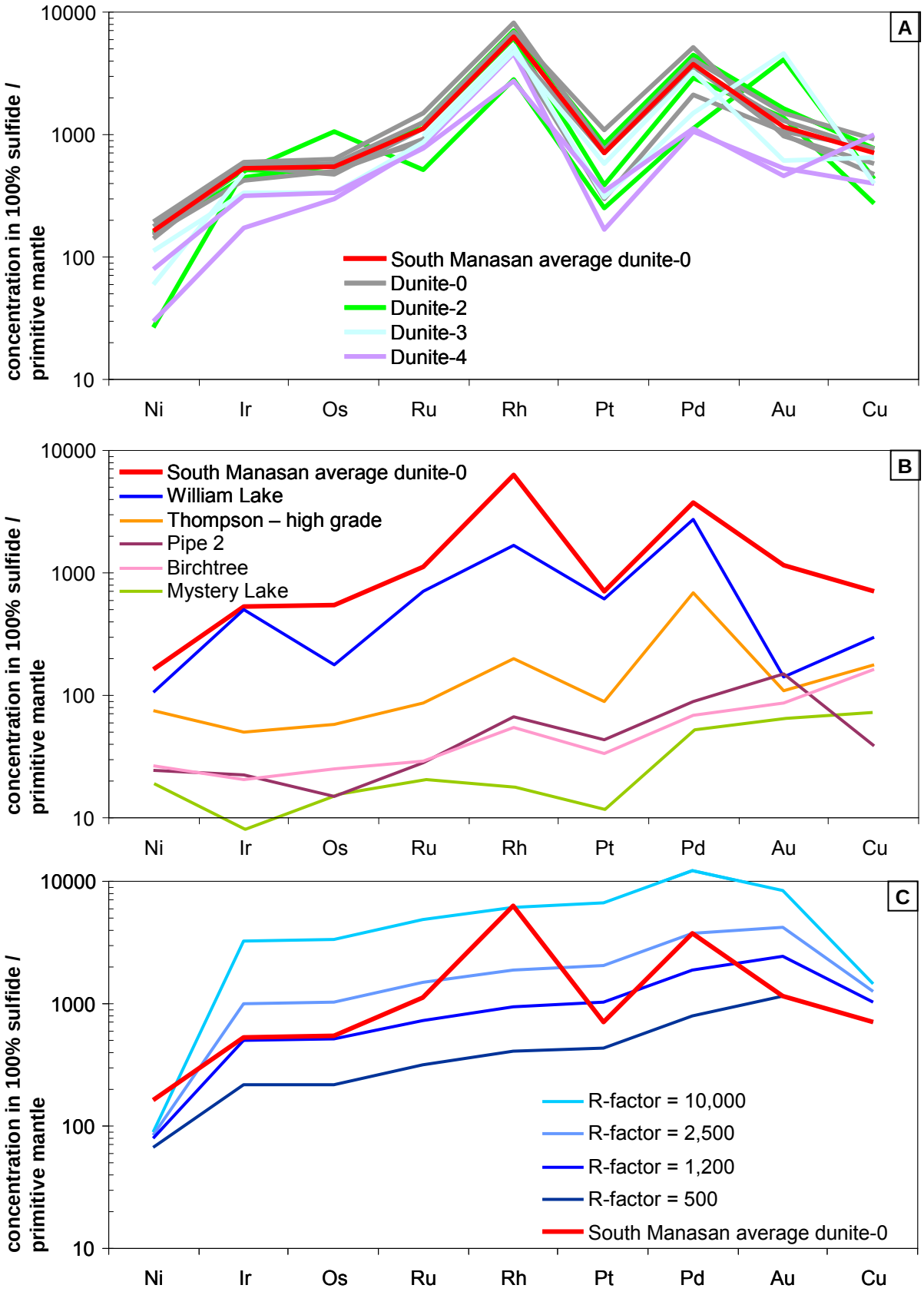
A
10000
1000
100
10
concentration in 100% sulfide / primitive mantle
South Manasan average dunite-0
Dunite-0
Dunite-2
Dunite-3
Dunite-4
Ni
Ir
Os
Ru
Rh
Pt
Pd
Au
Cu
B
South Manasan average dunite-0
William Lake
Thompson – high grade
Pipe 2
Birchtree
Mystery Lake
C
R-factor = 10,000
R-factor = 2,500
R-factor = 1,200
R-factor = 500
South Manasan average dunite-0

Figure 13 Mantle-normalized plot of Ni, PGE, Au element concentrations in 100% sulfide from South Manasan intrusion, select deposits of the Thompson Nickel Belt and model concentrations at select R-factors. Normalizing values from McDonough & Sun (1995). A) Element patterns of the South Manasan intrusion colour coded by rock type. The thick red line is an average value of freshest rocks (dunite-0). B) Element patterns of the South Manasan intrusion compared to select deposits of the Thompson Nickel Belt. TNB shows a wide range of metal enrichment with some of the lowest found in South Mystery and the highest in William Lake. Note that South Manasan has a pattern similar to the rest of TNB but with a higher degree of enrichment. C) Element patterns of the South Manasan intrusion compared to model concentrations attained at R-factors of 500, 1200, 2500 and 10000. Modelling values are reported in Table 4, after Burnham et al. (2009). Note that South Manasan intrusion element pattern cannot be modeled with one R-facor value.

Name		Dunite-0	Dunite-1	Dunite-2	Dunite-3	Dunite-4	Dunite-5	Analytical Method
Rock type / Oxide/ Element		Dunite	Dunite, moderately serpentinized	Dunite, strongly serpentinized	Dunite, strongly serp., weakly carbonate altered	Dunite, moderately serp., moderately carbonate altered	Dunite, strongly serp., strongly carbonate altered	
		n=17	n=1	n=41	n=8	n=9	n=6	
SiO_2 wt. %	average	38.76	36.80	34.06	32.93	39.04	31.42	1
	stdev	1.23		0.88	1.88	1.43	3.40	
	range	36.6-40.6		31.6-35.8	31.4-37.1	37-41.2	25.8-35.8	
TiO_2 wt. %	average	0.02	0.01	0.01	1.01	0.07	0.01	1
	stdev	0.01		0.00		0.02	0.01	
	range	0.01-0.04		0.01-0.02		0.03-0.1	0.01-0.03	
Al_2O_3 wt. %	average	0.37	0.11	0.18	0.15	2.16	0.24	1
	stdev	0.30		0.14	0.04	1.14	0.23	
	range	0.1-0.96		0.07-0.79	0.1-0.2	0.7-4.08	0.11-0.71	
MgO wt. %	average	45.54	45.50	39.33	39.19	35.57	33.53	1
	stdev	1.38		1.53	1.18	4.29	4.70	
	range	42.2-47.8		34.9-42.2	36.7-40.3	28.6-41.7	25.4-38.4	
MnO wt. %	average	0.11	0.08	0.06	0.09	0.14	0.12	1
	stdev	0.02		0.03	0.02	0.02	0.04	
	range	0.08-0.16		0.02-0.13	0.06-0.12	0.12-0.18	0.08-0.19	
FeO wt. %	average	8.18	6.00	5.72	4.99	10.21	5.02	1
	stdev	0.73		1.46	0.58	0.93	0.92	
	range	7.00-9.83		3.57-13.55	4.7-6.88	9.9-13.6	5.04-8.04	
CaO wt. %	average	0.50	0.16	0.66	0.53	1.96	3.34	1
	stdev	0.29		1.01	0.31	1.09	4.46	
	range	0.22-1.1		0.04-5.54	0.2-1.02	0.48-3.67	0.32-9.52	
Na_2O wt. %	average	0.01	0.01	0.01	0.01	0.01	0.01	1
	stdev							
	range	<0.01		0.01-0.02	0.01-0.02	0.01-0.03	<0.01	
K_2O wt. %	average	0.01	0.01	0.01	0.01	0.10	0.03	1
	stdev	0.00				0.25	0.06	
	range	0.005-0.01		<0.01	<0.01	0.01-0.77	0.01-0.15	
LOI wt. %	average	3.68	9.17	17.86	20.09	6.53	21.91	2
	stdev	1.83		1.71	1.94	2.74	2.72	
	range	1.36-7.67		13.55-20.3	16.4-21.9	2.29-11.6	18.95-26.3	
C wt. %	average	0.54	0.48	0.81	1.92	0.70	4.20	4
	stdev	0.51	0.19	0.47	0.56	0.47	0.99	
	range	0.13-2.87	0.28-0.76	0.11-2.9	0.6-2.77	0.08-1.73	2.96-6.05	
Total wt. %	average	98.98	99.18	99.16	99.08	98.17	96.78	
	stdev	1.11		1.14	1.48	1.41	3.14	
	range	97.35-100.95		97.53-101.18	97.68-101.63	96.10-100.75	91.00-100.45	

Analytical Methods:

1. Pressed pellet XRF
2. LOI at 1000°C
3. Sodium peroxide fusion ICP-AES
4. Combustion furnace
5. Four acid near total ICP-AES
6. Li metaborate fusion ICP-MS
7. Fire assay ICP-AES

REEs were below determination limits reported in appendix to thesis

Table 1A. Summary of geochemical analysis of drillcore from the South Manasan intrusion for Major oxides and C wt. %.

Name		Dunite-0	Dunite-1	Dunite-2	Dunite-3	Dunite-4	Dunite-5	Analytical Method
Rock type / Element		Dunite	Dunite, moderately serpentinized	Dunite, strongly serpentinized	Dunite, strongly serp., weakly carbonate altered	Dunite, moderately serp., moderately carbonate altered	Dunite, strongly serp., strongly carbonate altered	
		n=17	n=1	n=41	n=8	n=9	n=6	
Cr ppm	average	1572	1065	985	979	2756	1196	1
	stdev	399		93	127	643	859	
	range	1110-2400		812-1155	850-1175	1700-3490	688-2940	
Zn ppm	average	59	46	39	34	77	56	5
	stdev	17		40	9	15	25	
	range	43-122		10-271	24-51	56-94	31-101	
Pb ppm	average	2	1	4	4	8	5	5
	stdev	1		4	3	11	7	
	range	1-4		1-21	1-9	1-36	1-19	
As ppm	average	5	3	25	30	3	43	5
	stdev	4		33	47	1	76	
	range	1.9-17		2.5-191	6-144	2.5-7	2.5-198	
V ppm	average	21	6	8	8	83	11	5
	stdev	11		3	3	37	11	
	range	6-40		2.5-18	6-12.6	32-141	6-32	
Sr ppm	average	2	1	11	26	11	49	6
	stdev	2		20	53	7	52	
	range	0.7-6.2		0.3-79.4	1.1-153.4	1.9-21.9	1.2-115.5	

Analytical Methods:

1. Pressed pellet XRF
2. LOI at 1000°C
3. Sodium peroxide fusion ICP-AES
4. Combustion furnace
5. Four acid near total ICP-AES
6. Li metaborate fusion ICP-MS
7. Fire assay ICP-AES

Table 1B. Summary of geochemical analysis of drillcore from the South Manasan intrusion for trace elements: Cr, Zn, Pb, As, V and Sr.

Name		Dunite-0	Dunite-1	Dunite-2	Dunite-3	Dunite-4	Dunite-5	Analytic range & method	
Rock type / Element		Dunite	Dunite, moderately serp.	Dunite, strongly serp.	Dunite, strongly serp., weakly carb.	Dunite, moderately serp., moderately carb.	Dunite, strongly serp., strongly carb.		
		n=50	n=6	n=141	n=24	n=28	n=23		
S wt. %	average	0.59	0.32	0.46	0.39	0.55	0.63		3
	stdev	0.41	0.10	0.45	0.53	0.41	0.52		
	range	0.01-1.53	0.15-0.42	0.02-1.7	0.05-1.93	0.11-1.96	0.06-1.71		
Ni wt. %	average	0.775	0.560	0.595	0.413	0.388	0.425	0.005-35	3
	stdev	0.387	0.137	0.306	0.329	0.113	0.205		
	range	0.323-1.715	0.325-0.671	0.254-1.685	0.007-1.28	0.242-0.865	0.17-0.927		
Cu wt. %	average	0.037	0.016	0.023	0.017	0.026	0.029	0.005-35	3
	stdev	0.032	0.008	0.027	0.021	0.036	0.034		
	range	0.005-0.17	0.005-0.027	0.005-0.14	0.005-0.091	0.005-0.202	0.005-0.11		
Co wt. %	average	0.015	0.011	0.009	0.010	0.014	0.013	0.002-35	3
	stdev	0.003	0.002	0.004	0.005	0.002	0.011		
	range	0.01-0.022	0.008-0.013	0.002-0.024	0.002-0.018	0.011-0.022	0.002-0.061		
Pt ppb	average	114	65	67	47	32	37	5-10,000	7
	stdev	96	37	66	83	19	39		
	range	5-355	5-97	5-325	5-254	5-80	5-122		
Pd ppb	average	275	152	157	103	65	85	1-10,000	7
	stdev	244	86	160	193	48	102		
	range	5-913	10-225	1-794	1-615	1-212	1-310		
Au ppb	average	24	11	27	23	9	14	1-10,000	7
	stdev	19	4	25	32	4	10		
	range	1-89	4-15	1-137	1-149	2-20	2-49		
		n=5	n=0	n=3	n=2	n=2	n=0		
Os ppb	average	36		24	28	13		10-10,000	7
	stdev	29		17	36	6			
	range	9-83		14-44	2-53	9-17			
Ir ppb	average	33		20	28	9		1-10,000	7
	stdev	25		21	31	1			
	range	8.3-74		6.3-43.8	6.5-50.1	8-9.3			
Ru ppb	average	112		73	110	55		50-10,000	7
	stdev	90		85	127	21			
	range	20-260		10-170	20-200	40-70			
Rh ppb	average	30		17	27	8		5-10,000	7
	stdev	28		22	34	2			
	range	4.1-77.3		1-42.7	2.5-50.5	6.3-8.9			
Re ppb	average	5		5	5	5		5-10,000	7
	stdev	0							
	range	5-6							

Analytical Methods:

1. Pressed pellet XRF
2. LOI at 1000°C
3. Sodium peroxide fusion ICP-AES
4. Combustion furnace
5. Four acid near total ICP-AES
6. Li metaborate fusion ICP-MS
7. Fire assay ICP-AES

Table 1C. Summary of geochemical analysis of drillcore from the South Manasan intrusion for S, Ni, Cu, Co and PGE .

	Mineral	Units	Dunite-0	Dunite-1	Dunite-2	Dunite-3	Dunite-4	Dunite-5
Sulfide	Pentlandite	modal %	3	2	2.5	3	1	3.5
	Pyrite	modal %	0.25	0.2	0.2	0.25	0.15	0.25
	Chalcopyrite	modal %	0.1	0.05	0.05	0.05	0.05	0.1
	Pyrrhotite	modal %					0.1	0.5
	Other Cu-sulfides	modal %		0.05	0.2	0.01	0.05	0.5
	Heazlewoodite	modal %			0.1			
Silicate	Olivine	modal %	90	50	10		45	
	Serpentine/Brucite	modal %	5	46	79	74	41	47
	Chlorite	modal %	0.75	0.2	0.2	0.2	3	0.25
	Talc	modal %	0.1	0.1	0.5	1	0.5	5
Oxide	Cr-spinel	modal %	0.5	0.5	0.3	0.25	0.25	0.25
	Magnetite	modal %		0.1	2.5	3	1.5	0.5
Carbonate	Magnesite	modal %		0.1	1	15	5	30
	Dolomite	modal %		0.1	0.75	1	1	12
	Iowaite	modal %		0.1	2.5	2	0.25	
	Pyroaurite	modal %		0.1				
Physical properties	Loss on Ignition	wt. %	3.7	9.2	17.9	20.1	6.5	21.9
	Density	g/cm^3	3.19	2.82	2.54	2.68	3	2.74
	Magnetism	unitless (SI) x 10^{-5}	325	400	2775	2950	1950	1200
	Colour		medium grey	dark grey to dark green	black to light green	grey to green	dark grey	medium grey
	Texture		cumulate	remnant cumulate	remnant cumulate	remnant cumulate	foliated/ remnant cumulate	foliated
Economic parameters	Ni grade	wt. %	0.78 (0.32-1.71)	0.56 (0.33-0.67)	0.60 (0.25-1.69)	0.41 (0.01-1.28)	0.39 (0.24-0.87)	0.43 (0.17-0.93)
	Ni tenor	wt% in 100% sulfide	34	36	28	15	9	10
	Ni % of Pentlandite	wt. %	34.6	36.7	38.9	-	-	31.8
	TPM (Pt+Pd+Au) grade	ppm	0.30 (0.02-1.32)	0.23 (0.02-0.34)	0.25 (0.01-1.22)	0.17 (0.01-0.99)	0.11 (0.01-0.31)	0.14 (0.01-0.45)
	TPM tenor	ppm in 100% sulfide	27	28	21	17	8	8
	Gangue intergrowth		Trace	Weak	Moderate	Moderate	Strong	Weak

Table 2. Summary of mineralogy, physical properties and economic factors of the South Manasan intrusion. Numbers in brackets represent the range of values.

A	Sulfide minerals: scanning electron microscope energy dispersive spectroscopy (SEM-EDS) analysis														
	Pentlandite, n=164			**Pyrite**, n=27			**Chalcopyrite**, n=9			**Heazlewoodite**, n=28			**Pyrrhotite**, n=3		
wt. %	average	stdev	range	average	stdev	range	average	stdev	range	average	stdev	range	average	stdev	range
S	35.65	1.05	30.8-41.02	55.14	1.08	50.29-55.98	37.65	0.39	37.16-38.36	29.57	1.15	28.25-32.89	38.69	0.08	38.6-38.76
Fe	27.99	3.22	20.5-37.07	41.96	0.75	39.48-43.38	29.53	0.24	29.09-29.84	0.22	0.46	0-1.42	60.59	0.33	60.32-60.95
Co	0.86	0.64	0.03-5.58	1.67	0.52	0.49-2.7							0.44	0.16	0.28-0.6
Ni	35.50	3.33	25.91-42.52	1.23	1.79	0.04-9.17				70.18	1.02	67.11-71.75	0.28	0.25	0-0.48
Cu							32.82	0.38	32.2-33.53						
Total	100.00			100.00			100.00			99.97			100.00		

B	Silicate minerals: wavelenght dispersive spectroscopy electron microprobe analysis											
	Olivine, n=49			**Serpentine**, n=121			**Chlorite**, n=25			**Talc**, n=14		
wt. %	average	stdev	range	average	stdev	range	average	stdev	range	average	stdev	range
SiO_2	40.81	0.32	40.17-41.48	41.65	1.68	36.14-45.07	33.08	1.18	32.11-37.63	61.16	1.86	57.27-62.76
Al_2O_3				0.18	0.35	0-2.21	14.38	1.16	11.94-16	0.21	0.54	0-2.07
MgO	50.43	0.76	48.81-51.48	42.67	1.45	38.5-44.51	34.94	0.83	33.97-36.81	31.43	1.03	29.89-33.61
FeO	8.48	1.04	7.18-10.49	2.22	1.31	0.34-7.61	4.25	1.24	2.1-6.12	1.93	0.49	1.29-2.99
MnO	0.14	0.04	0.06-0.25	0.05	0.05	0-0.27	0.02	0.02	0-0.09	0.03	0.03	0-0.07
Cr_2O_3				0.06	0.14	0-0.81	1.33	0.97	0.35-4.05	0.06	0.11	0-0.42
TiO_2				0.01	0.02	0-0.07	0.04	0.02	0-0.1	0.02	0.02	0-0.05
Na_2O				0.01	0.01	0-0.07	0.01	0.02	0-0.05	0.03	0.03	0-0.1
CaO	0.08	0.08	0-0.32	0.02	0.02	0-0.07	0.04	0.03	0-0.12	0.04	0.03	0.01-0.11
NiO	0.32	0.05	0.19-0.39	0.13	0.14	0-0.65	0.10	0.04	0.03-0.19	0.11	0.04	0.05-0.18
H_2O				12.80	0.22	12.19-13.25	12.77	0.14	12.6-13.37	4.69	0.18	4.3-4.9
Total	100.25	0.33	99.62-100.87	99.81	1.16	97.53-102.63	100.96	0.90	99.64-104.63	99.70	1.14	97.27-101.09

C	Silicate and oxide minerals: SEM-EDS analysis											
	Brucite, n=29			**Iowaite**, n=15			**Cr-spinel**, n=8			**Cr-spinel rim**, n=17		
wt. %	average	stdev	range	average	stdev	range	average	stdev	range	average	stdev	range
SiO_2				1.71	1.16	0.58-4.73						
Al_2O_3							18.08	1.41	15.79-19.84	3.30	2.87	0.51-10.18
MgO	61.05	1.32	58.29-63.95	41.29	0.91	39.22-43.05	8.29	1.20	6.55-9.93	3.34	1.79	1.84-9.8
FeO	4.81	0.78	2.35-5.94	22.31	1.41	20.25-25.11	25.82	1.83	23.32-28.56	40.30	6.59	29.29-53.78
MnO							0.96	0.12	0.85-1.17	1.16	0.21	0.92-1.67
Cr_2O_3							45.94	1.62	43.45-48.2	50.43	6.88	38.59-61.94
TiO_2							0.46	0.01	0.45-0.47	1.18	0.99	0.43-3.52
V_2O_3										0.86	0.31	0.54-1.18
H_2O	34.14*			25.40*								
Cl				9.30	0.67	8.43-10.38						
Total	100.00			100.00			99.55			100.57		

Table 3. Summary of mineral analysis from the South Manasan intrusion, Thompson Nickel Belt, Manitoba.
A) Sulfide mineral analysis by SEM-EDS.
B) Silicate mineral analysis by wavelength dispersive electron microprobe.
C) Silicate and oxide mineral analysis by SEM-EDS.

	Ni (ppm)	Cu (ppm)	Pd (ppb)	Pt (ppb)	Ir (ppb)	Rh (ppb)	Ru (ppb)	Os (ppb)	Au (ppb)	Reference
Magma used in modelling	1015	78	6.3	6.3	1.4	0.74	3.2		2.5	1
								1.5		2
Sulfide/silicate partitioning coefficient	175	600	30,000	30,000	30,000	30,000	30,000		5000	1
								30,000		3
Primitive mantle	1960	30	3.9	7.1	3.2	0.9	5	3.4	1	4

References: 1. Burnham et al., (2009). 2. Crocket (2002). 3. Fleet et al. (1999).
4. McDonough & Sun (1995)

Table 4. Summary of values used to estimate silicate:sulfide ration (R-factor) of the South Manasan intrusion. Metal concentrations in parental magma were previously used to estimate R-factor for TNB deposits by Burnham et al., (2009).

	South Manasan	Mt. Keith	Jinchuan	Santa Rita	Dumont	Betheno
Location	Thompson Nickel Belt, Manitoba, Canada	Agnew-Wiluna belt, Western Australia	Longshoushan thrust belt, Gansu, China	Itabuna-Salvador-Curaca belt, Balh, Brazil	Abitibi belt, Quebec, Canada	Agnew-Wiluna belt, Western Australia
Host rock	Dunite	Dunite, peridotite *1*	Dunite, peridotite, lherzolite, pyroxenite *5*	Dunite, websterite, gabbroic rocks *9*	Dunite, peridotite *11*	Dunite *15*
Alteration assamblage	Fresh to serpentinized; carbonate altered along structures	Talc-carbonate, serpentine, hydrotalcite *1, 2*	Variably serpentinized *5*	Absent in the ore zone *9*	Serpentinized in ore zone, talc-carbonate altered on margins *12 14*	Fresh to weakly serprentinized ore zone *15*
Origin	Undifferentiated sill	Undifferentiated sill *3*	Undifferentiated chonolith/sill *6*	Differentiated layered intrusion *9*	Cryptic layered sill *12 ,*	Undifferentiated sill *15*
Sulfide mineralogy	Pn >> Py > Ccp >> Hzl	Pn >> Po, Mlr, Vi > Py, Ccp, Hzl, Grs *1, 4*	Pn, Po, Ccp *5*	Pn >> Po, Py, Ccp *9*	Pn >> Hzl > Awr > Mlr *11*	Pn >> Py, Mlr *15*
Sulfide texture	Interstitial	Intercumulus blebs *1, 4*	Interstitial, net-texture *5*	Interstitial, stratiform layer *9*	Interstitial *11*	Interstitial *15*
Ni tenor	9-36	16 *4*	8-10 *7*	15-25 *9*	32-86** *14*	31 *15*
TPM tenor	8-28 ppm	10-30 ppb *4*	1-9 ppm *7*	0.1 - 10 ppm *9*	1-3 ppm *13*	5-6 ppm *15*
Grade and size*	0.5% Ni 1200 m x 125 m x 1000 m	506 Mt @ 0.55% Ni *4*	500 Mt @1.2% Ni 0.7% Cu *8*	570 Mt @ 0.52% Ni *10*	1,665 Mt @ 0.27 % Ni *14*	0.6% Ni 500m x 250m *15*

* There are no NI 43-101 compliant resource statements for South Manasan or Betheno available in the public domain

** Ni tenor estimated based on mill tesing composite samples and a Ni cutoff of 0.15 wt. % used in grade and tonnage asessment

List of abbreviations: Awr - awaruite, Ccp - chalcopyrite, Grs - gersdorffite, Hzl - heazlewoodite, Mlr - millerite, Pn - pentlandite, Po - pyrrhotite, Py - pyrite, Vi - violarite

References: 1. Hopf and Head (1998). 2.Grguric et al. (2001). 3. Rosengren et al. (2005). 4. Grguric et al. (2006). 5. Chai and Naldrett (1992). 6. Lehmann et al. (2007). 7. Song et al. (2009). 8. Barnes and Tang (1999). 9. Barnes et al. (2011b). 10. Inwood (2011). 11. Eckstrand (1975). 12. Duke (1986). 13. Brugmann et al. (1990). 14. Ausenco (2013). 15. Barnes et al. (2009).

Table 5 Comparison of the South Manasan intrusion to other global low grade ultramafic-hosted Ni deposits

APPENDIX A: Sample preparation, analysis, quality control and results

Samples from the South Manasan Intrusion were derived from HQ sized (63.5 mm diameter) diamond drill cores (numbers 115175, 115191 and 115194). Locations of the drill hole collars and traces are shown in Figure 1B and 1C. The core was divided into lithological intervals based on macroscopic mineralogical observations, colour and texture. All occurrences of sulfide and ultramafic rock were sampled and subjected to specific gravity and magnetic susceptibility measurements, lithogeochemical analysis, polished this section petrography, scanning electron microscope energy dispersive spectrometry (SEM-EDS) petrography and mineral chemistry and wavelength dispersive electron microprobe mineral chemistry (Table A-1).

Sample density was measured by weighing a representative piece of drill core from each sample interval using an Ohaus ExplorerPro weight scale. “Weight in air” was measured on top of the scale and “weight in water” in a water-submerged tray suspended from a weighing hook underneath the scale (Fig A-1). The density was calculated according to formula:

$$\text{Density} = \frac{\text{weight in air}}{\text{weight in air} - \text{weight in water}}.$$

The magnetic susceptibility was measured from the same piece of drill core using a Fugro GMS-2 handheld magnetic susceptibility meter and reported as SI unitless x 10^{-5}.

Lithogeochemical sampling and sample preparation

Lithogeochemical samples were taken in 3 stages. Stage 1 sampling covered the entire ultramafic intersections from each drill hole with continuous samples. Dill hole 1151750 was subdivided into 140 lithogeochemical samples, 1151910 into 59 samples and 1151940 into 76 samples. The samples were free of fault gauges, but include talc-carbonate or serpentine stringers. Heavily jointed samples and rubbly core was used where no other material was available. The minimum sample length was 15 cm (0.5 feet), maximum 3 m (10 feet) and the average sample length was 2.1 m (7 feet). The samples were then laterally halved with a core saw (Fig. A-2). These half-core splits were submitted for ore-grade assay of Ni, Cu, Co, Fe, S, Mg, Pt, Pd and Au (ALS packages ME-ICP81 and PGM-ICP23). The minimum sample weight was 0.56 kg, maximum 15.04 kg and the average sample weight was 8.26 kg. The remaining half core was laterally quartered and was used for Stage 2 and 3 samples. The relatively homogeneous sample medium and large sample weights ensured that sampling was carried out according to Gy's sampling rule.

Stage 2 comprised 73 lithogeochemical samples that were submitted for trace level multi-element whole-rock geochemistry (ALS packages ME-XRF05, ME-ICP06, ME-MS81, ME-ICP61, LOI OA-GRA05 and C C-IR07) and ore-grade assay like Stage 1. Sample intervals adhered to Stage 1 dimensions so that ore-grade results can be compared for each interval. The minimum sample weight was 0.56 kg, maximum 6.94 kg and the average sample length was 4.34 kg.

Stage 3 comprised 12 lithogeochemical samples that were submitted for ultra-trace level rare earth, trace element and platinum group element whole rock geochemistry (Actlabs packages IMC-100 and NI-FINA). The sample material was collected from the master pulps of Stage 2 samples.

Analysis

Data were reported by ALS Labs, Actlabs and Geolabs using methods with analytical ranges, LLD, and precision guides as per Data Repository 1. Stage 1 and 2 were analyzed at ALS Labs. Samples were weighed and crushed using Boyd crushers using high chrome iron plates to better that 70% passing a 2 mm. A split of up to 250 g was taken using a Boyd rotary splitter and pulverized using standard steel Essa LM2 pulverizers to better than 85% passing a 75 micron screen. The samples were subject to the following methods:

Evaluation of ores and high grade materials by Fusion-ICP-AES (ALS code ME-ICP81). A prepared sample (0.2 g) was added to sodium peroxide flux (2.6 g), mixed well and then fused in a 670°C furnace. The resulting melt was cooled and then dissolved in 30% hydrochloric acid. This solution was then analyzed by inductively coupled plasma – atomic emission spectrometry and the results were corrected for spectral inter-element interferences.

Precious metal fire assay with ICP finish (ALS code PGM-ICP23). The fire assay technique uses high temperature and flux to 'melt' the rock and allow the precious metals to be collected. 30 g of sample material was used. Lead formed from the reduction of litharge (PbO) was used as the collecting medium for silver and gold. The test sample was mixed with a high

soda ash that fused at high temperature with the gangue minerals present in the sample to produce a slag that is liquid at the fusion temperature. The flux to sample ratio of 5 – 6:1 was used. The liberated precious metals were scavenged by the molten lead and gravitated to the bottom of the fusion crucible. The prill was then dissolved in a mixture of hydrochloric and nitric acid (aqua regia) and the concentration determined by spectroscopic methods.

Major element oxides by pressed pellet XRF (ALS code ME-XRF06). A calcined or ignited sample (0.9 g) was added to 9.0g of Lithium Borate Flux (50 % - 50 % $Li_2B_4O_7$ – $LiBO_2$), mixed well and fused in an auto fluxer between 1050 - 1100°C. A flat molten glass disc was prepared from the resulting melt. This disc was then analyzed by X-ray fluorescence spectrometry.

Trace elements pressed pellet XRF (ALS code ME-ICP06). A finely ground sample powder (10 g minimum) was mixed with a few drops of liquid binder (polyvinyl alcohol) and then transferred into an aluminum cap. The sample was subsequently compressed under approximately 30 ton/in^2 in a pellet press. After pressing, the pellet was dried to remove the solvent and analyzed by WDXRF spectrometry.

Rare and trace elements lithium metaborate fusion ICP-MS (ALS code ME-MS81). A prepared sample (0.200 g) was added to lithium metaborate flux (0.90 g), mixed well and fused in a furnace at 1000°C. The resulting melt was then cooled and dissolved in 100 mL of 4% HNO_3 / 2% HCl_3 solution. This solution was then analyzed by inductively coupled plasma - mass spectrometry.

Rare earth and trace elements four acid near total ICP-AES (ALS code ME-ICP61). A prepared sample (0.25 g) was digested with perchloric, nitric, hydrofluoric and hydrochloric acids. The residue was topped up with dilute hydrochloric acid and the resulting solution was

analyzed by inductively coupled plasma-atomic emission spectrometry. Results were corrected for spectral interelement interferences.

Loss on ignition at 1000°C (ALS code LOI OA-GRA05). A prepared sample (1.0g) was placed in an oven at 1000°C for one hour, cooled and then weighed. The percent loss on ignition was calculated from the difference in weight.

Total Sulphur using a Leco sulphur analyzer (ALS code S-IR08). The sample (0.01 to 0.1 g) was heated to approximately 1350 °C in an induction furnace while passing a stream of oxygen through the sample. Sulphur dioxide released from the sample was measured by an IR detection system and the total sulphur result was provided.

Stage 3 samples were analyses at Actlabs with the following method:

Low-level precious metal nickel fire assay with INAA finish (Actlabs code NI-FINA). Samples up to 50 g in size were fire assayed using a nickel sulfide (NiS) fire assay procedure. The nickel sulphide button was dissolved in concentrated HCl and the resulting residue which contains all the PGE and Au were collected on a filter paper. This residue underwent 2 irradiations and 3 separate counts to measure all the PGE and Au. Instrumental Neutron Activation Analysis (INAA) is an analytical technique, which is dependent on measuring gamma radiation induced in the sample by irradiation with neutrons. The primary source of neutrons for irradiation is usually a nuclear reactor. Each element which is activated emits a characteristic wavelenght of gamma radiation which can be measured and quantified.

At Geolabs the pulp split has been analyzed for:

Minor and trace elements using multi-acid digestion and ICP-MS (Geolabs code IMC-100). Sample calibration was carried out using a combination of synthetic multi-element solutions and certified reference materials.

Quality control

Accuracy was measured by repeated analysis of standard reference materials and comparison of the values with expected values. Examples of this are shown in Fig A-3 where expected and observed Ni, Cu, S, Pt, Pd, Au, MgO, FeO and Cr are shown. Precision was monitored by repeated analysis of samples and standards. Figure A-3 shows the precision on reference materials achieved for observed Ni, Cu, S, Pt, Pd, Au, MgO, FeO and Cr, and demonstrates that precision is within the range of uncertainty, except for Cr.

Quality control samples were different for Stage 1, 2 and 3. Stage 1 samples were processed like regular Vale Brownfield Exploration samples: 2 samples of high-grade ore in-house reference material and one quartzite blank per every 100 samples. The samples were analyzed at ALS Labs. Due to the relatively small number of quality control samples and a higher grade reference material the quality of Stage 1 analysis results were assessed by comparing with Stage 2 analysis results (Figure A-4).

Stage 2 quality control measures included insertion 6 of each of quartzite blanks, duplicate samples, 2 types of standard reference material and one type of in-house reference material which were chosen to be representative in composition of the range of rock types from the South Manasan Intrusion. The samples were analyzed at ALS Labs. The following materials were used to assess the quality of Stage 2 analysis.

Lawson quartzite blanks were used to assess the carryover contamination between samples. Material was obtained from Vale Brownfield exploration, Sudbury, ON. The quartzite is from the Lorrain formation, Cobalt group, Huronian Supergroup. The sample site is adjacent

to Lawson Quarry located 70 km southwest of Sudbury and 16 km south southeast of Espanola, ON.

OKUM reference material was used to assess the quality of analysis of Cr, MgO, FeO and LOI. Material was obtained from Ontario Geoscience Laboratories, Sudbury, ON. The material is an ultramafic komatiite collected at Serpentine Mountain in McArthur Township, 25 km south of Timmins, Ontario, Canada. The sample consists of black massive rocks composed of randomly oriented spinifex blades 5-10 cm long.

The results of analysis raised questions about the reliability of quoted provisional values, specifically for FeO and MgO (which were otherwise within limits for WPR-1 and TH-1) and were therefore excluded from the quality control process.

WPR-1 reference material was used to assess the quality of analysis of Ni, Cu, S, Au, Pt, Pd, Cr, MgO, Feo and LOI. Material was obtained from CANMET Mining and Mineral Science Laboratories, Ottawa, ON. The material is an altered peridotite from the Wellgreen Complex, Yukon territory, Canada which contains essentially antigorite with small amounts of chlorite and accessory magnetite and chromite. The peridotite contains pyrrhotite, pentlandite and chalcopyrite all enclosed, penetrated or intergrown with magnetite. Violarite occurs as inclusions in the pyrrhotite. PGE tellurides have also been noted.

TH-1 reference material was used to assess the quality of analysis of Ni, Cu, S, Au, Pt, Pd, Cr, MgO and FeO. Material was generated by blending coarse rejects of Vale Manitoba ore sample (approximately 75% Thompson orebody and 25% Birchtree orebody) and is routinely used for quality control of exploration samples. The recommended values of the TH-1 were determined by 40 analyses by ALS labs assayed on different days and by different operators and the control limits (at 3 standard deviations) were derived from the same analytical data set. The

standard deviation control limits are supplemented by the precision-related control limits which are based on the decomposition technique and analytical finish, taking into account the fact that the imprecision increases as the concentration approaches the detection limit of the method. The control limits were set as follows:

Upper Control Limit = Recommended Value + (Method Precision x Recommended Value + Detection Limit)

Lower Control Limit = Recommended Value - (Method Precision x Recommended Value + Detection Limit)

Stage 3 quality control measures comprised analysis of a well-characterized in-house sample and a standard reference material and comparison of the results with expected values. Samples were analyzed at Geolabs for rare-earth and trace elements and at Actlabs for PGEs. Due to the relatively small number of quality control samples the quality of Stage 3 analysis results were assessed by comparing with Stage 2 analysis results. The following materials were used to assess the quality of Stage 3 analysis.

VBLO reference material was used to assess the quality of rare-earth and trace element analysis. The material is an in-house Vale standard made from a representative sample of Voisey's Bay troctolite with trace sulfide mineralization.

AMIS0022 reference material was also used to assess the quality of PGE analysis. The material was prepared by African Mineral Standards from a Platreef PGE-Cu-Ni ore. The material was obtained by the laboratory from Anglo Platinum Limited from the 150/80 bench at the northern end of the Sandsloot open pit, PPRust Mine on the northern limb of the Bushveld

Complex. The material was crushed, dry milled and air-classified to <54 μm. It was then blended in a bi-conical mixer, systematically divided and sealed into 1 kg packs. 12 laboratories were each given 8 randomly selected packages of samples and results from 11 of those laboratories were used for the determination of accepted values.

Quality control results

Ni was most reliably determined by ICP81 (Fig 3A-A and B). Below 0.1% Ni (established with OKUM standard reference material) no particular method was effective. However, the vast majority of lithogeochemistry samples had concentrations above 0.1% and Ni tenor was not calculated below 0.25% Ni. No carryover contamination has been detected in quartzite samples.

Cu was equally reliable by ICP81 and XRF05 with no carryover contamination detected in quartzite samples (Fig 3A-C and D).

S was most reliable by ICP81 (Fig 3A-E and F) with minor carryover contamination detected in quartzite blanks (<0.09%) (Fig 3A-G). Ni tenor calculations were not carried out below 0.25% S and calculated Ni tenor were not used on an individual basis, but as trends.

MgO was most reliable by ICP81 with all analysis within bounds of analytical uncertainty (Fig 3A-H and I). However, OKUM standard reference material assay results returned 1.5-2% below expected values. Contamination carryover in quartzite blanks was as high as 0.5 wt% (Fig 3A-J).

FeO was most reliable by ICP81 with all analysis within bounds of analytical uncertainty (Fig 3A-K and L). However, OKUM standard reference material assay results returned 2 wt. % above expected values. Contamination carryover in quartzite blanks was as high as 0.67 wt% which may explain some of the elevated values (Fig 3A-M).

Cr analysis results were significantly different from the standard reference materials (Fig 3A-N). The most consistent results were obtained from XRF05; however, the results were elevated by 500 to 700 ppm above expected values. MS81 also provided results above the expected range, but with significant scatter in values (up to 800 ppm). On the other hand ICP61 results were either at the low range of expected values (WPR-1 standard reference material) or significantly below (700 ppm lower) than expected values (OKUM standard reference material). Contamination carryover in quartzite blanks was 20-40 ppm (Fig 3A-O) which is too low to explain the 500-700 ppm offset observed with the use of XRF05 method on WPR-1 standard reference material. The presence of Cr-spinel has been observed in polished thin section on the SEM; however, it appears the absolute abundances of Cr cannot be established reliably with the lithogeochemical methods used in this study.

LOI was above expected ranges by 0.5-1.7 wt. % (Fig 3A-P). Contamination carryover in quartzite blanks was as high as 1.29 wt. % (Fig 3A-Q). It seems that a significant and readily apparent amount of altered ultramafic rock is required to introduce that much LOI into the sample. Therefore, it is more likely that weighing uncertainties or sample loss is responsible for up to 1.29 wt. % LOI in quartzite blanks.

Au concentrations were partially outside of very low range provided by the TH1 (Fig 3A-R) and WPR-1 standard reference material (Fig 3A-S). Analytical results were mostly below the determination limit of the PGM-ICP23 method.

Pt concentrations were within bounds of analytical uncertainty at intermediate levels (0.285 ppm) (Fig 3A-U) and mostly within bounds at very low levels (0.034 ppm) (Fig 3A-T).

Pd concentrations were within bounds of analytical uncertainty at intermediate levels (0.235 ppm) (Fig 3A-W) and within bounds at low levels (0.083 ppm) (Fig 3A-V).

Geochemical assay results

Data Repository 2 is digital file in Excel 2010 containing all whole-rock analytical results obtained from the drill core samples of the South Manasan intrusion.

Mineralogy methods

97 polished this sections 30 microns thick were prepared by Vancouver Petrographics from small section of split drillcore. Reconnaissance petrography of 97 polished thin sections was carried out using a Mieji MT microscope at the Vale petrography lab in Thompson MB and yielded modal mineralogy, grain size and micro-textures. High quality photomicrographs of representative textures and minerals were obtained using a petrographic microscope equipped with a camera at the petrography lab at Laurentian University, Ontario. 9 polished thin sections were coated with graphite and used for SEM-EDS analysis to document mineral chemistry, principally sulfide and textural relationships. The SEM-EDS system used in this study consisted of an Oxford Sight EDS (energy dispersive detector) mounted on a JEOL 6400 scanning

electron microscope at the Central Analytical Facility of Laurentian University, Canada. Data were acquired at an accelerating voltage of 15 kV, a 1.005 nA beam current and with acquisition count times of 5-10 s, and a working distance of 15 mm. Jadeite, diopside, orthoclase, corundum, quartz, chalcopyrite, and pyrophanite were used as standards for calibrating the instrument. 11 polished this sections were used for olivine and serpentine analysis by wavelength dispersive analysis using a CAMECA SX50 electron microprobe at Indiana University. An accelerating voltage of 15 kV was used. Beam current and peak counting time for major elements were 20 nA and 20 s, respectively. Nickel was analyzed at a beam current of 100 nA, a peak counting time of 100 s and a beam diameter was 10 μm. The detection limit for Ni under these conditions was about 60 ppm in olivine and about 100 ppm in serpentine. The accuracy of analysis was monitored using a reference material of similar compositions.

Mineralogy results

Sulfide mineral and silicate analysis by SEM-EDS is tabulated in Data Repository 3. Olivine and serpentine mineral analysis by Microprobe are tabulated in Data Repository 4. Representative mineral analysis is summarized in Table 3.

Assay group & Lab	Method code		Method description	Elements analyzed	Number of samples			
					Borehole #			Total
					115175	115191	115194	
Stage 1: ALS	Ore grade	ME-ICP81	Sodium peroxide fusion ICP-AES	Ni, Cu, Co, Fe, Pb, Zn, As, S, Mg	140	59	76	275
		PGM-ICP23	Fire assay ICP-AES	Pt, Pd, Au				
Stage 2: ALS	Ore grade	ME-ICP81	Sodium peroxide fusion ICP-AES	Ni, Cu, Co, Fe, Pb, Zn, As, S, Mg	30	23	20	73
		PGM-ICP23	Fire assay ICP-AES	Pt, Pd, Au				
	Trace	ME-XRF05	Pressed pellet XRF	Trace element oxides				
		ME-ICP06	Li metaborate fusion ICP-AES	Major element oxides				
		ME-MS81	Li metaborate fusion ICP-MS	Rare earth & trace elements				
		ME-ICP61	Four acid near total ICP-AES	Rare earth & trace elements				
		LOI OA-GRA05	LOI at 1000°C	Loss on ignition				
		S-IR08	Total Sulphur using a Leco	S				
		C C-IR07	Combustion furnace	C				
Stage 3: Actlabs, Geolabs	Ultra-trace	IMC-100		Rare earth & trace elements	12	0	0	12
		NI-FINA		Os, Ir, Ru, Rh, Pt, Pd, Au, Re				
Vale Thompson exploration office	Specific gravity and magnetic susceptibility (number of core samples)				140	59	76	275
	Thin section microscopy (number of thin sections)				46	23	28	97
Laurentian University	Reconnaissance SEM-EDS mineral chemistry (number of thin sections)				9	2	2	13
Indiana University	Microprobe mineral chemisty of olivine and serpentine (number of thin sections)				11	4	4	19

Table A-1 Summary of analytical methods and sample quantities used to collect data from the South Manasan intrusion. Lithogeochemical analysis was completed in 3 stages: (1) ore-grade half-core samples of all ultramafic and sulfide occurrences in drill core, (2) ore-grade, LOI, C and trace elements from select quarter-core samples representative of the rock units, and (3) high-quality rare-earth, trace and PGE determinations from a small number of quarter-core samples. For a diagram of sample selection see Figure A-2. Method code is explained in the text.

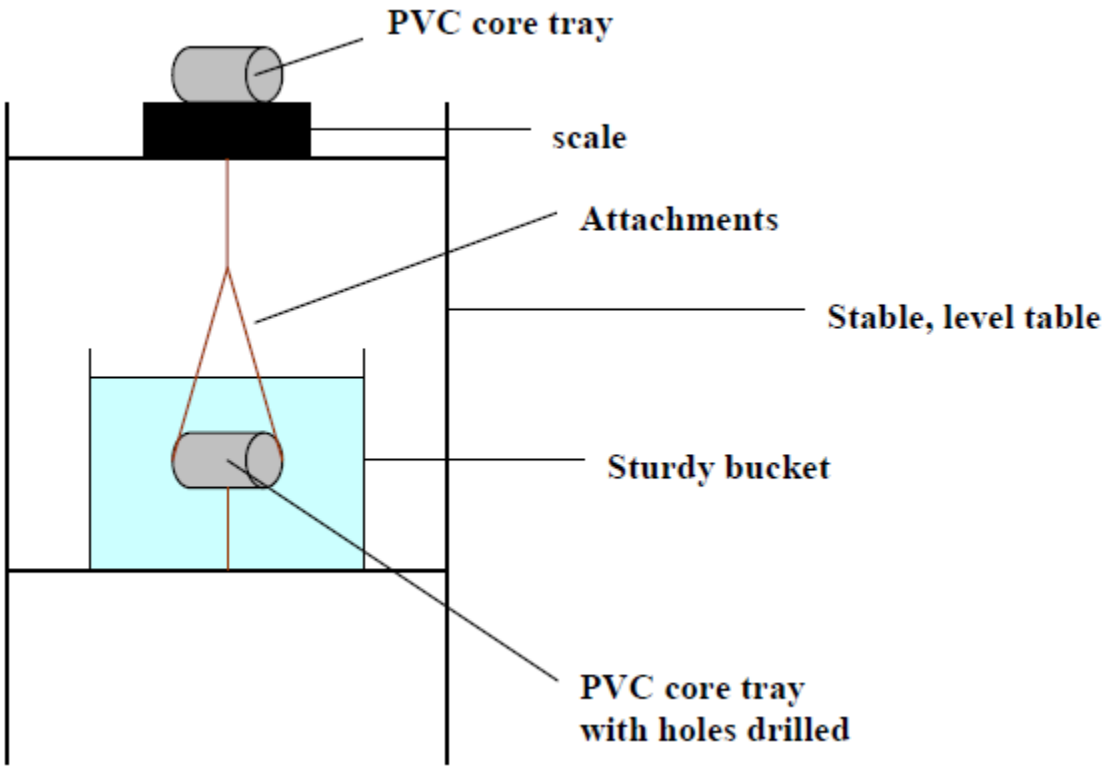

Figure A-1 Specific gravity equipment setup. A representative piece of drill core from each sample interval was measured on top of the scale to obtain "weight in air". Following that, the same piece was weighed in a water-submerged tray suspended from a weighing hook underneath the scale to obtain "weight in water". The density was calculated according to formula in text.

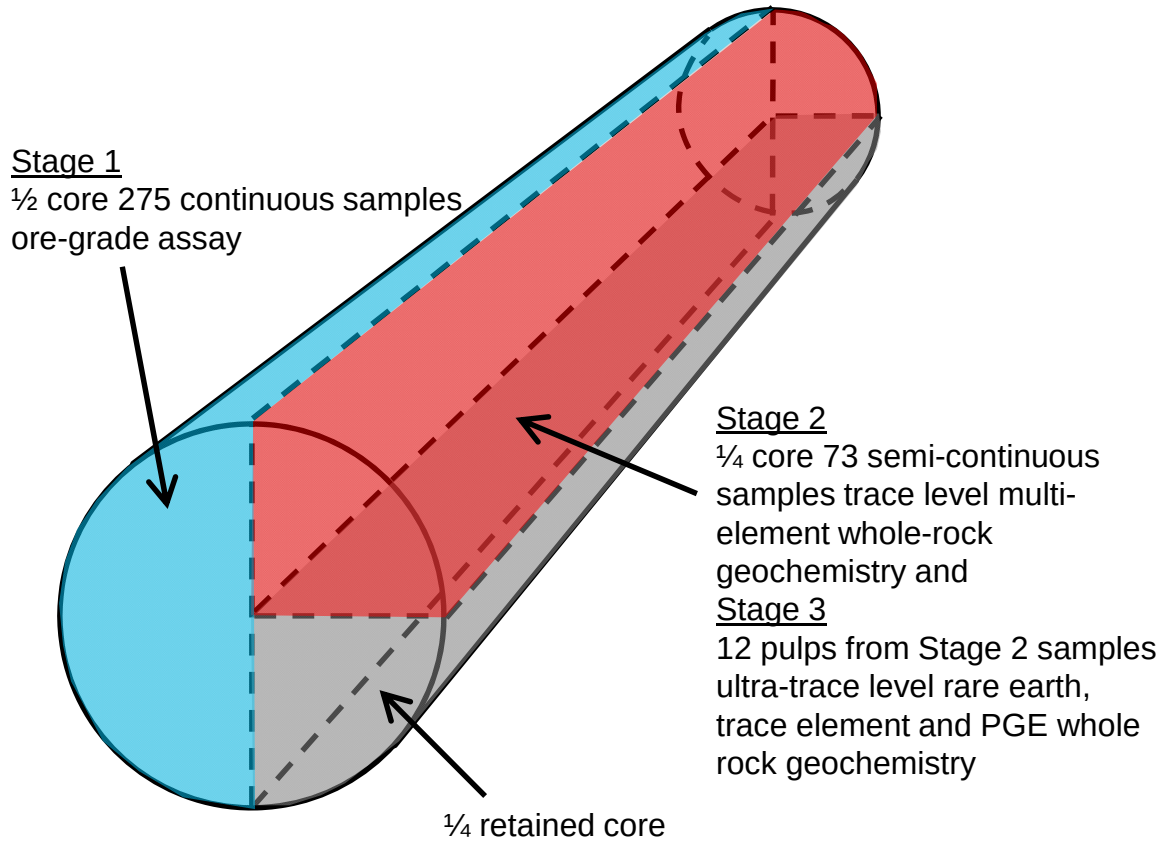

Figure A-2. Sketch of the drill core sampling. Lithogeochemical analysis was completed in 3 stages: (1) ore-grade half-core samples of all ultramafic and sulfide occurrences in drill core, (2) ore-grade, LOI, C and trace elements from select quarter-core samples representative of the rock units, and (3) high-quality rare-earth, trace and PGE determinations from a small number of quarter-core samples.

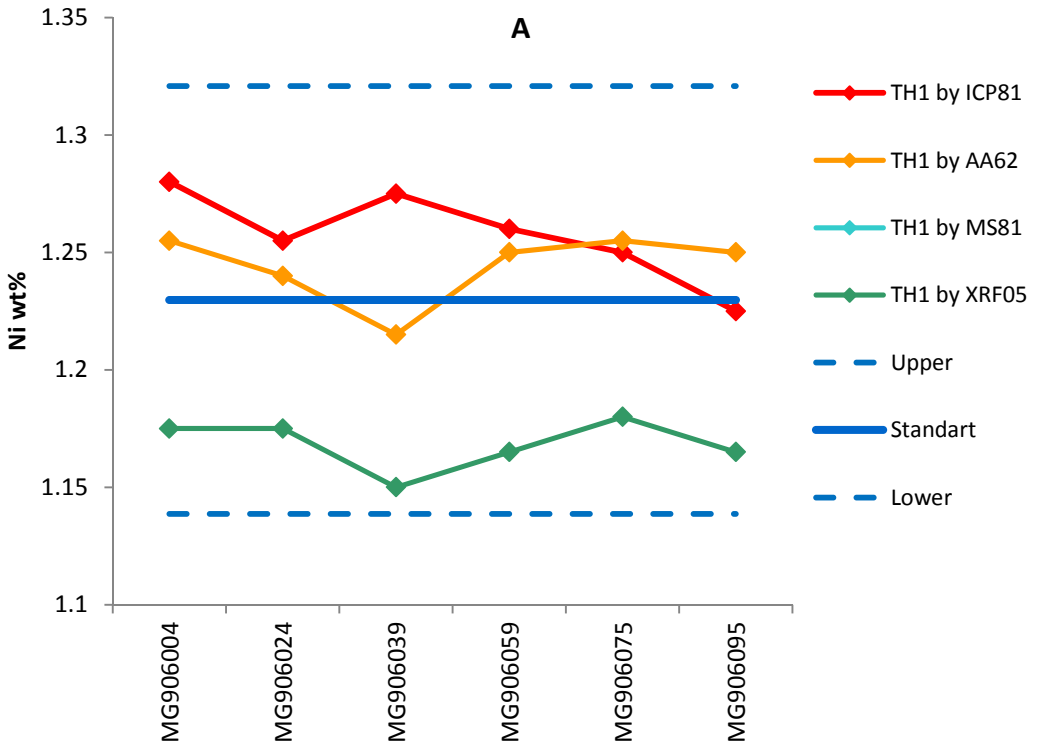
A
Ni wt%
1.35
1.3
1.25
1.2
1.15
1.1
MG906004
MG906024
MG906039
MG906059
MG906075
MG906095
TH1 by ICP81
TH1 by AA62
TH1 by MS81
TH1 by XRF05
Upper
Standart
Lower

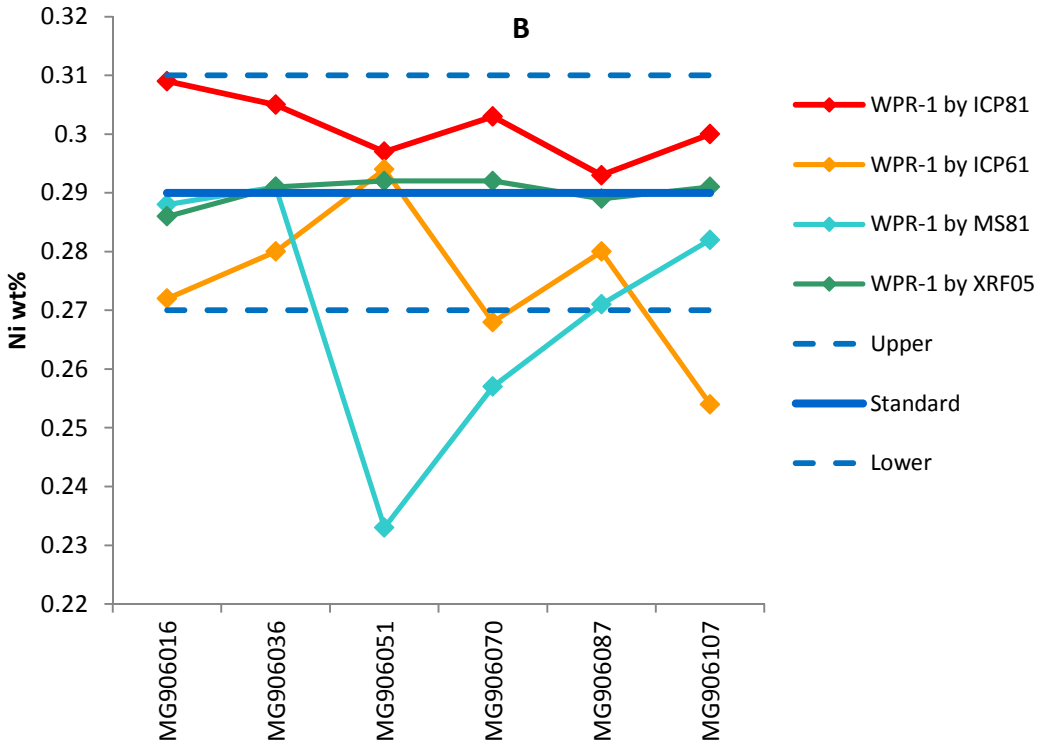
B
Ni wt%
0.32
0.31
0.3
0.29
0.28
0.27
0.26
0.25
0.24
0.23
0.22
MG906016
MG906036
MG906051
MG906070
MG906087
MG906107
WPR-1 by ICP81
WPR-1 by ICP61
WPR-1 by MS81
WPR-1 by XRF05
Upper
Standard
Lower

Figure A-3.

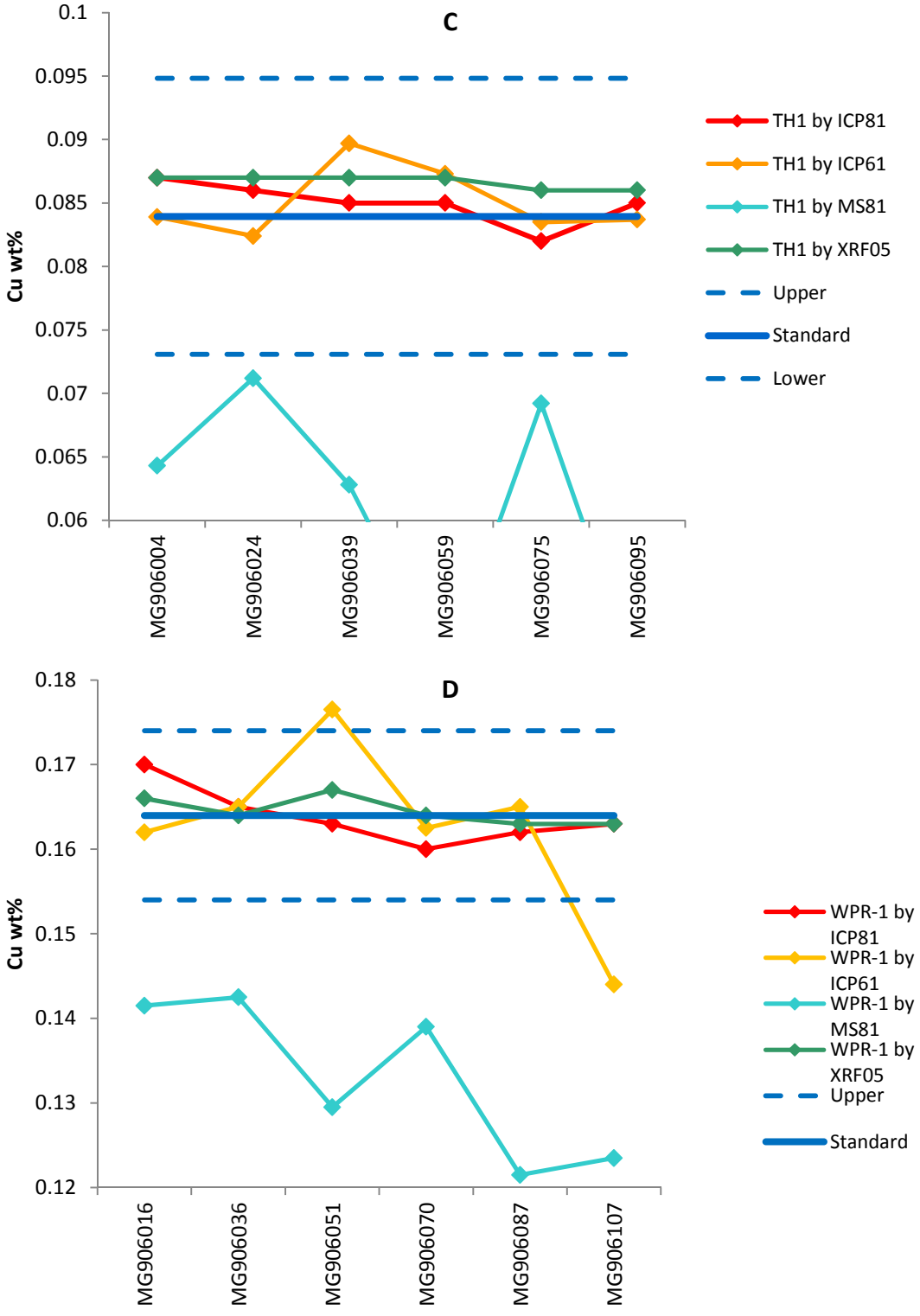
C
Cu wt%
0.1
0.095
0.09
0.085
0.08
0.075
0.07
0.065
0.06
MG906004
MG906024
MG906039
MG906059
MG906075
MG906095
TH1 by ICP81
TH1 by ICP61
TH1 by MS81
TH1 by XRF05
Upper
Standard
Lower
D
Cu wt%
0.18
0.17
0.16
0.15
0.14
0.13
0.12
MG906016
MG906036
MG906051
MG906070
MG906087
MG906107
WPR-1 by ICP81
WPR-1 by ICP61
WPR-1 by MS81
WPR-1 by XRF05
Upper
Standard

Figure A-3.

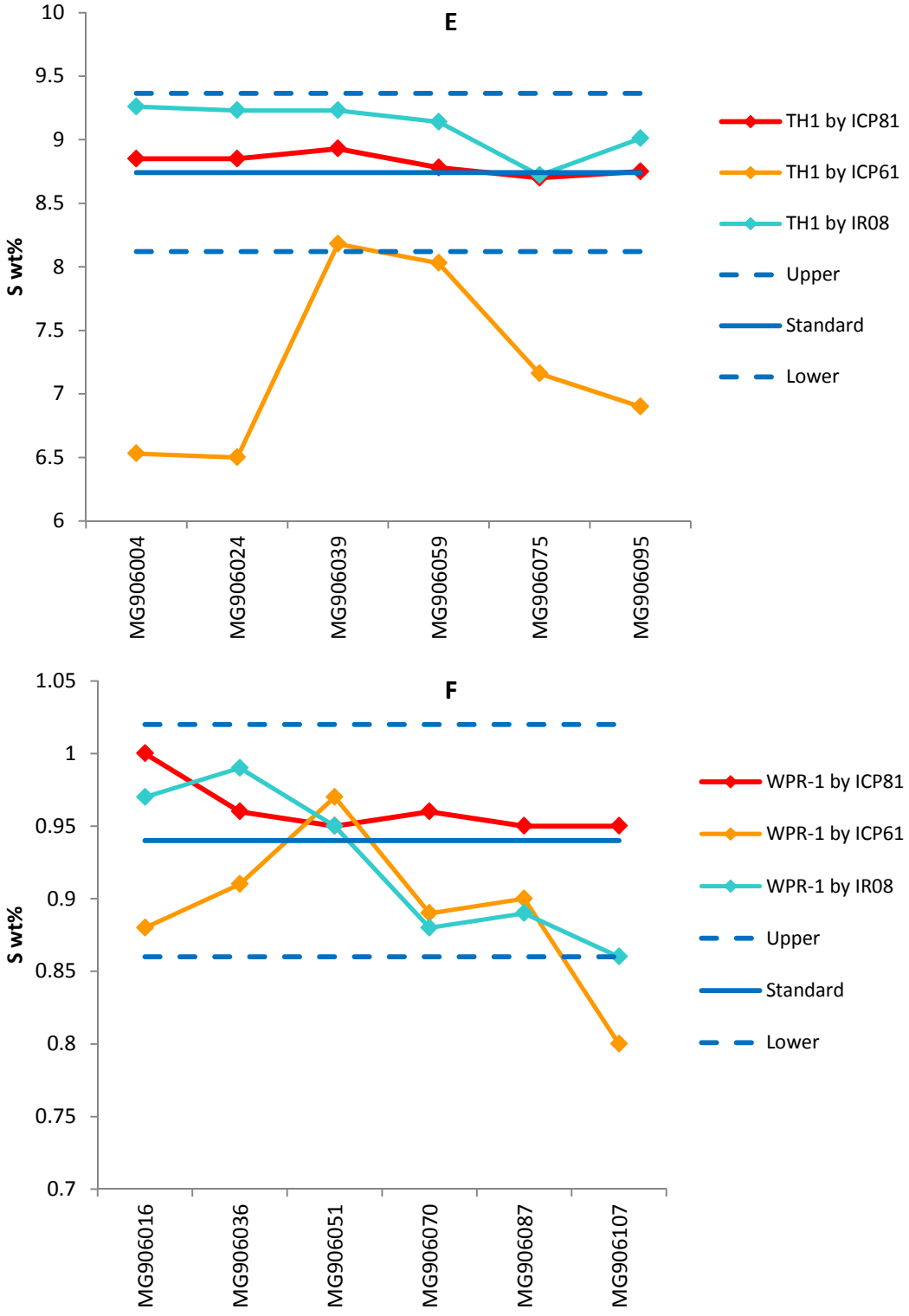

Figure A-3.

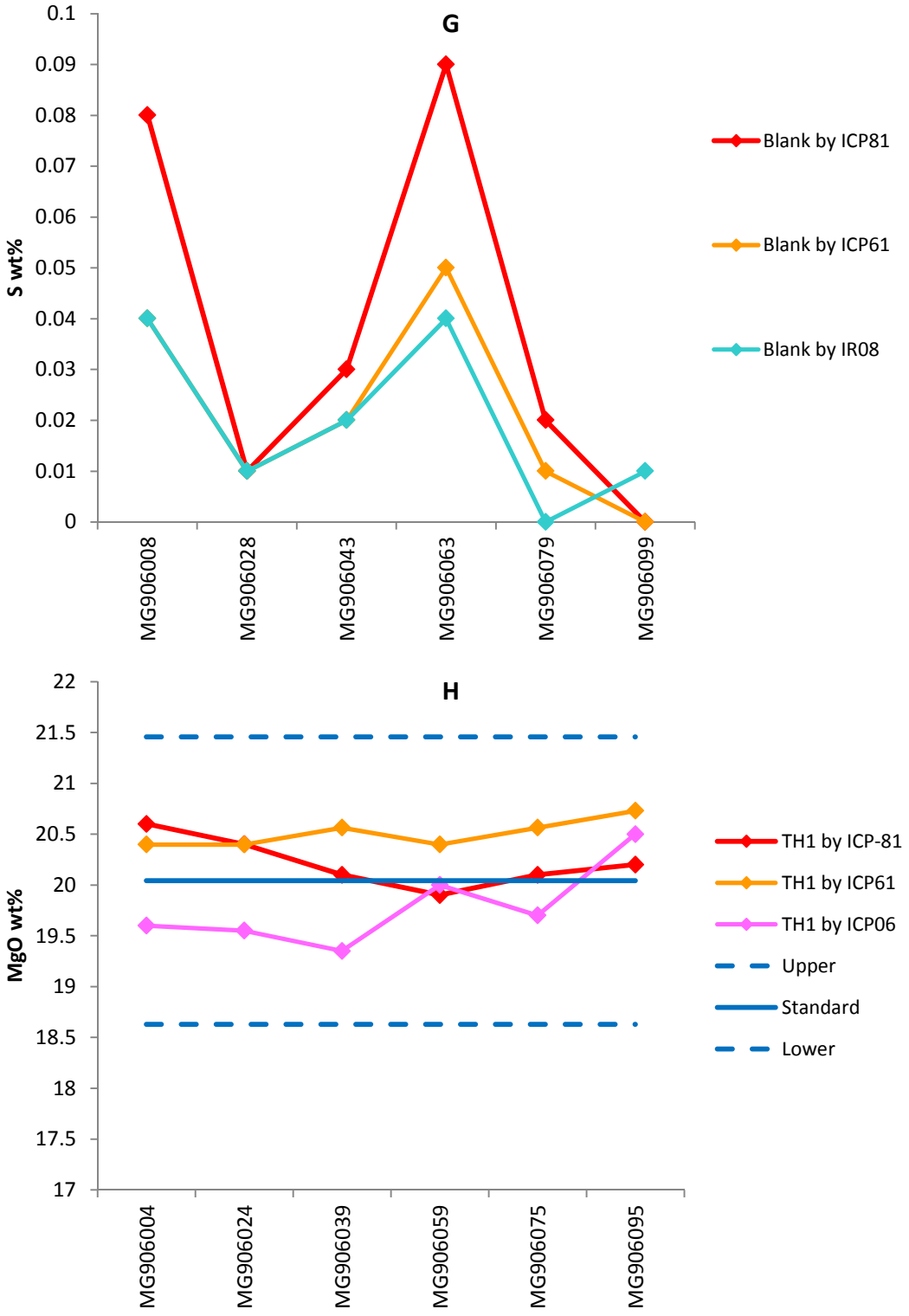
G
S wt%
0.1
0.09
0.08
0.07
0.06
0.05
0.04
0.03
0.02
0.01
0
MG906008
MG906028
MG906043
MG906063
MG906079
MG906099
Blank by ICP81
Blank by ICP61
Blank by IR08
H
MgO wt%
22
21.5
21
20.5
20
19.5
19
18.5
18
17.5
17
MG906004
MG906024
MG906039
MG906059
MG906075
MG906095
TH1 by ICP-81
TH1 by ICP61
TH1 by ICP06
Upper
Standard
Lower

Figure A-3.

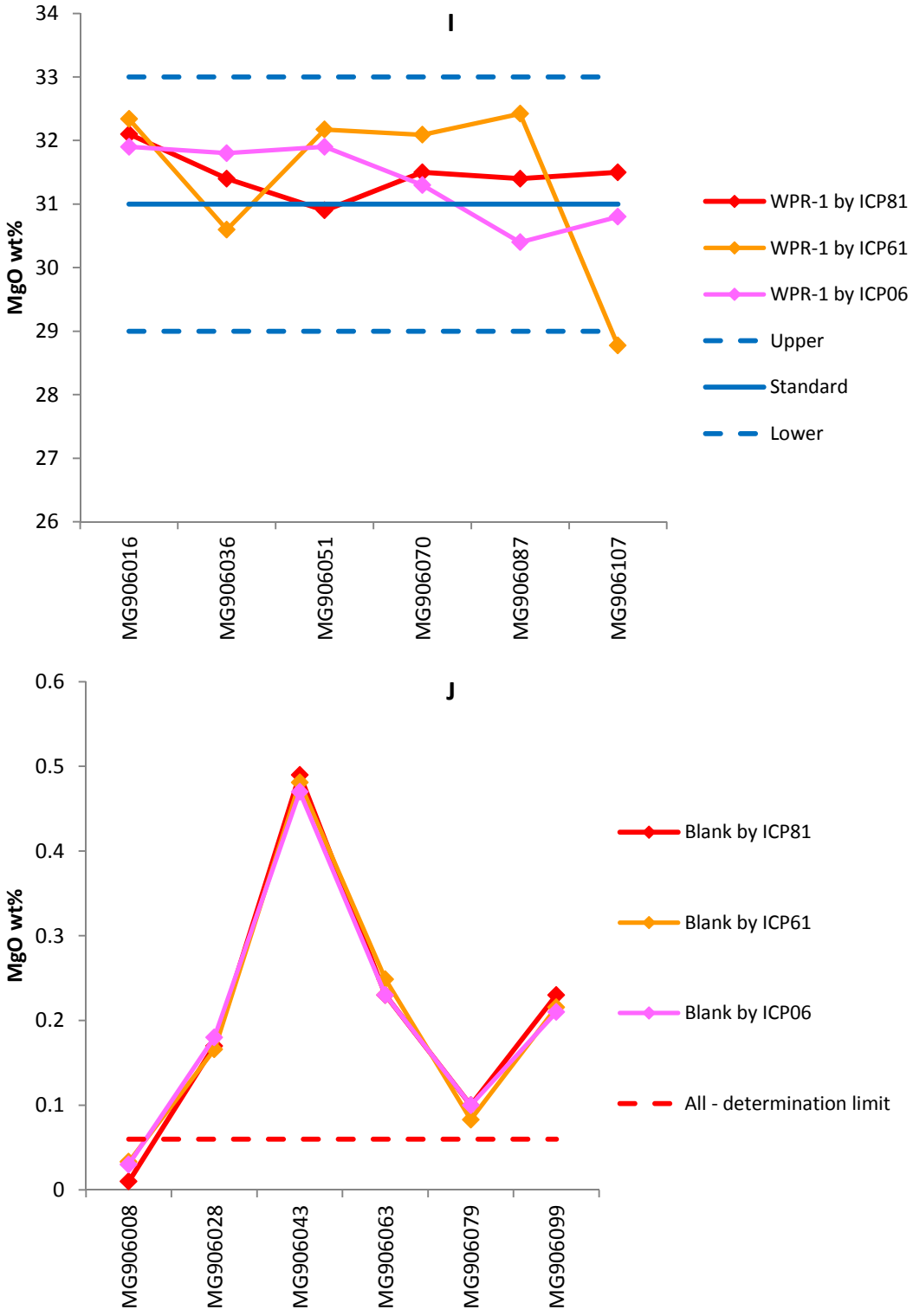
I
MgO wt%
34
33
32
31
30
29
28
27
26
MG906016
MG906036
MG906051
MG906070
MG906087
MG906107
WPR-1 by ICP81
WPR-1 by ICP61
WPR-1 by ICP06
Upper
Standard
Lower
J
MgO wt%
0.6
0.5
0.4
0.3
0.2
0.1
0
MG906008
MG906028
MG906043
MG906063
MG906079
MG906099
Blank by ICP81
Blank by ICP61
Blank by ICP06
All - determination limit

Figure A-3.

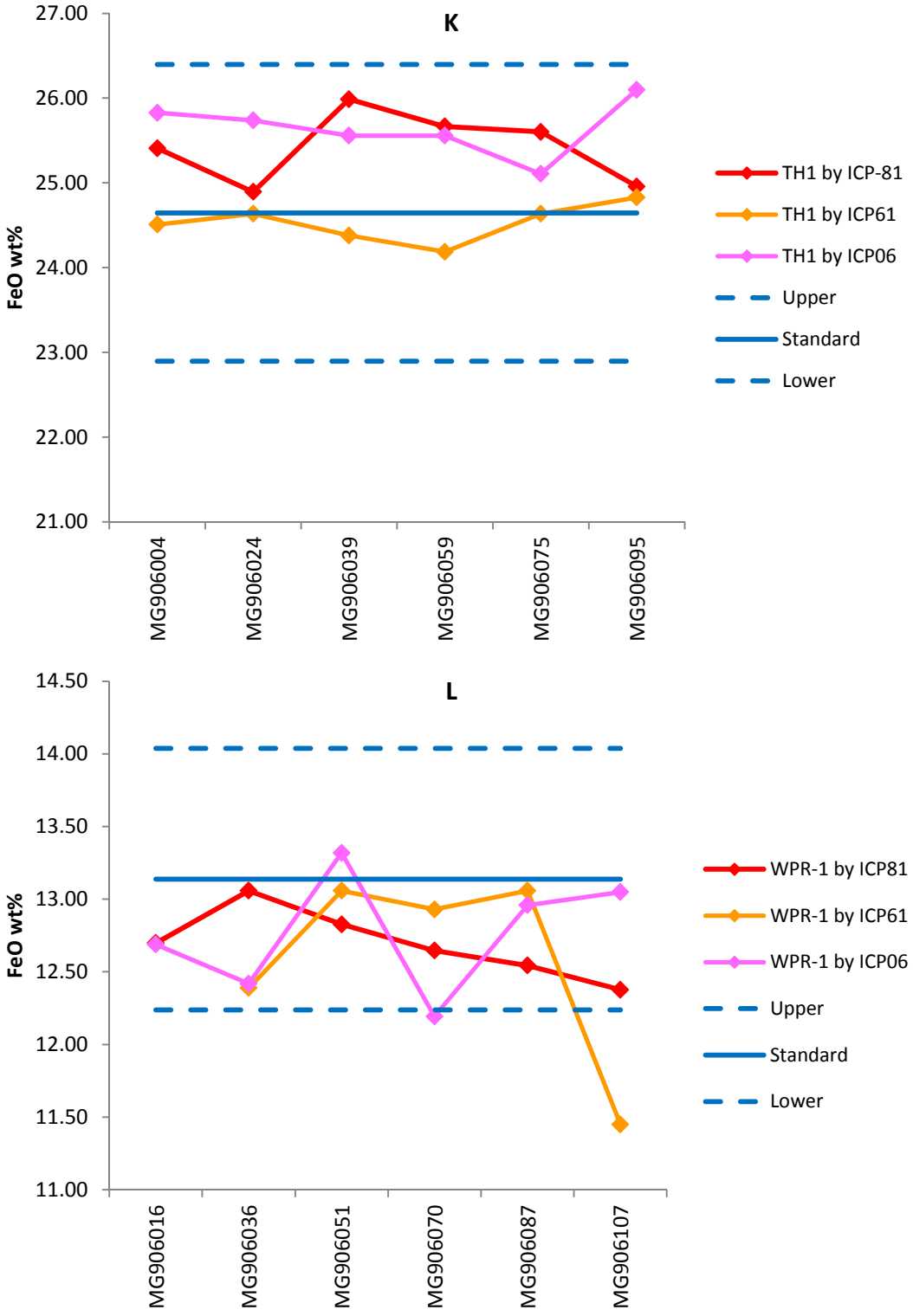
K
FeO wt%
27.00
26.00
25.00
24.00
23.00
22.00
21.00
MG906004
MG906024
MG906039
MG906059
MG906075
MG906095
TH1 by ICP-81
TH1 by ICP61
TH1 by ICP06
Upper
Standard
Lower
L
FeO wt%
14.50
14.00
13.50
13.00
12.50
12.00
11.50
11.00
MG906016
MG906036
MG906051
MG906070
MG906087
MG906107
WPR-1 by ICP81
WPR-1 by ICP61
WPR-1 by ICP06
Upper
Standard
Lower

Figure A-3.

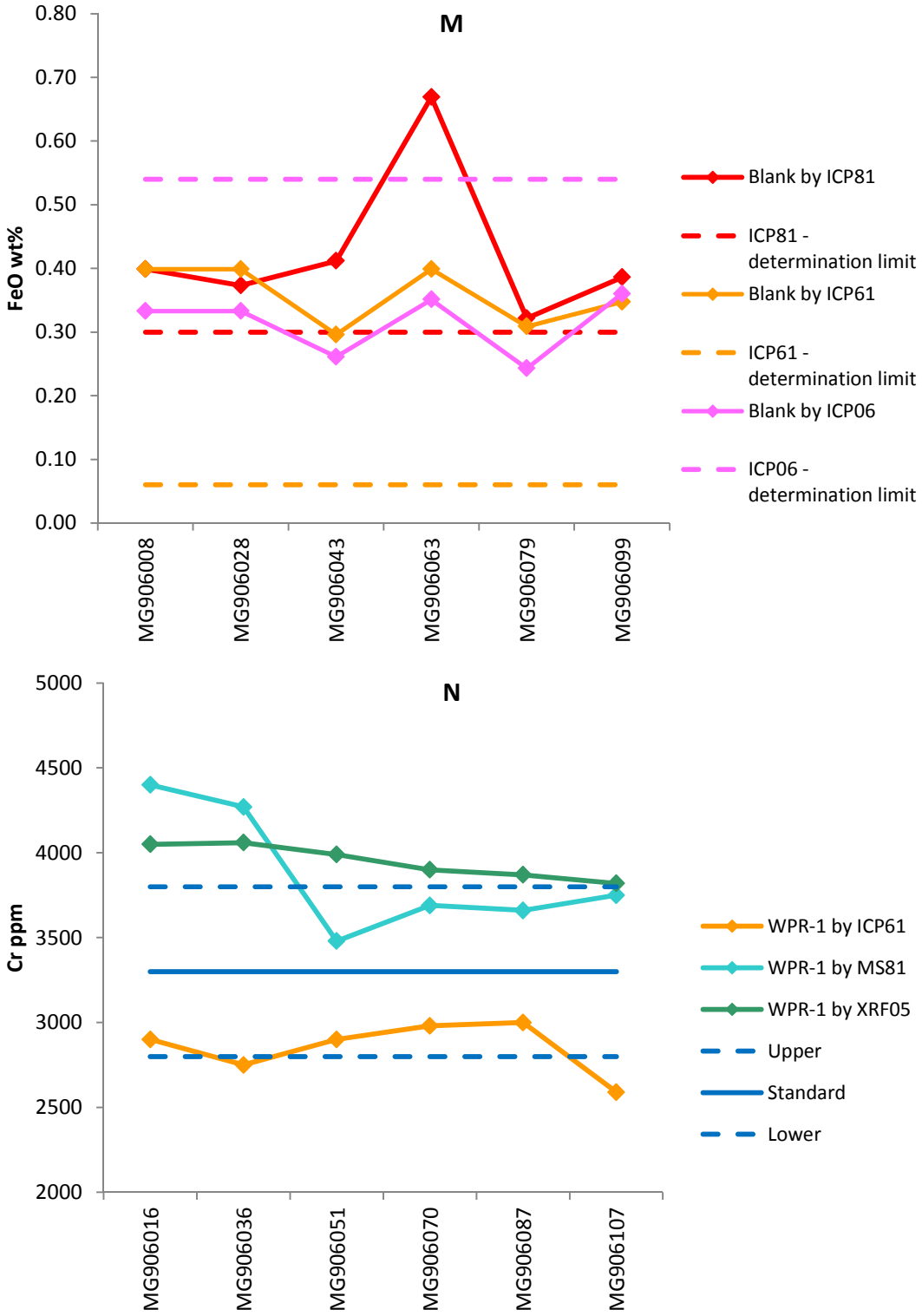
M
FeO wt%
0.80
0.70
0.60
0.50
0.40
0.30
0.20
0.10
0.00
MG906008
MG906028
MG906043
MG906063
MG906079
MG906099
Blank by ICP81
ICP81 - determination limit
Blank by ICP61
ICP61 - determination limit
Blank by ICP06
ICP06 - determination limit
N
Cr ppm
5000
4500
4000
3500
3000
2500
2000
MG906016
MG906036
MG906051
MG906070
MG906087
MG906107
WPR-1 by ICP61
WPR-1 by MS81
WPR-1 by XRF05
Upper
Standard
Lower

Figure A-3.

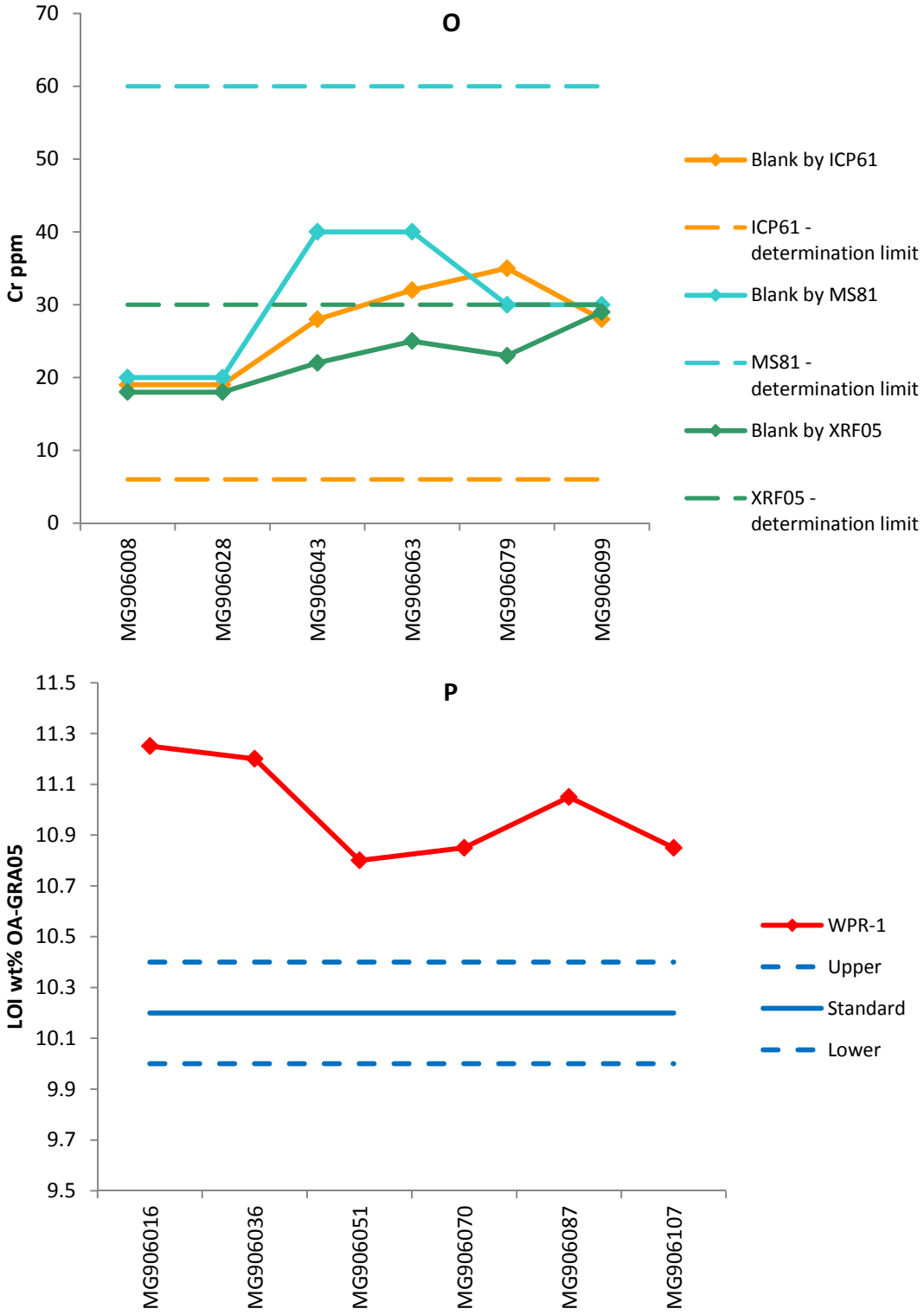
O
Cr ppm
70
60
50
40
30
20
10
0
MG906008
MG906028
MG906043
MG906063
MG906079
MG906099
Blank by ICP61
ICP61 - determination limit
Blank by MS81
MS81 - determination limit
Blank by XRF05
XRF05 - determination limit
P
LOI wt% OA-GRA05
11.5
11.3
11.1
10.9
10.7
10.5
10.3
10.1
9.9
9.7
9.5
MG906016
MG906036
MG906051
MG906070
MG906087
MG906107
WPR-1
Upper
Standard
Lower

Figure A-3.

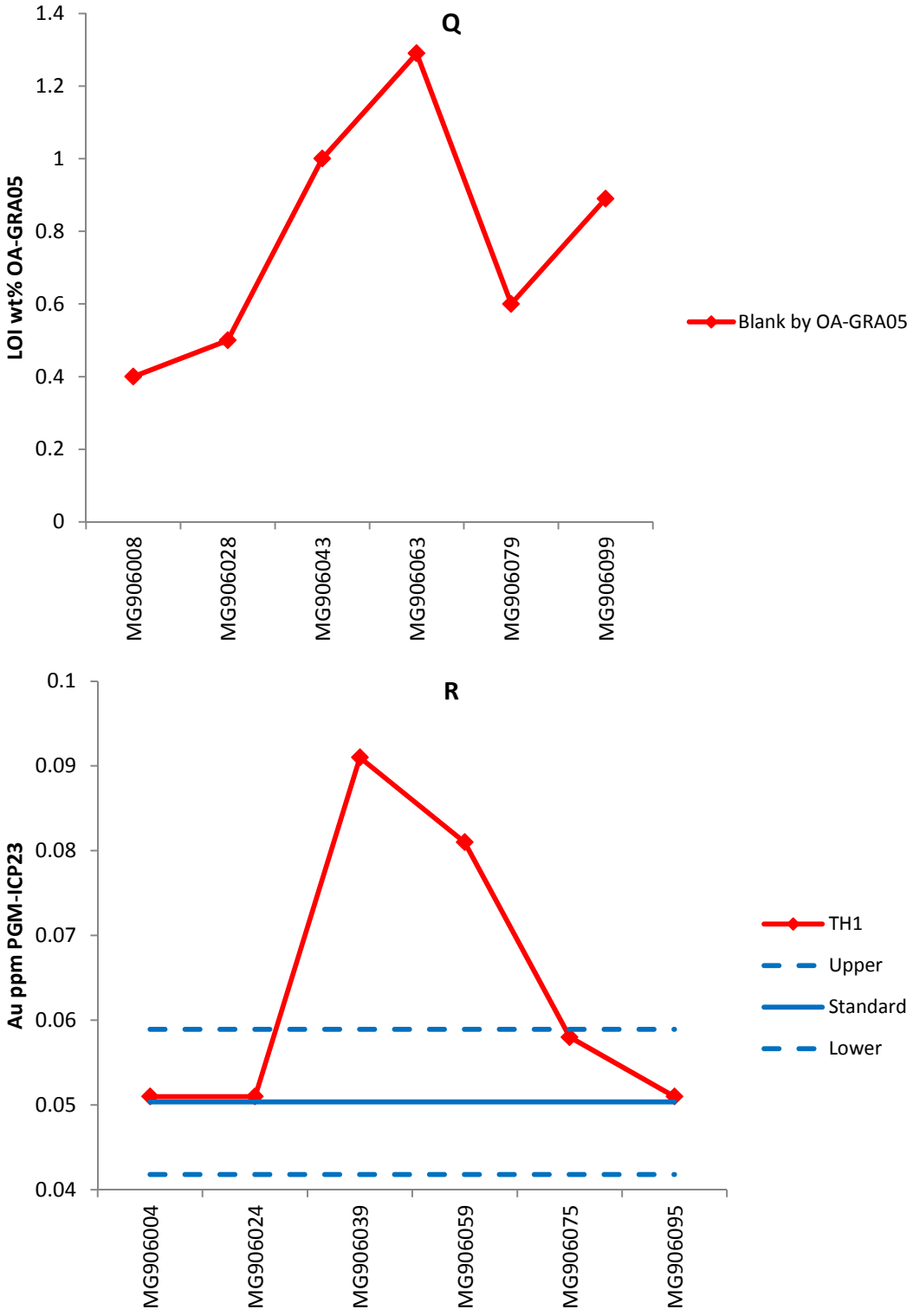
Q
LOI wt% OA-GRA05
1.4
1.2
1
0.8
0.6
0.4
0.2
0
MG906008
MG906028
MG906043
MG906063
MG906079
MG906099
Blank by OA-GRA05
R
Au ppm PGM-ICP23
0.1
0.09
0.08
0.07
0.06
0.05
0.04
MG906004
MG906024
MG906039
MG906059
MG906075
MG906095
TH1
Upper
Standard
Lower

Figure A-3.

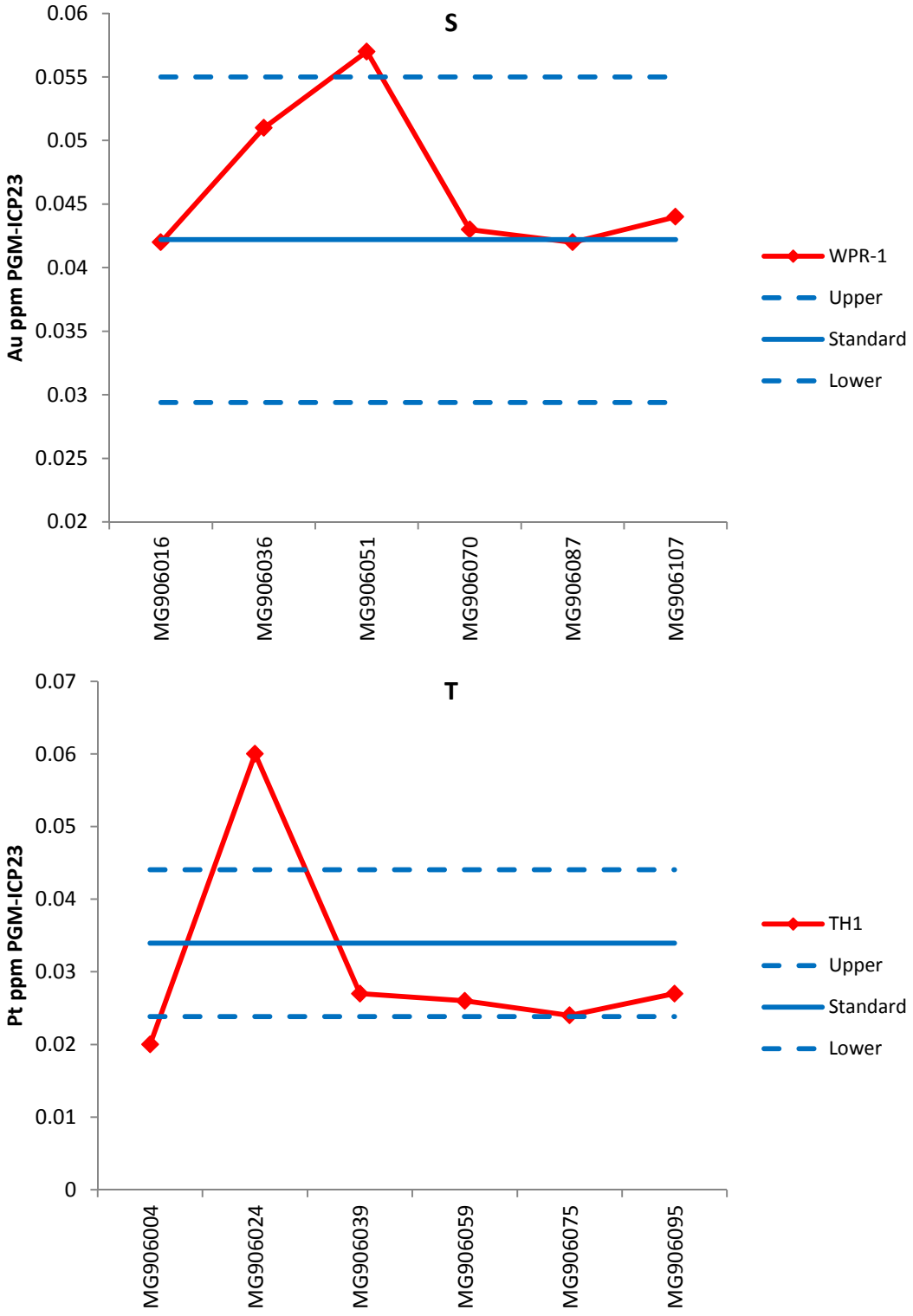
S
Au ppm PGM-ICP23
0.06
0.055
0.05
0.045
0.04
0.035
0.03
0.025
0.02
MG906016
MG906036
MG906051
MG906070
MG906087
MG906107
WPR-1
Upper
Standard
Lower
T
Pt ppm PGM-ICP23
0.07
0.06
0.05
0.04
0.03
0.02
0.01
0
MG906004
MG906024
MG906039
MG906059
MG906075
MG906095
TH1
Upper
Standard
Lower

Figure A-3.

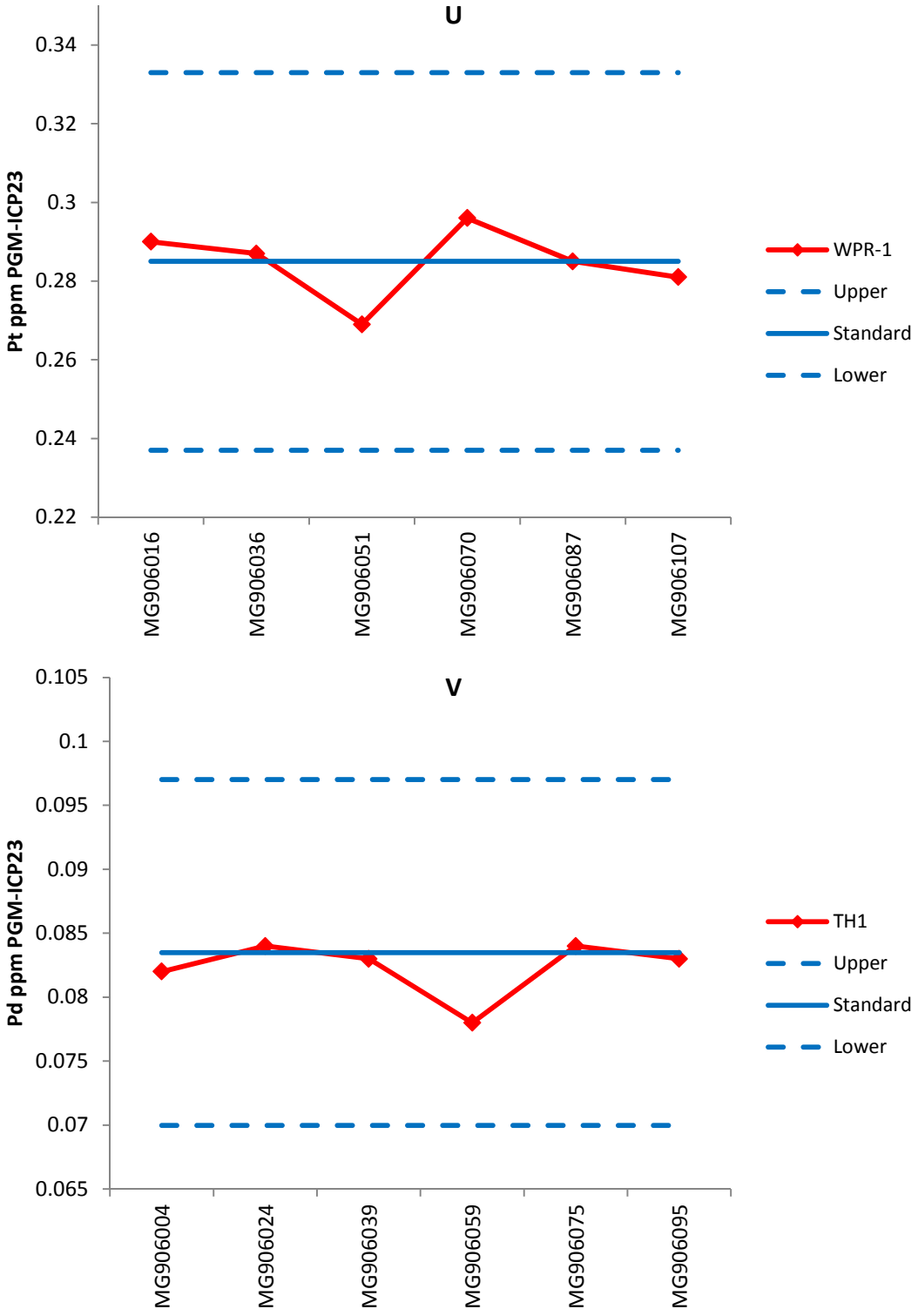
U
Pt ppm PGM-ICP23
0.34
0.32
0.3
0.28
0.26
0.24
0.22
MG906016
MG906036
MG906051
MG906070
MG906087
MG906107
WPR-1
Upper
Standard
Lower
V
Pd ppm PGM-ICP23
0.105
0.1
0.095
0.09
0.085
0.08
0.075
0.07
0.065
MG906004
MG906024
MG906039
MG906059
MG906075
MG906095
TH1
Upper
Standard
Lower

Figure A-3.

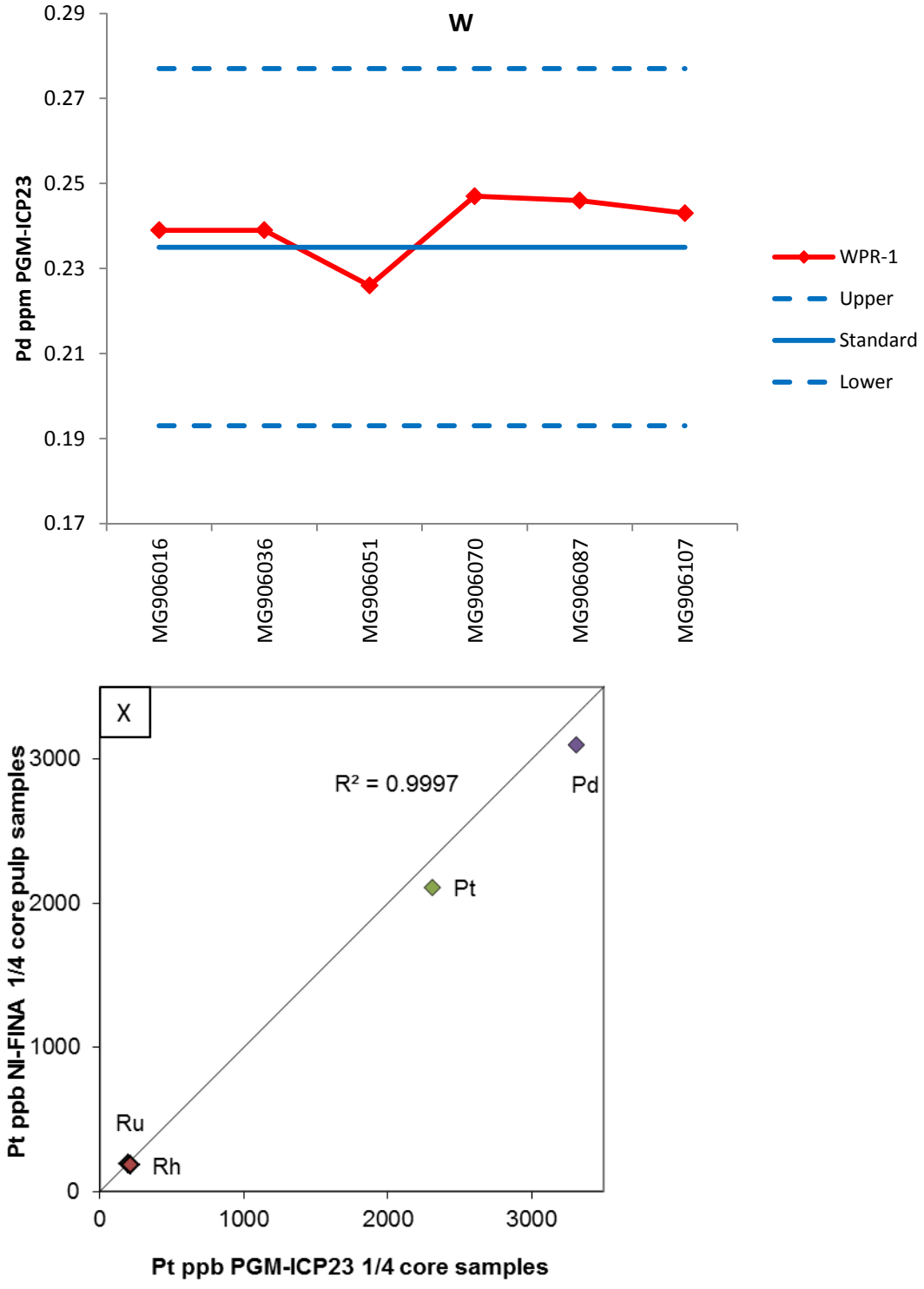
W
0.29
0.27
0.25
0.23
0.21
0.19
0.17
Pd ppm PGM-ICP23
MG906016
MG906036
MG906051
MG906070
MG906087
MG906107
WPR-1
Upper
Standard
Lower
X
R² = 0.9997
Pd
Pt
Ru
Rh
3000
2000
1000
0
Pt ppb NI-FINA 1/4 core pulp samples
Pt ppb PGM-ICP23 1/4 core samples

Figure A-3.

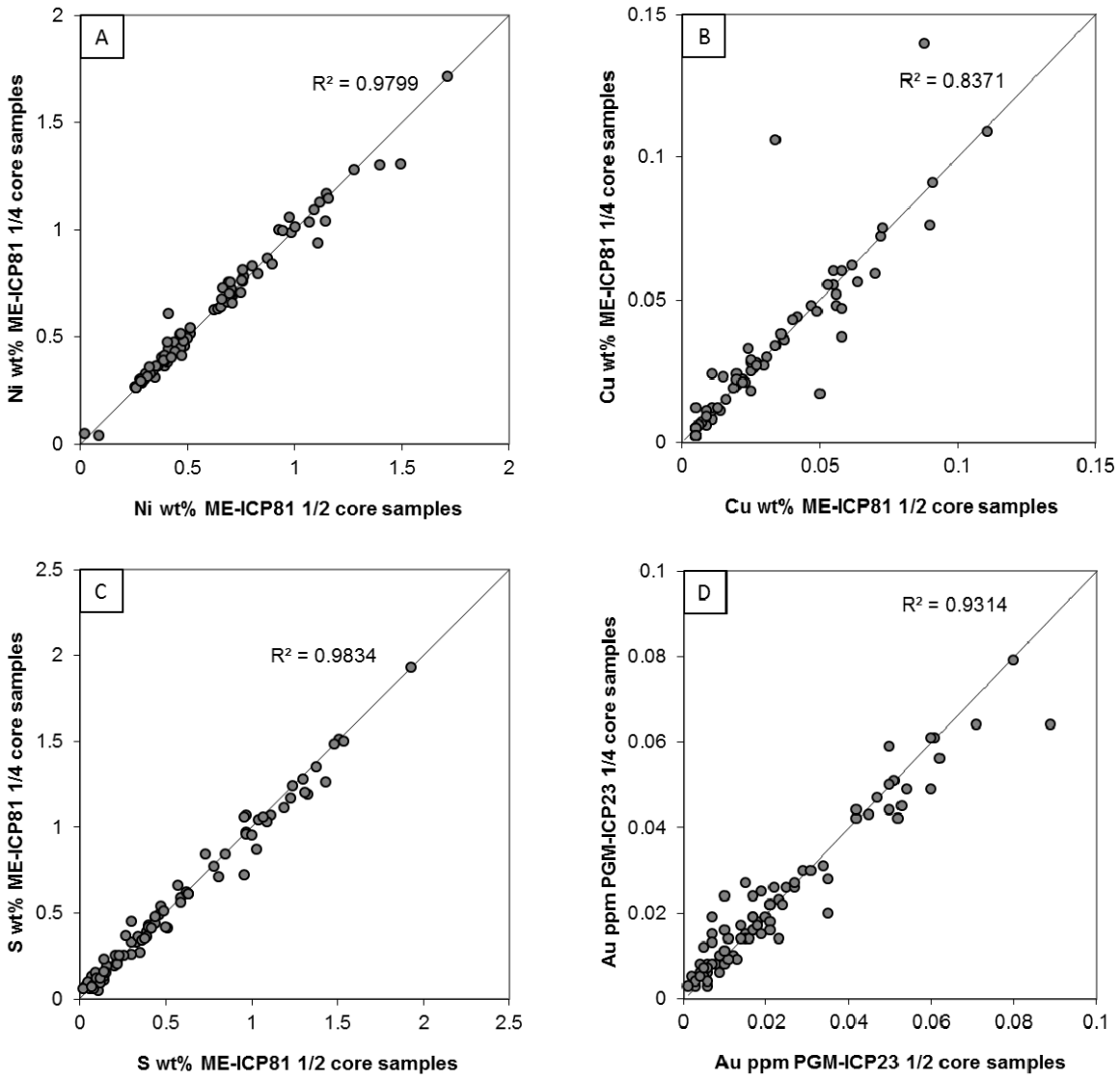

Figure A-4. Precision measured by sample duplicates. A) Ni wt%. B) Cu wt%. C) S wt%. D) Au ppm.

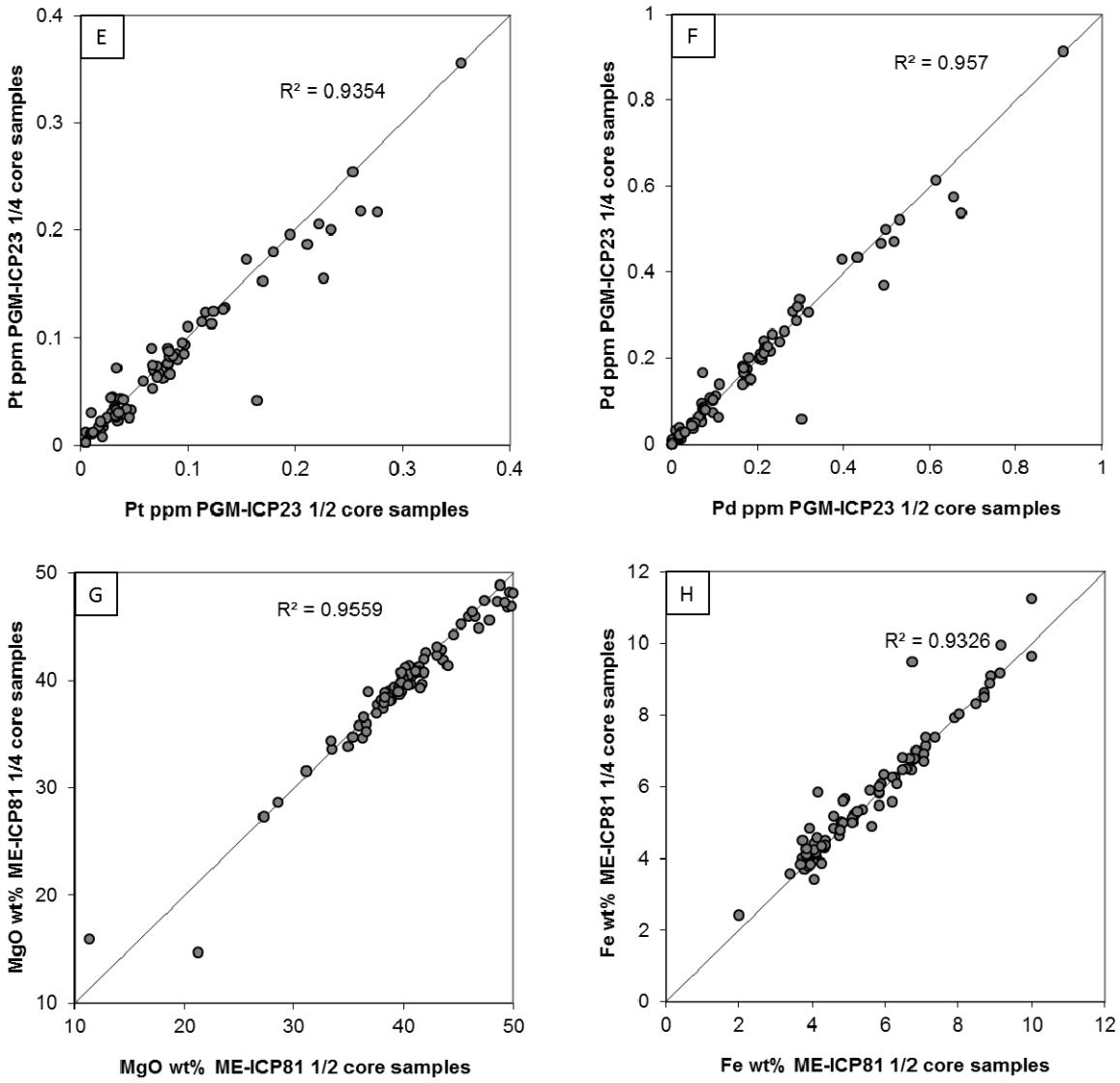

Figure A-4. Precision measured by sample duplicates. E) Pt ppm. F) Pd ppm. G) MgO wt%. H) Fe wt%.

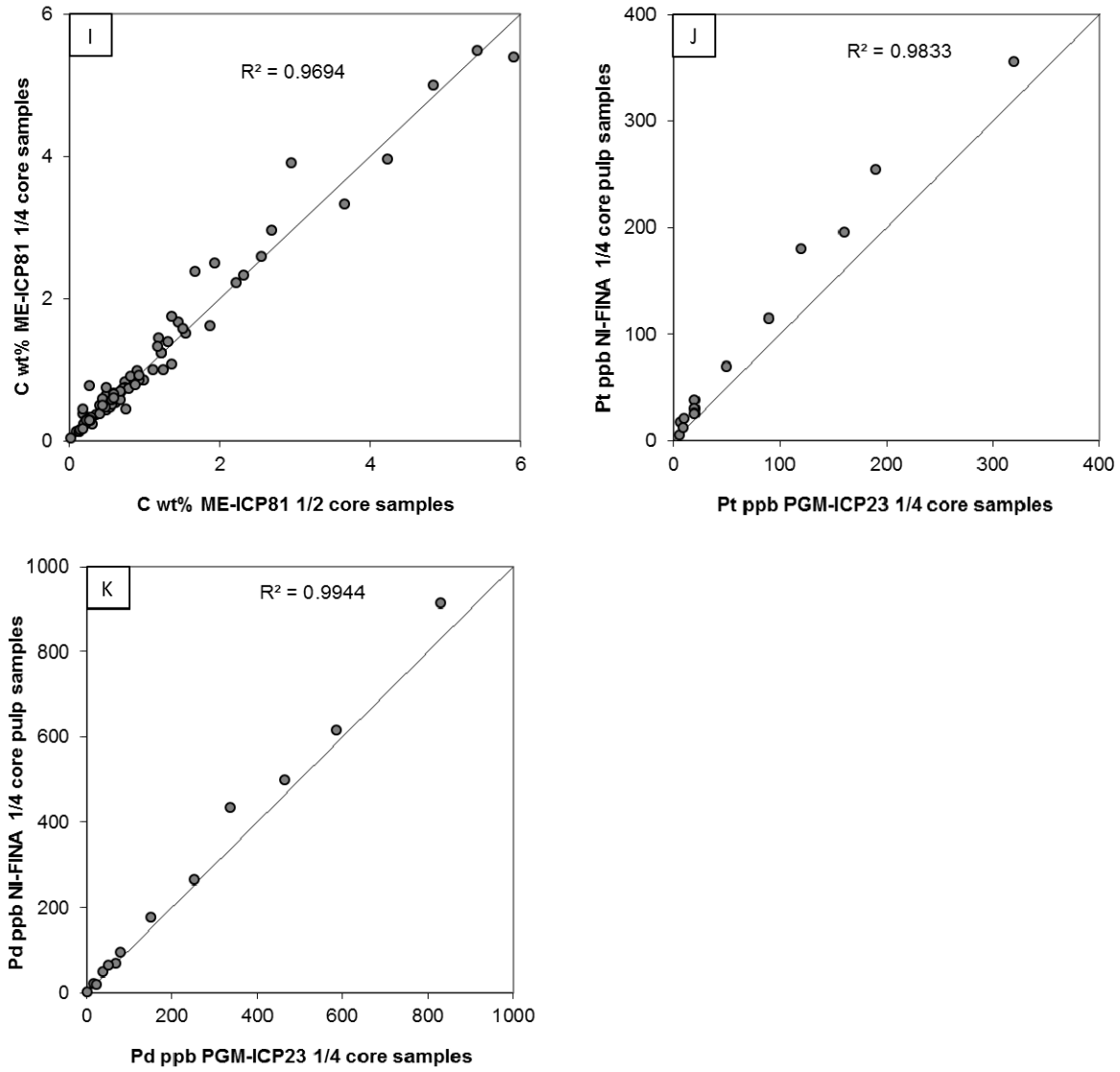

Figure A-4. Precision measured by sample duplicates. I) C wt%. J) Pt ppb. K) Pd ppb.